TECHNISCHE UNIVERSITÄT WIEN
Vienna University of Technology

Diploma Thesis

Development of a Multi-Physical CFD Model of a Lithium-Ion Cell and Simulation of Cooling Concepts for Vehicular Applications

presented in partial fulfillment of the requirements for the degree
Diplom-Ingenieur

supervised by
Ao. Univ.-Prof. Dipl.-Ing. Dr. techn. Andreas Werner
Institute for Energy Systems and Thermodynamics

conducted at the
Austrian Institute of Technology
under the guidance of
Dr. Fiorentino Valerio Conte
and
Dr. Christian Jungreuthmayer

submitted to the
Faculty of Mechanical and Industrial Engineering
Vienna University of Technology

by
Paul Georg Oberhumer
Oberbergham 2
4673 Gaspoltshofen

Vienna, April 2012

Affidavit

I, Paul Georg Oberhumer, hereby declare that I am the sole author of the present diploma thesis *Development of a Multi-Physical CFD Model of a Lithium-Ion Cell and Simulation of Cooling Concepts for Vehicular Applications* and that I have not used any source or tool other than those referenced. This thesis has not been submitted either in whole or part, for a degree at this or any other university or institution.

Vienna, April 2012 _____

To my father Karl

Abstract

By utilizing computational fluid dynamics, a model for a lithium-ion cell is developed and is eventually used to predict the spatial temperature distribution across battery packs comprising twelve cells. Instead of geometrically resolving the layered structure of the jelly roll, a substitute is introduced to replace the entire jelly roll and to enable cost-effective simulations. The jelly roll substitute takes into account the anisotropy of thermal conductivity caused by the layered structure, and provides production of waste heat by applying an electric load. As the electrical conductivity of the substitute material is dependent on temperature, the model includes thermal-electrical coupling. Applying appropriate methods enables the derivation of thermal material parameters from properties of the underlying layer materials. In contrast, the electrical conductivity has to be parameterized in consideration of the dimensions and the electric boundary conditions of the substitute. For this purpose, a single cell is tested in several cycling experiments in order to acquire data on the electrical response as well as data on the temporal development of the surface temperature. The experiments are performed using different load levels and different SoC-values. Sufficient runtime is chosen to achieve thermally steady conditions. To validate the CFD model in a first step, a chosen experiment is computed using steady state analyses employing both, a realistic model including an ambient air volume and a simplified model representing heat dissipation to the environment by heat flux boundary conditions. Subsequently, transient analyses are performed using the simplified model only. The results show that all heat transfer mechanisms contribute significantly to heat dissipation in a natural convection situation.

The pack models consider three different cooling concepts in which either air or coolant act as cooling fluid. The cooling effect is implemented by conducting the cooling fluids through a unit affixed to the bottom surfaces of the cells, or through gaps located in between the cells. Several inlet conditions of the cooling fluids and modifications of characterizing design features are investigated by means of parameter studies. The heat transfer capability of each individual cooling concept as well as its resulting temperature field are evaluated. In doing so, maximum temperature and temperature homogeneity inside the jelly roll volumes are of particular interest.

Acknowledgments

This thesis was written at *AIT – Austrian Institute of Technology* (Österreichisches Forschungs- und Prüfzentrum Arsenal GmbH), in the context of a project carried out for an automobile manufacturer. The research was conducted within the *Electric Drive Technologies* business unit of AIT, which is a widely recognized development center for electric drive concepts, helping both manufacturers and suppliers to optimize the energy storage device as well as the entire powertrain.

Having finished this diploma thesis, I would like to express my appreciation to people who made my studies – and finally this thesis – possible:

I am grateful to Dr. Fiorentino Valerio Conte for giving me the opportunity to work on the project. He was the project leader and kept me free from organizational matters; he also gave me a lot of expert advice concerning the processes occurring inside the cell.
My gratitude is extended to Dr. Christian Jungreuthmayer who supported me in realizing my first great CFD project. He always had time to discuss the aspects of modeling and provided me with constructive feedback whilst allowing me to work independently.
Furthermore, I would like to show my gratitude to Ao. Univ.-Prof. Dr. Andreas Werner who agreed to supervise this diploma thesis on the part of TU Vienna. I would also like to thank him for the final assessment of the work.
This thesis would not have been possible without the support of many colleagues at AIT. In particular I would like to thank Dr. Markus Einhorn for his helpful explanations and Ing. Manfred Tadler and Kristijan Rajinovic for their important work done in the laboratory.

I am deeply thankful to my brother Lorenz who patiently improved the language of this thesis. I also appreciate that you always cared, were motivating, and gave me advice whenever I asked for it.
I would like to thank my friend and fellow student Franz Holzleithner for having a great time during our studies. Your intellectual curiosity and enthusiasm for being an engineer always inspires me.
It is a pleasure to thank my siblings Romana, Astrid, Peter, and Helene for their ongoing support during my entire studies. Each of you has contributed to my graduation in his or her own way.
Finally, I owe my deepest gratitude to my mother Edith, the way how you raised me laid the foundation for my studies. You always place value on the education of your children and you are always proud of us.

Paul Georg Oberhumer

Contents

Acronyms and Abbreviations

AIT	Austrian Institute of Technology
CAD	Computer-aided design
CFD	Computational fluid dynamics
CTU	Cell testing unit
EV	Electric vehicle
HEV	Hybrid electric vehicle
IC	Internal combustion
NMC	Nickel manganese cobalt oxide
OCV	Open-circuit voltage
PHEV	Plug-in hybrid electric vehicle
PTC	Positive temperature coefficient
SoC25	Test run with $SoC = 0.25$
SoC50	Test run with $SoC = 0.50$
SoC75	Test run with $SoC = 0.75$
SoC50oc	Test run with $SoC = 0.5$, doors of temperature chamber opened
SoC50oc2	Second test run with $SoC = 0.5$, doors of temperature chamber opened
SoC	State of charge
SoH	State of health

Nomenclature

Symbols

A	Surface	m^2
α	Heat transfer coefficient	$\mathrm{W\,m^{-2}\,K^{-1}}$
β	Isothermal compressibility	$\mathrm{K^{-1}}$
C	Capacity	Ah
c	Specific heat	$\mathrm{J\,kg^{-1}\,K^{-1}}$
D	Overall layer thickness	m
d	Thickness of material component	m
d	Gap width	m
E	Energy	J
ϵ	Emissivity	1
Gr	Grashof number	1
g	Constant of gravitation	$\mathrm{m\,s^{-2}}$
i	Current	A, C
l	Length	m
λ	Thermal conductivity	$\mathrm{W\,m^{-1}\,K^{-1}}$
μ	Dynamic viscosity	Pa s
Nu	Nußelt number	1
ν	Kinematic viscosity	$\mathrm{m^2\,s^{-1}}$
P	Power loss	W
Pr	Prandtl number	1
$\dot{Q}$	Heat flow	W
R	Thermal resistance	$\mathrm{m^2\,K\,W^{-1}}$
ρ	Density	$\mathrm{kg\,m^{-3}}$
Ra	Raygleigh number	1

Re	Reynolds number	1
S	Sutherland constant	K
s	Thickness	m
σ	Stefan-Boltzmann constant	$\mathrm{W\,m^{-2}\,K^{-4}}$
σ	Electrical conductivity	$\mathrm{S\,m^{-1}}$
T	Periodic time	s
T	Temperature	K
t	Time	s
θ	Temperature	°C
$\dot{V}$	Volume flow rate	$\mathrm{m^3\,s^{-1}}$
v	Voltage	V
y^+	Wall distance	1

Subscripts

all	Corresponding to all experiments
ap	Aramid paper
c	Corresponding to probe Center
cp	Cover plate – cooling plate
conv	Convection
e	Environment
i	Material component
l	Lateral
p	Parallel
rad	Radiation
ref	Reference
s	Series
w	Wall
∞	Ambient
0	Reference
50	Corresponding to experiment SoC50

1 Introduction

1.1 Motivation

Environmental concerns and limited resources are driving forces for replacing fossil fuels as prime energy source. A large share of consumption is caused by the use of internal combustion (IC) engines in passenger cars. Since most renewable energy technologies generate electricity from naturally replenished resources, it becomes obvious to use electricity as energy carrier in transportation as well. Moreover, the introduction of electric powertrains reduces the total energy need, which is possible through higher efficiency and the application of advanced technologies (for example recuperation of braking energy). So electric mobility plays a key role in minimizing our demand for fossil fuels.

A key component of an electric vehicle (EV), a hybrid electric vehicle (HEV), or a plug-in hybrid electric vehicle (PHEV) is the energy storage system. Typically these vehicles use a battery, which comprises series and parallel connections of (battery) cells. The performance of the various storage systems is compared by drawing a *Ragone chart*. For creating the chart, the available energy is plotted versus the available power – both values in relation to the mass of the storage system. The energy-to-mass ratio (*specific energy*) can be seen as cruising range in an EV, whereas the power-to-mass ratio (*specific power*) is equivalent to acceleration. Depending on the precise chemical composition and the layout, a battery can be designed for high energy or high power performance, as illustrated in figure 1.1.

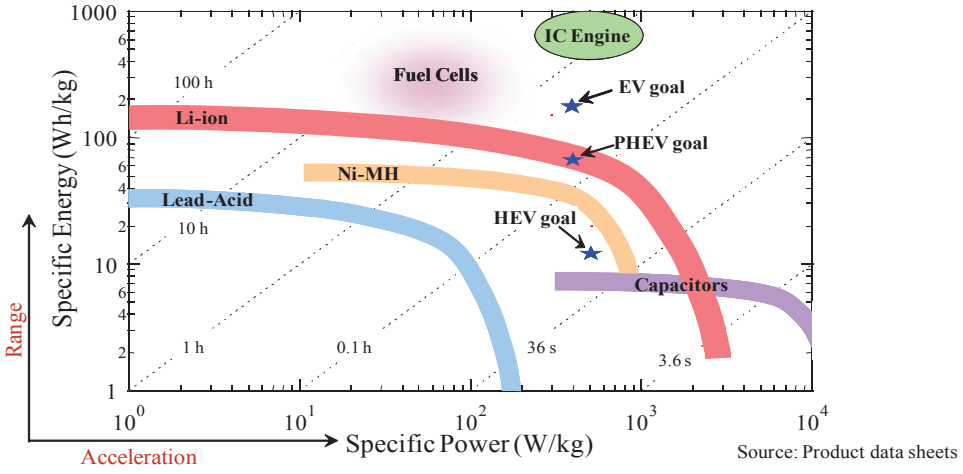

Fig. 1.1: Ragone chart [18] of various energy storage and conversion devices.

The figure points out that batteries based on *Lithium-ion* chemistry are the most preferred candidates for powering EVs. Using this type of battery offers some further positive aspects. A summary of the advantages provides the following list [15]:

- High energy density
- High power density
- High voltage
- Possibility for fast charging
- No memory effect
- Long cycle life
- Low self-discharge
- No maintenance required

Given these promising attributes enormous effort has been taken in development of lithium-ion batteries during the last decade. As a result, the estimated growth of worldwide sales of transportation battery industry increases from $ 878 million in 2010 to $ 8 billion in 2015 [16]. Nevertheless, there are still some serious drawbacks of state of the art batteries. One of them is the *aging* problem, which denotes the irreversible decrease of available energy over time and usage. In terms of battery engineering aging appears as loss of capacity and increase of impedance. One main parameter affecting the aging process is the temperature within the battery. On the one hand, a high cell temperature encourages aging, while on the other hand it increases the cell's energy and power performance. However, if the temperature reaches a critical value, the cell will run through self-reinforced chemical reactions and is eventually being destroyed (*thermal runaway*). As the weakest cell in serially connected cells determines the capacity of the whole stack, it is important that all cells offer the same capacity to ensure the maximum cruising range of the EV.

In other words, an appropriate thermal management and cooling system has to be designed for the battery. The system should provide the following characteristics:

- Prevent thermal runaway by avoiding overheating of the battery.
- Ensure an uniform temperature distribution inside the battery to prevent single cells from accelerated aging (avoidance of hot spots!).
- Adjust temperature to an intended level to achieve a desired aging behavior or battery performance.

Since it is impossible to maintain a completely uniform temperature profile across the battery, a small temperature spread is acceptable. Besides that, it should be mentioned that another main parameter affecting aging is the load. Therefore a battery management system is installed, which distributes the load evenly to all cells.

1.2 Objective and Method

In the present thesis the spatial temperature distribution across a pack consisting of twelve lithium-ion cells is analyzed. This pack is part of a battery for vehicular application, which includes 258 cells as a whole. The aim of the work is the evaluation of three

different cooling concepts concerning the homogeneity of their resulting temperature fields. Furthermore several conditions are considered in the scope of parameter studies. For this purpose a numerical model is derived which describes production of waste heat caused by electric load and heat dissipation to the cooling system and to the environment. Since the cell's internal resistance has a temperature dependence, the model undergoes thermal-electrical coupling. Furthermore, the model includes a conjugate heat transfer problem. In other words, three equations – electric potential, energy, and flow field – have to be solved simultaneously.

The work is split into three parts. In chapter 2 the experimental work performed within the framework of the project is presented. The aim of the experiments is to collect data which is used for correlation of the parameterized model describing the electric part. Furthermore, the data is used for model validation. Parameterization and validation is done in chapter 3, where a model of a single cell is developed. Finally, the cell model forms the basis to assemble the pack models. Details about the pack models and obtained results are shown in chapter 4.

The investigation is done by utilizing the software package *Star-CCM+*, a state of the art CFD (computational fluid dynamics) code developed by *CD-adapco*. It uses a finite volume discretization of the governing equations and allows doing all relevant steps (preprocessing, solving, postprocessing) for handling the problem within one software environment. In addition *Pro/ENGINEER Wildfire 5.0* is used for generating the pack geometries. Measurement results and simulation results are presented with use of *Matlab R2010b* and *MS Excel 2010*.

1.3 Basic Information about the Cell

An electrochemical cell comprises four main components: an anode, a cathode, an ionic conductor, and an electron conductor. Electrons are set free in consequence of oxidation processes at the anode and migrate through the electron conductor (and an external load/source) to the cathode, where they are consumed in reduction processes. At the same time positively charged ions are migrating through the ionic conductor from anode to cathode[1] to complete the electric circuit [15]. These processes always occur simultaneously, forming a system called redox reaction. For a rechargeable cell the process is reversed by supplying the cell with electricity. In doing so the former anode becomes the cathode and vice versa.[2] Figure 1.2 shows a schematic representation of the electrochemical process in a lithium-ion cell. A characteristic is that lithium-cations are intercalated into active materials (anode/cathode). Lithium in its metal form is not present in chemical reactions. Such active materials are adhered to metal foils for

[1] Or negatively charged ions are migrating from cathode to anode.

[2] Per definition, the anode is where oxidation occurs (negative electrode during discharge) and the cathode is where reduction occurs (positive electrode during discharge). Despite this, the negative electrode is always referred to as anode and the positive electrode is always referred to as cathode in battery engineering (irrespective of operation mode!) [12].

collecting the current. An insert, usually an electrically isolating, microporous material soaked with an electrolyte, separates anode and cathode. While this separator prohibits internal short circuiting it is permeable for ions.

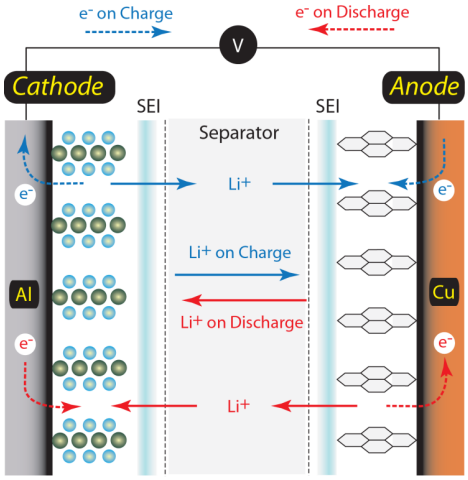

Fig. 1.2: Schematic[3]of the electrochemical process in a lithium-ion cell [14]. Lithium-cations are intercalated into anode and cathode.

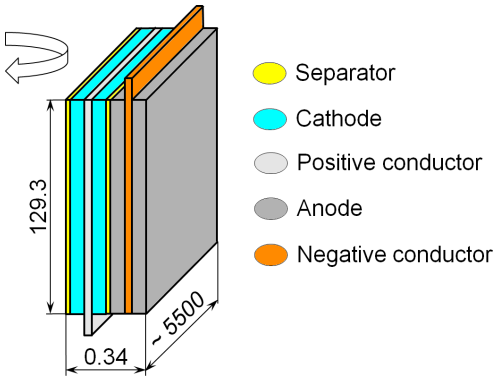

Fig. 1.3: Schematic[4] of the unwrapped electrode configuration. The arrow indicates the winding direction. Dimensions in mm.

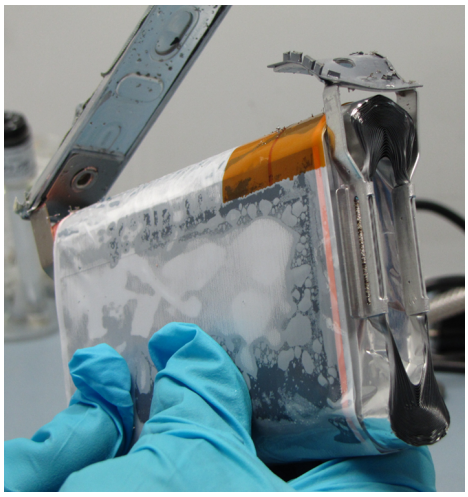

Fig. 1.4: Photograph of the jelly roll with attached current collectors [4].

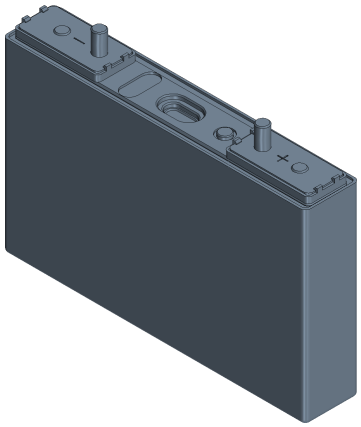

Fig. 1.5: CAD-geometry of the entire cell.

This thesis is based on a cell produced by a Japanese manufacturer. The cathode material is made of lithium nickel manganese cobalt oxide (NMC) and the anode material is graphite based. The electrolyte consists of dissolved lithium salt ($LiPF_6$) and the separator

[3]SEI: solid electrolyte interface.

[4]The schematic implies some simplifications against the real configuration: Firstly, the individual layers are not completely congruent regarding their projection perpendicular to the overall layer. Secondly, the inner turns of the winding just consists of separator material.

comprises several layers of polyolefin films. Active material is applied to both sides of the metal foils and because of a wound-up electrode configuration electrochemical processes occur on both sides. This wound-up electrode configuration is referred to as jelly roll in the following sections. Figure 1.3 provides a schematic of the unwrapped electrode configuration – attention should be paid to the dimensions. The metal foils, referred to as conductors, are protruding from the layered structure. These overlapping ends are clamped together by current collectors. The current collectors are used to connect the cell to an external circuit. A photograph of the jelly roll and the attached current collectors is presented by figure 1.4. For safety reasons the jelly roll is placed in a hard casing, which is depicted in figure 1.5. Further details on the cell structure are given in section 3.1.

1.4 Basic Principle of Modeling

Because of the thin layers – the thicknesses of the involved materials are in the range of 23 µm to 63 µm – a very fine mesh resolution would be required in the CFD model. A CFD model containing a large number of cells would lead to high memory consumption and very long simulation run times. However, high computational cost is not desired and for that reason the real jelly roll is represented by the following simplification. Instead of the complex layered structure, the jelly roll substitute comprises only four regions with rectangular cross section. In doing so, all material layers are replaced by one bulk material. The strategy is illustrated in figure 1.6.

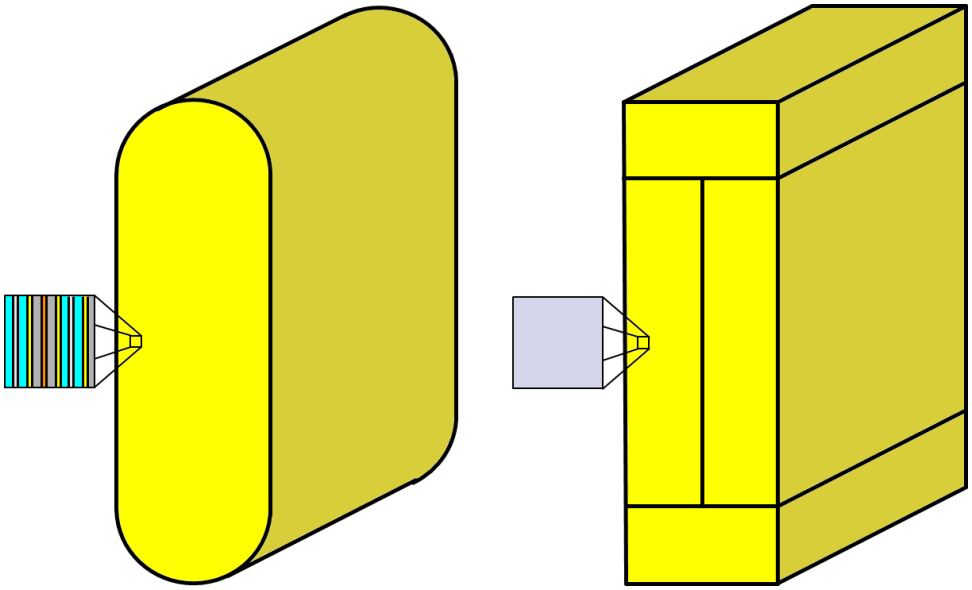

Fig. 1.6: Illustration of the jelly roll (left side) and the jelly roll substitute (right side). The complex layered structure is replaced by rectangular prisms consisting of one bulk material. The properties of the bulk material are adapted using appropriate approaches.

As a consequence, electric boundary conditions and material properties have to be adapted accordingly. Thermal properties are derived from the layer materials, whereas the electric behavior cannot be described accurately because of lacking information. Therefore, a parameterization based on experimental results is being applied. The jelly roll substitute considers following main aspects:

- Representation of anisotropic thermal conductivity (section 3.3.1)
- Prediction of electrical power loss (section 3.3.2)
- Representation of current density orientation (section 3.6.1)

2 Experimental Work

The aim of the experimental work is to collect data which is used to parameterize the temperature-dependent electrical resistance of the bulk material and to validate the CFD model of the cell. For this purpose the cell is subjected to specially defined load sequences and electric response as well as thermal development are measured. In the first section a few essential terms regarding cells and batteries are explained. Then the experimental setup is presented, followed by the test sequence and the last section discusses test results.

2.1 Terms and Definitions

Equivalent Circuit

The equivalent circuit of a cell represents the cell's electric behavior and comprises resistors, capacitors, inductors, and an idealized voltage source. Depending on modeling accuracy, more or less of these elements are considered. A common model consists of one ohmic resistor R_i, a parallel combination of one resistor and one capacitor (R_a, C_a), and a voltage source named *open-circuit voltage* (OCV). The circuit diagram of this model is depicted in figure 2.1. Thereby is v the terminal voltage and i the terminal current. The simplest model just consists of one ohmic resistor R_i and a voltage source.

Internal Resistance

The OCV designates the equilibrium state under idle condition and can be derived from the thermodynamic formulation of chemical reactions. When current is drawn from the cell, voltage drops off because of kinetic limitations of electrode reactions[1] (*electrode polarization* or *overvoltage*) and of the cell's internal resistance [21, 15]. The internal resistance includes the ionic resistance of electrolyte, the electronic resistances of electrodes, of conductors, and of current collectors and the contact resistance between active mass and conductors. These resistances are ohmic[2] in nature and generate waste heat under operation (also known as Joule or ohmic heating). That means part of the stored energy is consumed as power loss. In addition, heat is released/absorbed because

[1] Basically, two effects have to be considered: *activation polarization* is related to the kinetics of the charge-transfer reactions taking place at the electrode/electrolyte interfaces of anode and cathode and *concentration polarization* is due to mass transport limitations during cell operation. [21]

[2] The voltage drop due to internal resistance is usually referred to as *ohmic polarization*.

of the thermodynamic reversible heat effect of chemical reactions.[3] As temperature enhances diffusion processes, internal resistance decreases with rising temperature.

Capacity

The energy E, available from a fully charged cell, is defined by time-integrating power output (2.1) over discharging time t_d:

$$E = \int_0^{t_d} v(t)\, i(t)\, \mathrm{d}t \tag{2.1}$$

$$C = \int_0^{t_d} i(t)\, \mathrm{d}t \tag{2.2}$$

Time integration of discharge current (2.2) gives the delivered electric charge and is called capacity C, given in units of ampere-hours or coulombs. In battery engineering capacity is usually used to classify cells since power loss, and therefore available energy, is a function of loading. In order to rate capacity, manufacturers specify nominal load and temperature conditions. Because of different operating conditions in real applications, the rated capacity can not be fully exhausted, or even exceeded in service. In a serial connection of *equal* cells the overall potential is the sum of the individual terminal voltages, whereas the capacity remains at the single cell's value.

C-Rate

Commonly discharge, as well as charge current, is expressed as multiple of the rated capacity:

$$i = F\, C_\mathrm{n} \tag{2.3}$$

To be dimensionally correct, the numerical value of the capacity C_n has to be taken. The variable F expresses an arbitrary factor. The simulated cell is rated to a capacity of $C = 22.5\,\mathrm{A\,h}$, hence a current of rate $1C$ follows to $i = 22.5\,\mathrm{A}$. It takes approximately one hour to discharge the fully charged cell under this load.

Performance and State of Charge

The performance of a battery or cell generally depends on several factors [15]:

- Load
- Temperature
- Cycle life
- Storage
- Load history
- Charging method
- Battery design
- Variations in manufacturing

[3] Chemical reactions are either exothermic or endothermic and the heat of a reaction can be split into reversible and irreversible produced heat. The irreversible part, which is always exothermic, is already included with Joule heating.

The ability to deliver rated capacity is reflected by a figure of merit called *state of health* (SoH). The SoH represents present charge storage capability compared to fresh (new) state and is given in units of percent points.[4] During service and lifetime SoH is continuously deteriorating because of irreversible physical and chemical changes. Power performance also deteriorates because of a rising cell impedance. As already mentioned, the diminishing of performance is called *aging*. Another quantity which describes battery condition is defined as *state of charge* (SoC). The SoC gives present charge state in relation to present charge storage capability and is given in units of percent points.[5] Equivalent to this, information about the charge state is provided by the OCV. The typical correlation between SoC and OCV for a lithium-ion chemistry is presented in figure 2.2. The voltage bounds (V_l, V_u) are defined by the participants of chemical reactions and determine the range of cell operation.[6] Hence, if cells with *different* capacity are connected serially, the weakest cell (worst capacity) will be fully charged/discharged at first and will define the stack capacity. The voltage bounds of the simulated cell are $V_u = 4.1\,V$ and $V_l = 2.5\,V$, respectively. The nominal cell voltage is given as $V_n = 3.67\,V$, which represents OCV at $SoC = 50\,\%$.

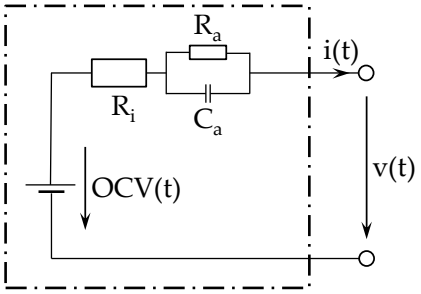

Fig. 2.1: Cell equivalent circuit diagram.

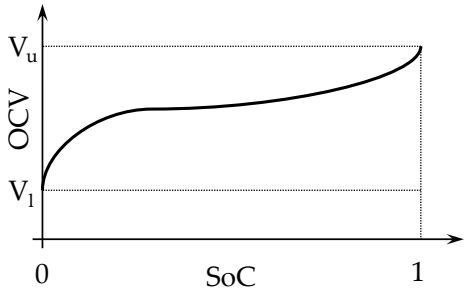

Fig. 2.2: Schematic relationship between open-circuit voltage and state of charge.

In summary, specification of OCV-SoC characteristic, equivalent circuit elements (R_i, R_a, C_a), capacity C, SoC, and SoH enables a complete, electric description of a battery.

2.2 Experimental Setup

The following quantities are of interest:

- Internal resistance as a function of temperature
- Cell temperature development due to electric load

[4] $SoH = 1$: the performance matches the data sheet specifications.

[5] $SoC = 1$: the battery is fully charged.

[6] Operating beyond the bounds leads to cell damage: Charging with large over-voltage will introduce disintegration of the electrolyte, and discharging to a low voltage causes corrosion of the negative conductor.

As resistance cannot be measured directly, it has to be calculated from power loss. One possibility for determining power loss is to detect waste heat by utilizing a calorimeter, which unfortunately has not been available. Instead of detecting waste heat, power loss is calculated from transferred power. Therefore a special load profile is necessary. Section 3.3.2.1 explains this approach in detail. An AIT-made device called CTU (cell testing unit) provides the load and records terminal current, terminal voltage, and runtime with a sampling rate of 2 Hz.

Temperature is obtained from probes attached to the cell surface. To secure an accurate measurement, the probes (PTC sensors) are stuck on the surface using a heat-conducting paste. Additionally, a retainer provides a firm package for handling. It consists of two plates housing the probes (made of plastic, referred to as socket plates), which are encased by sheet steel. Figure 2.3 shows a photograph of the experimental setup. Although sixteen probes are available, only three of them will be used[7]. Their location and names are depicted in figure 2.4. Ambient temperature is also obtained by a probe positioned in proximity of the cell. Temperature data is acquired with a sampling rate of 10 Hz by utilizing a Cronos-PL-16 measurement system. Terminal voltage is detected again to enable synchronization of temperature data (Cronos) and electrical data (CTU).[8]

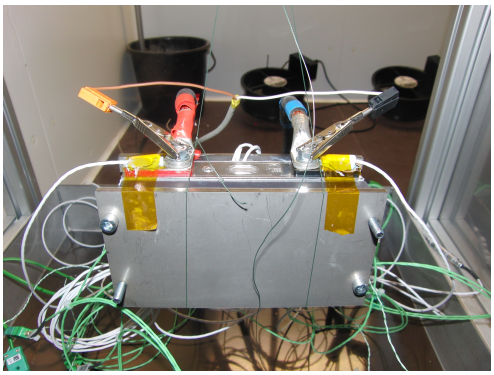

Fig. 2.3: Experimental setup.

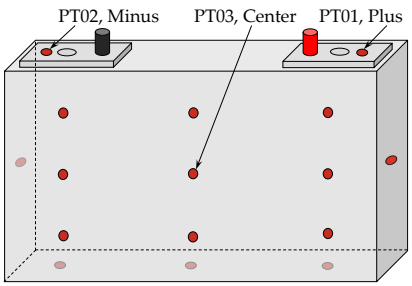

Fig. 2.4: Location and names of probes.

The experiment is simulated to validate the CFD model. In doing so, heat dissipation to environment has to be modeled. Therefore, the boundary conditions of the experiment have to be chosen in an easily reproducible manner. In order to optimize computational cost, the volume surrounding the cell model has to be as small as possible. These reasons lead to following requirements of the test setup. Firstly, the cell is hang-up to avoid head conduction to any adjacent hardware. Secondly, the experiments are carried out in

[7] Because of the excellent thermal conductivity of casing material and the isolating effect of the socket plates, a rather small temperature spread is developing at the casing side wall. Considering all probes does not add any meaningful information.

[8] In order to parameterize internal resistance (section 3.3.2 on page 32), CTU data and Cronos data are combined (page 34). In doing so, Cronos data is resampled to a frequency of 2 Hz by utilizing the Matlab command *resample()*. While synchronizing, a spread between the two time series was detected. Over a time period of 3 h, the spread amounts to a negligible delay of about 1 s.

quiescent air. As a result a natural convection situation develops, and the environment can be shrunken to a volume which just encloses the disturbed air around the cell. More details about modeling boundary conditions are given in section 3.3.1.2.

However, the experiments are carried out within a temperature chamber. The photograph in figure 2.5 shows the thermally isolated room. The chamber is equipped with several test ports, an air conditioning system to ensure a certain temperature, and a fire sprinkling system. In addition to the integrated fans of the air conditioning, a few extra fans enhance heat dissipation of the test objects by generating a forced convection situation. That is the setup of the first experiment. As noted, great care should be taken to disturb air as less as possible. Thus, the extra fans are turned off during the second and third experiment. Further on, air conditioning is turned off as well and heating-up of the chamber is avoided by opening its doors. Interference from other laboratory operations is prevented by performing the experiments during night.

The CTU provides power cables with a cross-sectional size of 35 mm^2, which are attached to the cell using adapters (short cables with a cross-sectional size of 10 mm^2). These were removed after the third experiment. In summary, three different setups are used. They are clearly presented in table 2.1 in the next section.

Fig. 2.5: Temperature chamber. Each CTU (black devices) serves six test ports.

2.3 Definition of Test Sequence

Since power loss is small in comparison to terminal power and the cell has a moderate heat capacity, load has to be applied for a long time period to obtain a reasonable increase of the surface temperature. In order to prevent the cell from complete discharging, the cell is burdened alternately with charging and discharging periods. The application of such a load is referred to as *cycling*. As load profile a square wave with periodic time $T = 20\,\mathrm{s}$ and amplitude i is chosen:

$$i(t) = \begin{cases} +i & \text{if: } (k-1)\,T < t \leq (2\,k-1)\,T/2 \\ -i & \text{if: } (2\,k-1)\,T/2 < t \leq k\,T \end{cases} \qquad \text{with: } k = 1, 2, \ldots \tag{2.4}$$

Figure 2.6 gives a short period of the cell's voltage response due to the applied current profile (positive current corresponds to charging). The voltage profile shows a strongly

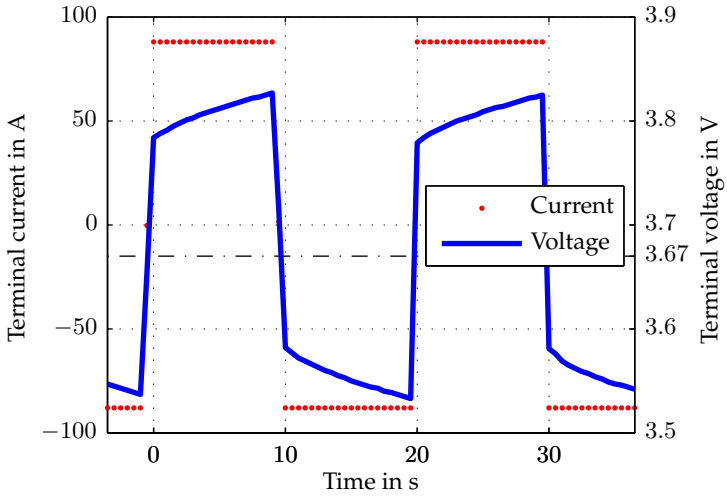

Fig. 2.6: Voltage response for cycling with $i = 4C$ and $SoC = 0.5$ ($OCV = 3.67\,\mathrm{V}$).

nonlinear response. The jump discontinuities are caused from the resistive component of cell impedance, whereas the increasing/decreasing edge is affected by (mainly) capacitive characteristics.[9] Over one cycle period the transferred charge integrates to zero, as a result the SoC remains at a constant level during cycling. The thermodynamic reversible heat effect cancels out as well. Hence, the parametrization of internal resistance will only capture irreversible effects.

The experiments are done using different SoC values and different load amplitudes. At the beginning of the test, the target-SoC is adjusted. Then the cell is stored until cell temperature is balanced with ambient temperature. After staring the experiment a general procedure is followed:

[9] For that reason, at least one capacitor-resistor element should be inserted into the equivalent circuit if a description of voltage is desired.

SoC adjustment → short cooling-off time → cycling (amplitude i_1) → long cooling-off time → Soc adjustment → short cooling-off time → cycling (amplitude $i_2 < i_1$) → ⋯

At the beginning the SoC is adjusted to compensate self-discharge, afterwards a short cooling-off time of 0.5 h follows. Then testing continues with cycling. A long cooling-off time, lasting as long as cycling duration, takes place subsequently. To compensate self-discharge, further SoC adjustment and short waiting time are appended. Then cycling starts again with another current level. During the whole experiment a temperature stopping criterion of 45 °C as well as above mentioned voltage bounds are defined. Table 2.1 gives an overview of the experiment conditions.

Name of test run	Sequence of load amplitudes[10]	Cycling duration	Connector cable	Air c.[11]	Ambient temp.[12]	Comment
SoC50	4C - 3C - 2C - 1C	3 h	10 mm^2	on	15 °C	extra fans on
SoC75	4C - 3C - 2C	3 h	10 mm^2	on	15 °C	extra fans off
SoC25	4C - 3C - 2C	3 h	10 mm^2	on	15 °C	extra fans off
SoC50oc	4C - 3C	4 h	35 mm^2	off	≈ 19 °C	open chamber
SoC50oc2	2C - 1C	4 h	35 mm^2	off	≈ 23 °C	open chamber

Tab. 2.1: Overview of experiment conditions.

2.4 Discussion of Test Results

Basically, all test runs show the same characteristic behavior. As case SoC50oc is used for validation later on, it is chosen to be presented. Figure 2.7 illustrates electrical data of the complete test run as a function of time, in which the interval of first SoC-adjustment is cut off.

The figure shows that the entire experiment lasts for about 17 h. During the first cycling period the charge voltage decreases from $v = 3.83$ V at time $t = 0$ h to a value of $v = 3.78$ V at time $t = 4$ h, whereas the discharge voltage increases from $v = 3.53$ V at time $t = 0$ h to a value of $v = 3.57$ V at time $t = 4$ h. This is caused by rising of cell temperature and therefore a reducing internal resistance. The constant voltage levels after a cycling period of about three hours ($t \approx 3$ h and $t \approx 11.6$ h) clearly indicate that a thermal steady state is reached. During power-off time a OCV drop of about 6 mV occurs whose adjustment is recognized as small peak in the current profile. The adjustment lasts on average for 3.5 min with a maximal current of about 8 A, which does not produce enough waste heat to obtain a temperature rise.

[10] To be exact: the cycling was done using $1C = 22$ A, $2C = 44$ A ....
[11] Air conditioning.
[12] Ambient temperature.

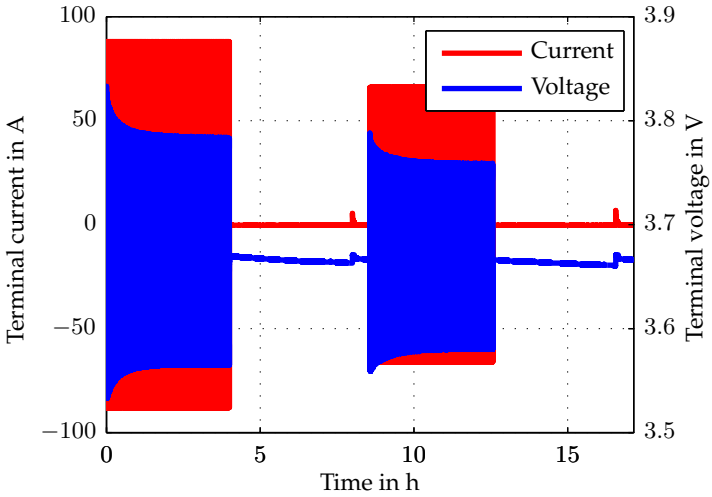

Fig. 2.7: Terminal current and terminal voltage for test run SoC50oc.

The temporal development of cell temperature is illustrated in figure 2.8, which compares the values of probe *Center* for all test runs. As the experiments are performed under various ambient temperatures, the temperature difference between probe and environment is used to maintain comparability. The plot clearly indicates the cycling periods, where temperature rises from ambient level to peak level at the end of the respective cycling period. Then the cell cools down do ambient level again. The difference between curves SoC75 and SoC25 points out that internal resistance is a function of SoC as well.

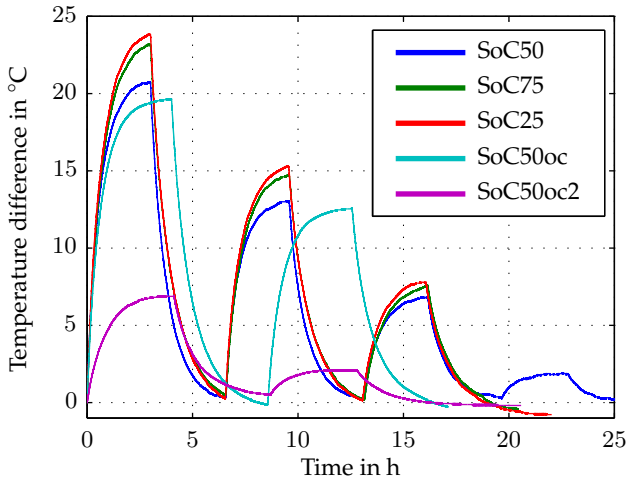

Fig. 2.8: Temperature difference between environment and probe *Center* for all test runs.

Although experiments SoC75, SoC25, and SoC50 are performed at the same ambient temperature level, the SoC50 experiment clearly takes course at a lower level. This is caused by the extra fans and thus an increased heat dissipation. However, experiment

SoC50 achieves higher temperatures than experiment SoC50oc, even though higher heat transfer (forced ⇔ natural convection) and lower ambient temperature (15 °C ⇔ 19 °C). This discrepancy is caused by additional heat, which is fed into the cell at the terminals. This additional heat is generated by the adapters (used in experiments SoC50, SoC75, and SoC25), which offer larger Joule heating than the CTU power cables because of less cross-sectional area. Figure 2.9 attests this effect. There the data of probes *Plus*, *Minus*, and *Center* of experiments SoC50oc and SoC25 are plotted. The terminals show higher temperatures than probe Center for experiment SoC25, where the adapters are used. The effect vanishes for the last cycling period, which means heat dissipation through the cables exceeds ohmic heat generation. Different thermal conductivities of terminal materials cause the temperature difference between probes Plus and Minus.

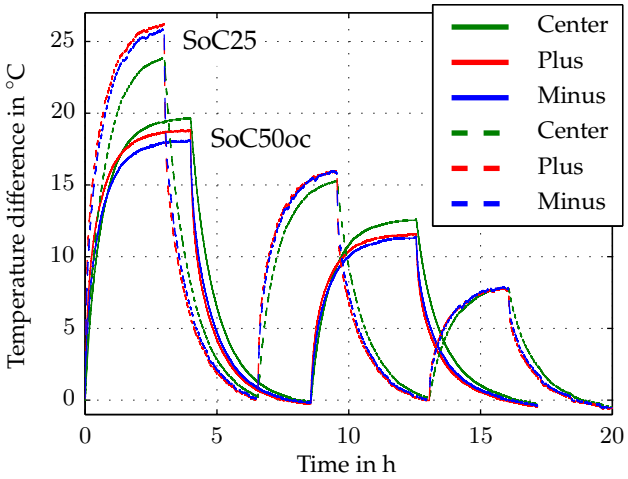

Fig. 2.9: Temperature differences between environment and main probes for test runs SoC25 (adapters used) and SoC50oc (adapters not used).

3 Cell Model

This chapter describes the model development for a single cell. The aim is to create a three-dimensional CFD model to predict the spatial temperature distribution across the cell. The first section presents a slightly simplified geometry derived from real cell geometry. This simplified geometry forms the basis for the mesh, which is generated in the second section. The next section presents the completion of the entire CFD model, a combination of mesh, physical model setup, numerical solver setting as well as various post-processing features. Thermal properties and heat dissipation are considered in subsection *Thermic Model*, whereas all electric issues are covered in the subsection called *Electric Model*. Subsequently, results of the steady state simulations and of the transient simulations including a validation of the CFD model are discussed. The last section covers a few general modeling aspects.

As mentioned before, the experiments are recomputed for validation, and thus test conditions have to be reproduced. From this it follows that not only the cell, also the retainer of the probes must be included in the model. The interaction with the environment has to be be considered by applying appropriate boundary conditions. Therefore two model variations are developed. For the first approach the model includes the environment in form of a rectangular cuboid enclosing the cell, which is referred to as *air box model*. The second approach uses an analytical formula to describe the interaction, and the control volume just consists of cell and retainer. This is referred to as *plain cell model*.

3.1 Geometry

The geometry generation is based on information [4] provided by the project partner. The information include installation dimensions (working drawing) and data (photographs, dimensions) which were obtained from disassembling a cell. The geometry is generated by utilizing *3D-CAD*, which is a parametric solid modeler and fully integrated within the Star-CCM+ software environment.[1] A schematic representation of the cell assembly is shown in figure 3.1. The overall dimensions are 148 mm · 26.5 mm · 105.3 mm, excluding terminals the height totals to 91 mm. Beside jelly roll, current collectors, and casing, the cell comprises insulators to separate the electric parts from the casing as well as safety devices (PTC-element, overpressure valve integrated at the casing lid). Additionally the jelly roll as a whole is wrapped into an isolating film as well. According to the basic

[1] Compare remark on page 18.

modeling principle explained in section 1.4, the jelly roll is replaced by a rectangular prism. To reduce complexity, geometric details without relevance in thermal behavior are neglected. In summary, the geometric simplifications are:

- Jelly roll replaced by a rectangular prism
- Radii of casing (edges) not modeled
- Inside insulators ①, insulation film ②, and PTC-element ③ neglected (compare figure 3.1)
- Simplified casing lid (no overpressure valve, plane structure without stamping)
- Simplified terminals (no thread) and top insulators (no bordering)
- Straight shape of current collectors (orange parts), no radii
- Current collector assemblies replaced by single parts

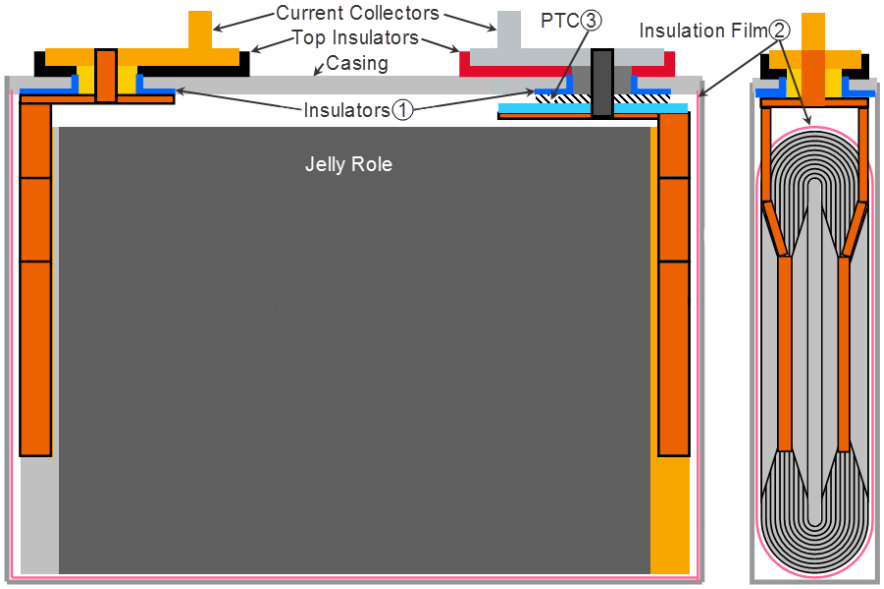

Fig. 3.1: Schematic representation of cell assembly.

The protruding conductor ends are cropped and the current collectors are directly attached to the jelly roll. Consequently, the jelly roll fills out the space between inner casing surfaces (transverse) and current collectors (longitudinal). Furthermore, the jelly roll has to be divided into five segments to gain an adequate basis for applying electric boundary conditions. Further details on this are provided in section 3.3.2. The remaining free volume is filled with air and referred to as cavity. As indicated in the figure, although each current collector consists of several parts these assemblies are being replaced by one single part as representation. The top insulators are modeled to maintain correct height of the terminals, but the bordering of the terminal plates is disregarded. As the probes retainer is also included, socket and steel plates are depicted as flat, rectangular prisms with dimensions $(148 \cdot 9.6 \cdot 90)$ mm and $(170 \cdot 4.6 \cdot 90)$ mm, respectively. The milled out

hollow space as well as temperature probes are not modeled. The screws are represented by straight cylinders. Figure 3.2 shows the used cell geometry, in which the casing is displayed transparent and the cavity volume is faded out for visualization reasons. The retainer and jelly roll segments can be seen in figure 3.3 in the next section. Referring to the air box model, the environment is created in shape of a rectangular box with dimensions $0.6\,\mathrm{m} \cdot 0.55\,\mathrm{m} \cdot 0.5\,\mathrm{m}$ (length/depth/height). The distance from box bottom side to cell bottom side is 175 mm, apart from that the cell is positioned in the center of the box. This geometry is depicted in figure 3.8 on page 28.

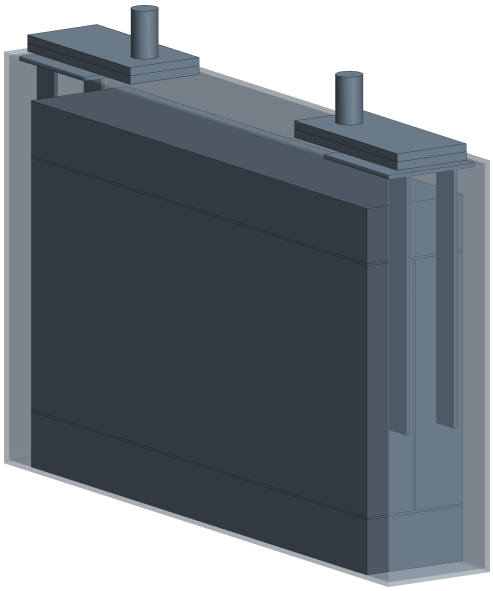

Fig. 3.2: Cell geometry, generated with 3D-CAD.

Remark: *Procedure of model generation in Star-CCM+*: The next step after drawing is exporting the created bodies to geometry parts, then each part consists of a set of surfaces and curves. Subsequently, geometry parts are assigned to regions, which is tantamount to link them with meshing models and physical models. After running the mesh generation process, a region provides the discretized, mathematical description of the problem being solved. These regions are completely surrounded by boundaries. If a region adjoins another one and information has to be exchanged across the boundary, the adjacent surfaces are connected by an *interface*. Regions are not necessarily contiguous volume domains. It is possible to combine all parts with common physical models, for example all parts made of aluminum are assigned to the same region. This is not done for the sake of convenient handling, meaning that each single part is represented by a single region. In summary, depth of modeling is easily observable from denotation. Within the 3D-CAD module different elements are called bodies, they become parts after exporting to geometry level, and they are assigned to regions finally.

One of the great advantages of using the integrated CAD module is the generation of part contact data for coincident faces by running the operation *Imprint*. It causes the curves from two (or more) bodies to be pasted onto the faces where they meet. The affected faces are automatically split by newly generated curves. So patches of common extent are generated. Neither surface repair nor similar actions have to be set on geometry level, the parts can be directly assigned to regions. It is very useful that interfaces can be *automatically* created of existing part contact data during assignment process. To create *all* possible interfaces, it is crucial that all parts are assigned to new regions in a *single* operation.

3.2 Mesh

The mesh is produced using the *Polyhedral Meshing Model* and its sub methods *Embedded Thin Mesher* and *Prism Layer Mesh*. A polyhedral mesh has got advantages in accuracy and robustness and uses fewer cells than an equivalent tetrahedral mesh; it represents the latest technology. The thin mesher is applied to domains with low thickness and generates a prismatic type volume mesh. This is advantageous in terms of cell count and cell quality in thin, narrow volumes. On the other hand, a prism layer mesh is always attached to boundaries or interfaces which are adjacent to fluid domains. These are the cavity surface and faces contacting environment. Especially if a turbulence model is used, a prism layer mesh will be needed for accurate simulation of turbulence and heat transfer near a wall. However, the prism layer thickness is approximated with an analytical approach for natural convection at a vertical plate with constant wall temperature. Therefore ambient air is assumed to be an ideal gas and the thickness of a laminar boundary layer is given by [17]:

$$\delta \sim l\, Gr^{-\frac{1}{4}} \qquad \text{with:} \tag{3.1}$$

$$Ra = Gr\ Pr = \frac{\beta_\infty\, (\theta_\mathrm{w} - \theta_\infty)\, g\, {l_\mathrm{ref}}^3}{{\nu_\infty}^2}\, Pr_\infty \tag{3.2}$$

In equation (3.2) stands Gr for the *Grashof number* and Ra for the *Rayleigh number*, both of which are dimensionless quantities.[2] They have to be calculated with fluid parameters at ambient temperature level. Applicability of the laminar approach is given for $Ra \leq Ra_{crit} = 10^9$, [3]. Table 3.1 lists parameters and results.

Temperature of wall	θ_w	38	°C
Temperature of environment	θ_∞	19	°C
Constant of gravitation	g	9.81	$\mathrm{m\,s^{-2}}$
Isothermal compressibility	β_∞	$3.4229 \cdot 10^{-3}$	$\mathrm{K^{-1}}$
Wall height	l_ref	$9.1000 \cdot 10^{-2}$	m
Kinematic viscosity	ν_∞	$1.5255 \cdot 10^{-5}$	$\mathrm{m^2\,s^{-1}}$
Prandtl number	Pr_∞	$7.1490 \cdot 10^{-1}$	
Grashof number	Gr	$2.0659 \cdot 10^6$	
Rayleigh number	Ra	$1.4769 \cdot 10^6$	

Tab. 3.1: Grashof- and Rayleigh number for natural convection at a vertical plate, using the casing height as reference length and temperatures[3] obtained in experiment SoC50oc ($i = 4C$, $t = 4\,\mathrm{h}$).

At the casing wall's top end the boundary layer thickness is approximated to $\delta(l_\mathrm{ref}) = 2.4\,\mathrm{mm}$. Thus, prism mesh thickness is set to a value of 3 mm. As the assumption of

[2] The Grashof number describes the ratio of buoyancy forces to viscous forces and the Rayleigh number whether heat is transferred through convection or conduction (in natural convection flows).

[3] The real wall temperature is slightly lower and not constant, but this does not matter for an approximation.

undisturbed vicinity is violated inside the cell, this approach cannot be used to determine the cavity surface mesh parameters. Moreover, a much smaller temperature gradient occurs, the volume is closed, and therefore little air circulation is expected. In the end, similar – but arbitrary – prism mesh parameters are set. Further on, the thin mesher is set to capture structures below 1 mm thickness. As most important reference value of the polyhedral mesher, a *base size* of 8 mm is entered. Local refinement areas are defined around the screws and terminal bolts. Finally, the air box model contains about 1 740 000 cells. The plain cell model achieves a cell count of about 130 000, excluding the retainer of about 95 000. Figure 3.3 shows the transverse section through the center of the air box mesh.

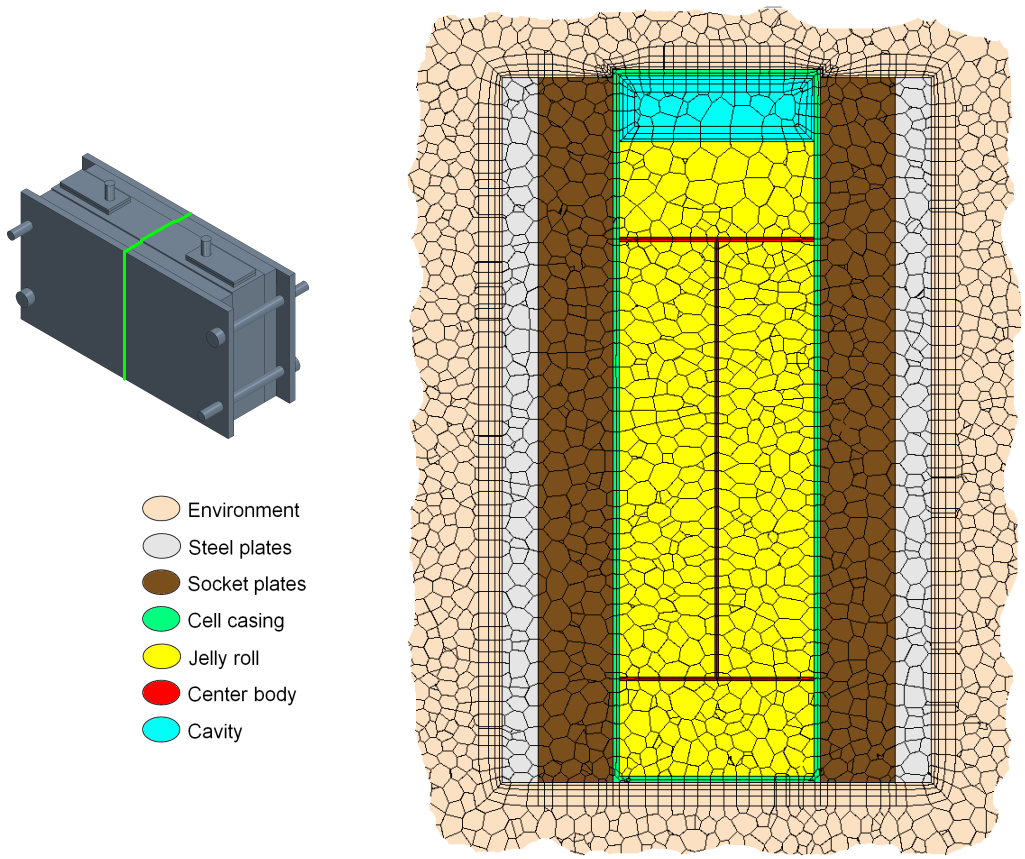

Fig. 3.3: Transverse section through center of the air box mesh, section plane location indicated in the small picture. The structured areas are the results of the mesher sub methods. The jelly roll is divided into five segments (Jelly roll and Center body).

3.3 Physical Models

First of all, the basic physical behavior is briefly discussed. Heat, which is generated due to electric load within the jelly roll, is transfered to the outer surface and dissipated

there. As the liquid electrolyte shows strongly limited mobility and the whole cell is an opaque system, conduction is the main mechanism for heat transfer. The conductors have a much higher thermal conductivity than the active materials, and therefore heat conduction parallel to the layered structure is much higher than perpendicular to the layers. This fact is considered by an anisotropic thermal conductivity of the bulk material. Furthermore density and specific heat capacity of the bulk material has to be determined, since both properties affect the thermal behavior of the system. The bulk material as well as all other cell components are modeled as solid material continua. On the other hand, the air within the cavity and surrounding volume is represented as fluid continua, to be more precise as ideal gas. Since flow is only driven by buoyancy, it is prescribed sufficiently close by a laminar flow model ($Ra \leq Ra_{crit}$). At solid walls a no-slip condition is applied. *For comparison only*, a simulation is performed in which description of ambient air flow is changed. In doing so, the laminar model is replaced by a turbulence model. Therefore the *Realizable Two-Layer k-ϵ Model* [7] is chosen, which combines the sophisticated *realizable k-ϵ* description of turbulence with the *two-layer approach*. This model is capable of resolving the viscous sublayer for an appropriate fine mesh.

In the CFD model each component is represented by a region. Regions are discretized by a mesh and associated with physical models. Information between adjacent regions can be passed by connecting the boundaries with common interfaces. A *contact interface* permits conjugate heat transfer between two regions[4], therefore this interface type is applied to all interfaces.

The governing equations are energy, electric potential and flow. While the energy equation is solved for all regions, the flow equations are only assigned to fluid regions and the electric potential equation is only assigned to the jelly roll region. Using Joule's law, the electric potential equation provides the density of dissipated power which gives a source term in the energy equation. The outcome of the energy equation is temperature which influences electric conductivity and in turn dissipated power. The solution variables (temperature, electric potential, velocity, pressure) are obtained using segregated solvers. Under-relaxation factors have to be increased to achieve a satisfying rate of convergence. Table 3.2 compares chosen settings with default values.

Factor	Default	Modified
Fluid energy	0.9	0.95
Solid energy	0.99	0.999
Velocity	0.7	0.8
Pressure	0.3	0.4
Electric potential	0.99	0.99

Tab. 3.2: Under-relaxation factors.

[4] At least one of them has to be a solid region.

As heat conduction dominates the problem, marked improvement of convergence rate is obtained by increasing the under-relaxation factor for solid energy. Additionally, *Cell Quality Remediation* is activated. This option modifies computed gradients of poor-quality cells in such a way as to improve the robustness of the solution. Steady state analyses as well as a transient simulations are being computed. For the latter, unsteady terms have to be considered by a time model. In conjunction with segregated flow and energy models only an *implicit unsteady* approach is available. The model demands entering of parameters *physical time-step* and *maximum inner iterations*. A time step of 10 s gives adequate time resolution, and 20 inner iterations are sufficient to reach convergence for each time step.

3.3.1 Thermic Model

The neglected insulators between current collectors and casing are taken into account by introducing *thermal contact resistances* at the associated interfaces. For a given heat flux $\dot{q}$, contact resistance R causes a temperature drop ΔT across the interface. The contact resistance is determined by comparison with one-dimensional, steady state heat conduction:

$$\Delta T = \dot{q}\, R \tag{3.3}$$

$$\Delta T = \dot{q}\, \frac{s}{\lambda} \tag{3.4}$$

$$\Rightarrow\ R = \frac{s}{\lambda} \tag{3.5}$$

Insulator thickness s and thermal conductivity λ are virtually added to the interface. This approach disregards heat conduction within the neglected component, as well as insulator mass. This does not matter in consideration of the small insulator thickness and the large differences in thermal conductivity/density between insulator and adjacent materials. Figure 3.4 explains the effect of introducing a thermal contact resistance at an interface. The neglected PTC-element has ideal thermal properties and does not have to be considered at all.

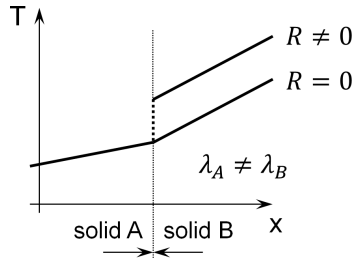

Fig. 3.4: Temperature drop across an interface resulting from thermal contact resistance R.

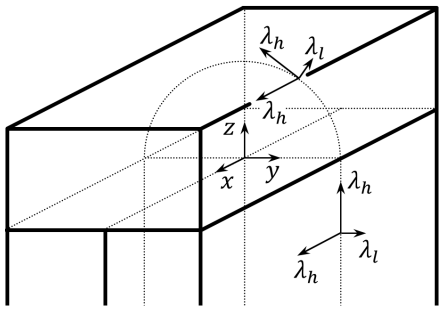

Fig. 3.5: Local coordinate system and orientation of the anisotropic thermal conductivity (λ_{high}, λ_{low}).

The thermal conductivity of the jelly roll is modeled by an anisotropic tensor profile. Because of the wound configuration, anisotropy depends on the position. Figure 3.5 illustrates this behavior. The top and bottom segments are adequately mapped by an axisymmetric formulation. In doing so, local coordinate systems have to be introduced. The position of the top coordinate system is indicated in figure 3.5. The remaining segments are modeled by a principal axis formulation.

3.3.1.1 Parameters

As mentioned above, required solid material parameters are thermal conductivity λ, density ρ, and specific heat c. Referring to the jelly roll bulk material, equivalent thermal circuits are used to determine thermal conductivities parallel (λ_p) and perpendicular (λ_s) to layers. They are indicated in figure 3.6. Mass density of the bulk material has to be calculated by adding up weighted densities of the underlying materials. To be more precise, weighting has to be done by using the volume fraction of individual layer to overall layer. In similar manner, specific heat of the bulk material is determined. Therefore specific heats of the underlying materials, weighted by the fraction of their individual layer mass to total layer mass, are summarized.

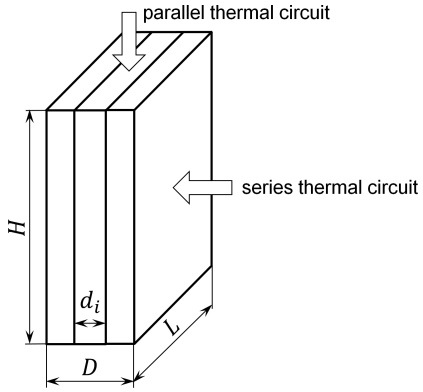

Fig. 3.6: Sketch for determination of bulk material properties.

Considering D as overall layer thickness and d_i as thickness of material component i, parameters of the bulk material are expressed by:

$$\lambda_s = D \left(\sum_i \frac{d_i}{\lambda_i} \right)^{-1} \tag{3.6}$$

$$\lambda_p = \left(\sum_i d_i \, \lambda_i \right) D^{-1} \tag{3.7}$$

$$\rho = \sum_i \rho_i \, \frac{d_i}{D} \tag{3.8}$$

$$c = \sum_i c_i \, \frac{\rho_i \, d_i}{\rho \, D} \tag{3.9}$$

Since the separator consists of insert and electrolyte, its material properties has to be determined in the same way. Therefore an usual insert porosity of 45% is assumed. Another assumption is that all pores are completely filled with electrolyte. Then thermal conductivity of the porous material is calculated with a simple parallel model, sometimes referred to as *Wiener Bounds* [5]. Again, density/specific heat are determined by totaling values which are weighted with volume/mass fraction. Table 3.3 gives the separator values.

Name	Material	Volume fraction	Mass fraction	Density	Specific heat	Thermal conductivity	Reference
				$\mathrm{kg\,m^{-3}}$	$\mathrm{J\,kg^{-1}\,K^{-1}}$	$\mathrm{W\,m^{-1}\,K^{-1}}$	
Insert	PP/PE	0.55	0.46	895	1978	0.334	[10]
Electrolyte	$LiPF_6$	0.45	0.54	1290	133.9	0.45	[10]
Separator	absorbed			1073	979.9	0.39	

Tab. 3.3: Material properties of the separator.

Thicknesses of layer components are provided by the project partner, whereas detailed information on material properties are lacking. For this reason properties are taken from literature. These do not correspond to the actual material composition, but meet the correct range. While a steady state temperature field just depends on thermal conductivity, temporal development of transient solutions is influenced by heat storage capability. Since the jelly roll has less volume than its substitute, the bulk density is approximated more precisely by the real jelly roll mass (table 3.4) and the substitute volume (figure 3.7). Jelly roll mass is obtained by subtracting mass of individual cell components from the overall cell mass. The individual component masses are calculated by integrating density over volume in Star-CCM+. For neglected components an estimation is made. Finally, the bulk material properties are listed in table 3.5.

Name	Mass	Reference
	g	
Entire cell	690	[11]
Casing	84	CCM+
Current Collector pos.	8	CCM+
Current Collector neg.	25	CCM+
Top insulators	3	CCM+
Miscellaneous	6	estimation
Jelly roll	565	

Tab. 3.4: Masses of cell components. CCM+: determined by CFD model.

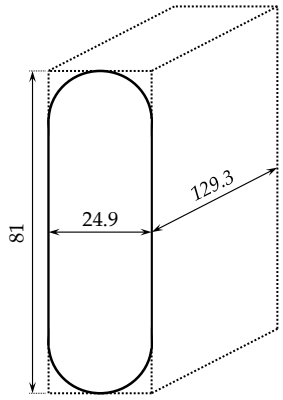

Fig. 3.7: Dimensions of jelly roll substitute.

Name	Material	Thickness	Density	Specific heat	Thermal conductivity	Reference
		µm	$\mathrm{kg\,m^{-3}}$	$\mathrm{J\,kg^{-1}\,K^{-1}}$	$\mathrm{W\,m^{-1}\,K^{-1}}$	
Separator	absorbed	22.8	1073	979.9	0.39	Table 3.3
Anode	Graphite	54.3	2660	1437.4	1.04	[10]
Neg. Conductor	Copper	28.8	8940	386	398	[6]
Anode	Graphite	54.3	2660	1437.4	1.04	[10]
Separator	absorbed	22.8	1073	979.9	0.39	Table 3.3
Cathode	NMC	63.2	1500	1260.2	1.48	[10][5]
Pos. Conductor	Aluminum	28.8	2702	903	237	[6]
Cathode	NMC	63.2	1500	1260.2	1.48	[10][5]
Jelly roll	bulk	338.1	2551	1010.5		
	corrected		2165			
	series circuit				1.1	
	parallel circuit				55.0	

Tab. 3.5: Layer architecture and material properties of the jelly roll.

The current collector is made of the same material as the belonging conductor, meaning the negative one of copper and the positive one of aluminum. The casing consists of aluminum as well. Polycarbonate, a material commonly used for electric insulations, is assumed to be the insulator material, while the socket plates are made of polyethylene. The retainer plates as well as the screws are made of steel. Air data is assumed to be constant. An overview of the remaining material parameters gives table 3.6 and 3.7. As mentioned, the disregarded insulations are taken into account by applying a thermal contact resistance. Insulator thickness $\delta = 0.5\,\mathrm{mm}$ leads to a value $R = \delta/\lambda_{\mathrm{polycarbonate}} = 0.0026\,\mathrm{m^2\,K\,W^{-1}}$.

Name	Material	Density	Specific heat	Thermal conductivity	Reference
		$\mathrm{kg\,m^{-3}}$	$\mathrm{J\,kg^{-1}\,K^{-1}}$	$\mathrm{W\,m^{-1}\,K^{-1}}$	
Neg. current collector	Copper	8940	386	398	[6]
Pos. cur. col., casing	Aluminum	2702	903	237	[6]
Retainer: plates, screws	Steel	7832	434	63.9	[6]
Retainer: socket plates	Polyethylene	950	2000	0.43	[2]
Top insulators	Polycarbonate	1200	1200	0.19	[2]

Tab. 3.6: Material properties of solid regions (exclusive jelly roll).

[5] The actual material in the paper is $LiFePO_4$. Anyway, the values are taken because of a lack of information as stated in the text.

Name	Material	Specific heat	Thermal conductivity	Dynamic viscosity	Molecular weight	Reference
		$\mathrm{J\,kg^{-1}\,K^{-1}}$	$\mathrm{W\,m^{-1}\,K^{-1}}$	$\mu\mathrm{Pa\,s}$	$\mathrm{g\,mol^{-1}}$	
Cavity, environment	Air	1003.6	0.026	18.55	28.97	[6]

Tab. 3.7: Material properties of fluid regions.

3.3.1.2 Boundary Conditions

Thermal boundary conditions are chosen according to experiment SoC50oc. They are explained separately for the air box model and the plain cell model. Distinction between steady state and transient simulations is made as well. Before doing that, heat transfer mechanisms are discussed briefly. In general, these mechanisms can be grouped into three categories:

- Convection
- Radiation
- Conduction

As already stated, conduction has to be taken into account since the massy CTU power cables conduct heat excellently. Whether radiation contributes significantly to heat transfer besides convection can be seen with a simple approximation of heat flows. At first convection is considered. In doing so, *Nußelt number*[6] Nu is calculated in order to determine heat transfer coefficient α. For a vertical wall the (average) Nußelt number is calculated by the formula of *Churchill* and *Chu* [3]:

$$\mathrm{Nu} = \left(0.825 + \frac{0.387\,\mathrm{Ra}^{1/6}}{\left(1 + \left(0.492\,\mathrm{Pr}^{-1}\right)^{9/16}\right)^{8/27}} \right)^2 \tag{3.10}$$

Then heat flow across the lateral surface of cell and retainer A_l is approximated by:

$$\dot{Q}_\mathrm{conv} = \alpha\, A_\mathrm{l}\, (\theta_\mathrm{w} - \theta_\infty) \qquad \text{with:} \qquad \alpha = \frac{Nu\,\lambda}{l_\mathrm{ref}} \tag{3.11}$$

Secondly, radiation heat is expressed by the *Stefan-Boltzmann law*. Therefore cell and retainer are assumed to be gray bodies with emissivity ϵ, exchanging heat with black environment. Then net heat flow to environment across the lateral surface is approximated by:

$$\dot{Q}_\mathrm{rad} = \sigma\,\epsilon\, A_\mathrm{l}\, ({T_\mathrm{w}}^4 - {T_\infty}^4) \tag{3.12}$$

[6] The Nußelt number is a dimensionless quantity correlating convective to conductive heat transfer across a solid-fluid boundary.

Therein denotes σ the *Stefan-Boltzmann constant*. Further absolute temperatures have to be taken. To evaluate heat flows, the same temperature conditions as for determination of the boundary layer thickness are used. Thus, some parameters of the calculations are already presented in table 3.1. Additionally required parameters are listed in table 3.8. This table also includes the obtained results. Heat transfer by radiation is in the order of convective heat transfer and must not be neglected. As only the lateral surface is considered, heat flows do not represent the overall heat dissipation. The approximation refers to maximum load condition (SoC50oc, $i = 4C$, $t = 4\,\mathrm{h}$), so power loss in a range of 0 to 10 W can be expected.

Nußelt number	Nu	$1.83 \cdot 10^{1}$	
Thermal conductivity	λ_∞	$2.57 \cdot 10^{-2}$	$\mathrm{W\,m^{-1}\,K^{-1}}$
Heat transfer coefficient	α	5.21	$\mathrm{W\,m^{-2}\,K^{-1}}$
Stefan-Boltzmann constant	σ	$5.67 \cdot 10^{-8}$	$\mathrm{W\,m^{-2}\,K^{-4}}$
Emissivity (of steel)	ϵ	0.82	
Lateral surface[7]	A_l	$4.09 \cdot 10^{-2}$	$\mathrm{m^2}$
Convective heat flow	$\dot{Q}_\mathrm{conv}$	4.05	W
Radiative heat flow	$\dot{Q}_\mathrm{rad}$	3.97	W

Tab. 3.8: Approximation of convective and radiative heat flow across the lateral surface of cell and retainer. Parameters are set according to condition in table 3.1.

Air Box Model This model represents the experiment realistically since ambient air is included in form of a cell-enclosing, rectangular cuboid. Figure 3.8 shows the geometry of the air box model. In order to obtain a natural convection[8] situation, the box surface is modeled as wall (no-slip condition) with an applied temperature of $\theta_\infty = 19\,^\circ\mathrm{C}$. The constant of gravitation is set to $9.81\,\mathrm{m\,s^{-2}}$. As a result, air rises around the hot cell and falls down along the box wall. To prevent disturbance due to boundary conditions at the wall, the dimensions of the surrounding box are chosen sufficiently large.

Consideration of radiation requires both a radiative transfer model and a radiation spectrum model. Therefore the options *Surface-to-Surface* and *Gray Thermal Radiation* are chosen. The Surface-to-Surface model simulates thermal radiation exchange between surfaces, without consideration of the medium in between the surface pair. Radiation only concerns ambient air[9]. Therefore radiation properties, such as emissivity ϵ, reflectivity ρ, and transmissivity τ, have to be set for the box surface and box interfaces. Opaque solid regions and assumed black environment lead to $\tau = 0$. Using *Kirchhoff's*

[7] $A_\mathrm{l} = 2\,(170 + 2\,(4.6 + 9.55) + 26.5)\,91\,\mathrm{mm^2}$.
[8] See remark on page 31.
[9] Thermal radiation within the cavity is neglected.

law of thermal radiation, only emissivity has to be entered.[10] The Gray Thermal Radiation model assumes that radiation properties are wavelength-independent. As temperature just varies slightly, emissivity is also assumed to be temperature-independent. Table 3.9 gives emissivity values, and therein used area names are identified with cell and retainer in figure 3.9.

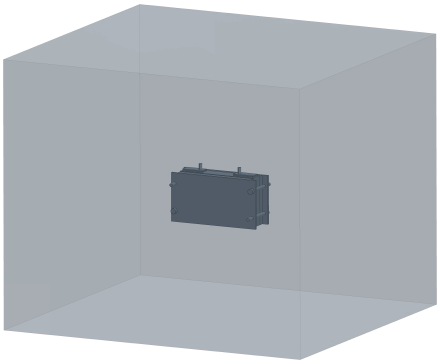

Fig. 3.8: Geometry of the air box model. The box surface is tinted light gray.

Area name	Emissivity	Reference
Plus	0.06	[20]
Minus	0.06	[20]
Aluminum	0.06	[20]
Plastic	0.90	[20]
Steel	0.82	[20]
Steel, inside	0.82	[20]
Box surface	1	

Tab. 3.9: Emissivity values of the air box model. Area names are identified in figure 3.9.

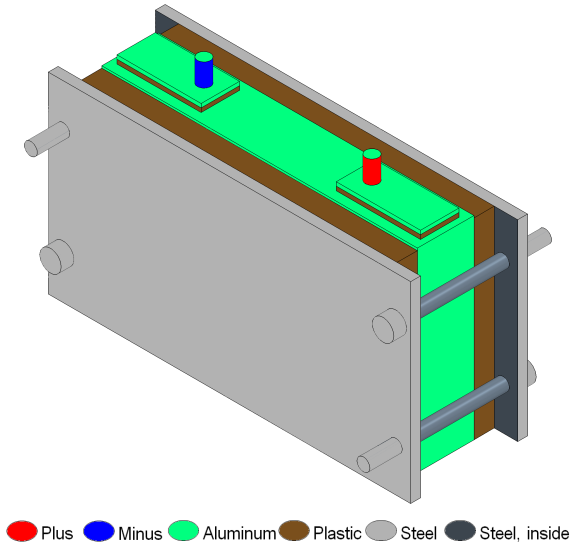

Fig. 3.9: Surface area naming of cell and retainer.

As the CTU cables cross the control volume boundary somewhere, heat flow, or at least temperature, at the intersecting surface should be known for modeling conductive heat transfer. To acquire this information, great technical expenditure is required. However,

[10] If radiation strikes a surface, energy of incident waves is either absorbed (absorptivity α), reflected, or transmitted ($\alpha + \rho + \tau = 1$). Emissivity ϵ is the measure of the surface's ability to emit radiation energy in comparison to a blackbody at the same temperature. Kirchhoff's law: At thermal equilibrium, emitted energy equals absorbed energy ($\alpha = \epsilon$).

measuring such data was not taken into account seriously. A proper analytical approach, considering ohmic heat generation within the cables and heat transfer from cables to environment and to cell, is not applicable because of missing information. The only useful information, obtained by temperature probes *Plus* and *Minus*, are temperatures at the terminals. As a consequence, power cables are replaced by additional boundary conditions. That means thermal effects of the power cables are considered without modeling their actual geometry. The additional boundary conditions are applied at the lateral surface of the terminal bolts, which are marked as *Plus* and *Minus* in figure 3.9. Since the bolts are positioned within the computational domain, *Temperature* boundary conditions are not realizable and temperature data can not be used directly. Instead, the interface option *Enable Energy Source* is activated in order to allow for application of *Heat Flux* interface conditions. Using a negative heat flux value means that the bolt-box-interfaces operate as heat sinks. Heat flux values are received from simulations with the plain cell model, where a direct application of temperature boundary conditions is possible. The values are listed in table 3.11.

Plain Cell Model This model allows low-cost simulations as it only consist of the cell and retainer volume. Conductive and radiative heat transfer are not computed by the code and have to be implemented as boundary condition instead. Therefore, the above approaches of heat transfer coefficient α and of modeling radiation by the Stefan-Boltzmann law are combined to a heat flux boundary condition given as:

$$\dot{q} = -\alpha \left(T - T_\infty\right) - \sigma \epsilon \left(T^4 - {T_\infty}^4\right) \tag{3.13}$$

As T denotes absolute surface temperature, heat flux $\dot{q}$ depends on the position at cell and retainer surface. Ambient temperature is set to $T_\infty = 292.15\,\mathrm{K}$. The heat transfer coefficient α is determined by evaluating the air box model solution. For simplification, the local heat transfer coefficient is averaged over the entire dissipation surface (box interfaces), and the resulting mean value is applied to the entire dissipation surface of the plain cell model (cell/retainer outside surface). Because of symmetry reasons, no radiative heat transfer takes place between opposite faces of the protruding steel plates. Low radiative heat exchange is also expected between opposing faces of screws and cell/socket plates. As a consequence, surface areas indicated as *Steel, inside* in figure 3.9 are excluded from radiative heat transfer. At surface areas *Plus* and *Minus* a temperature boundary condition is made to account for the conductive heat transfer of the CTU power cables. Table 3.10 gives an overview of boundary conditions.

Steady State Simulations Steady state simulations are less time-consuming and less computationally expensive than transient simulations. For this reason they are performed prior to transient runs to obtain a first confirmation of modeling assumptions. Both, the air box model and the plain cell model are used to simulate steady state solutions of cycling loads $i = 4C$ and $i = 3C$. In doing so, only electric current and conditions at the *Plus* and *Minus* surfaces/interface have to be adapted according to experiment. This

Area name	Heat transfer coefficient α	Emissivity ϵ	Temperature	Reference
Plus			see Tab. 3.11	
Minus			see Tab. 3.11	
Aluminum	3.8	0.06		[20]
Plastic	3.8	0.90		[20]
Steel	3.8	0.82		[20]
Steel, inside	3.8	0		

Tab. 3.10: Thermal boundary conditions of plain cell model. Area names are identified in figure 3.9. $[\alpha] = \mathrm{W\,m^{-2}\,K^{-1}}$, $[\epsilon] = 1$.

is done as an iterative process. In a first attempt, the air box model is simulated with disregarded heat sinks. This gives a good approximation of the heat transfer coefficient α. Subsequently α and the measured terminal temperatures are applied to the plain cell model. Because of different positioning of boundary conditions and temperature probes (terminal bolts $\Leftrightarrow$ terminal plates), the temperatures have to be adjusted slightly. In doing so, temperatures are decreased until the temperatures obtained at terminal plates[11] match measured experimental data. Finally, heat sink values are determined by evaluating heat flow across Plus/Minus surface areas. The heat sink values are now applied to the air box model, starting the iterative process again. The whole procedure is done easily by running the air box and plain cell models simultaneously and by updating boundary conditions during the simulations. The obtained parameters are listed in table 3.11.

Area name	Air box model		Plain cell model	
	Heat flux $\mathrm{W\,m^{-2}}$		Temperature °C	
	4C	3C	4C	3C
Plus	-503	-438	$37.3 - 0.3$	$30.4 - 0.2$
Minus	-2076	-1202	$36.9 - 0.5$	$30.2 - 0.4$

Tab. 3.11: Interface/boundary conditions of surface areas *Plus/Minus* in steady state simulations. Temperatures are expressed as *measured value minus adjustment*.[12]

[11] Therefore *point probes* are defined in the CFD model, which take samples of data at specific points. The point probes have the same positions as the real probes in the experimental setup, meaning they serve as virtual temperature probes.

[12] The adjustment and heat flux values of Plus and Minus surface areas are different as the underlying current collectors are made of aluminum and copper, respectively.

Transient Simulations In order to save computational costs, only the plain cell model is utilized to virtually rerun the experiment. Therefore electric load and temperature boundary conditions at the Plus/Minus surface areas have to be specified as a function of time. In contrast to the above, manual temperature adjustments are not practicable. Instead, measured temperatures are applied in a first simulation run and corrected values are calculated by comparison of CFD results with experimental data. These corrected values are applied in a second simulation run. Results of the second run are presented later. Figure 3.10 shows the time course of temperatures.

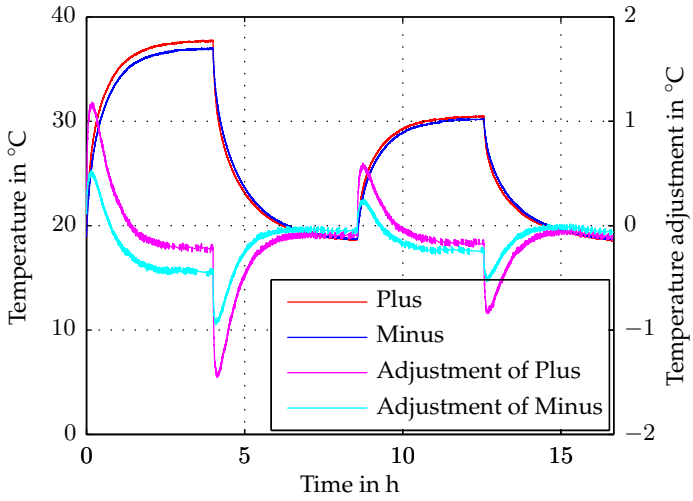

Fig. 3.10: Temperature boundary conditions of surface areas *Plus/Minus* in transient simulations. A first run is performed applying Plus/Minus (measured temperatures), whereas final results are found using *Plus/Minus + adjustment of Plus/Minus*.

Remark: *Air box model and importance of natural convection*: Using a closed box volume gives the simplest approach of modeling the convection phenomena. In a forced convection situation either an open volume or the entire temperature chamber would have to be modeled. This requires either defining of inlet/outlet boundary conditions or specification of fans. In other words, information about the velocity field must be known. Thus, higher standards of experimental setup and of measurement equipment are required, which would increase the cost of the experiment. Apart from that, the size of CFD model would increase considerably as well.

3.3.2 Electric Model

Modeling electrical effects is more abstract. The bulk material does not enable a characterization of electrochemical processes and of real fields of electric potential and electric current. In reality, the current flow between the electrodes is assumed to be perpendicular to the electrodes as the intermediate distance is small [13]. The majority of power loss is generated in this region as internal resistance arises mostly from electrolyte. Within the conductors electric current density is parallel to the foil surface. The current density increases toward the current collectors as electric charge is always conserved. While current flow in the conductors can not be described, the orientation of current density between the electrodes is represented passably by the model. Thus, use of the model is permitted. In fact, the model solves the electric potential equation derived as [7]:

$$-\nabla\sigma\nabla\Phi = 0 \tag{3.14}$$

Where σ is the *electrical conductivity* and Φ is the electric potential. The code allows treating σ as scalar quantity representing a linear, isotropic material. Using the local formulation of *Ohm's law*, current density $\vec{J}$ is expressed as:

$$\vec{J} = \sigma\,\vec{E} \qquad \text{with:} \qquad \vec{E} = -\nabla\Phi \tag{3.15}$$

Therein denotes $\vec{E}$ the electric field. Then density of dissipated power is given by:

$$p = \vec{J}\cdot\vec{E} \tag{3.16}$$

As stated, density of dissipated power gives a source term in the energy equation. In contrast to thermal material parameters, electrical conductivity can not be determined analytically and therefrom it is calculated from experimental results. Therefore the jelly roll substitute is virtually unwrapped and simplified as flat, block-shaped conductor such as suggested in figure 3.11. Using block height l and top surface area A, electric

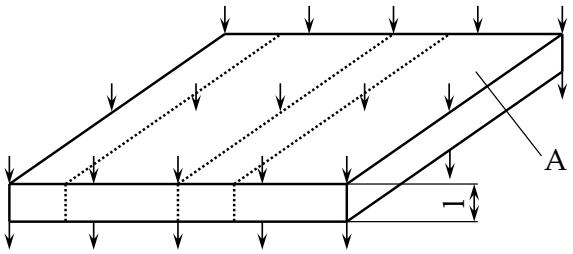

Fig. 3.11: Schematic of unwrapped jelly roll substitute and current flux.

conductance of the block is described as:

$$G = \sigma\,\frac{A}{l} \tag{3.17}$$

Inserting electric conductance into Joule's law, electrical conductivity of the bulk material is obtained:

$$\sigma = \frac{i^2\,l}{P\,A} \tag{3.18}$$

The variable P denotes the (temperature-dependent) total power loss of the cell and i the electric load. Because of a temperature gradient, electrical conductivity is variable within the bulk material.[13] According to the equivalent circuit diagram in figure 2.1, the cell's global electric behavior is described by one ohmic resistor $R_\mathrm{i} = 1/G$ ($R_\mathrm{a} = C_\mathrm{a} = 0$). It follows that the electric model does not reproduce any charge storage capability and any electrical dynamics.

3.3.2.1 Parameter

Electrical conductivity is the only required parameter. The block dimensions[14] are defined by the jelly roll substitute's geometry, while power loss and electric load are received from experimental data. The calculation of power loss from terminal voltage v and terminal current i is explained in the following paragraph.

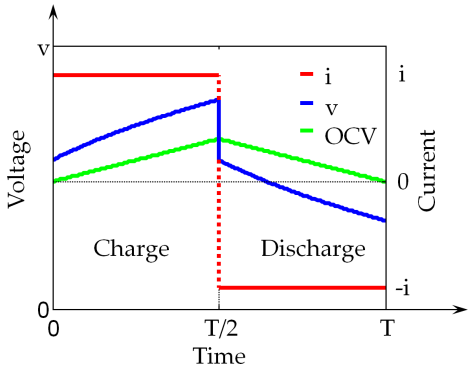

Fig. 3.12: Sketch of terminal voltage due to an applied current profile. Assuming $OCV \propto SoC$ leads to a linear change of OCV.

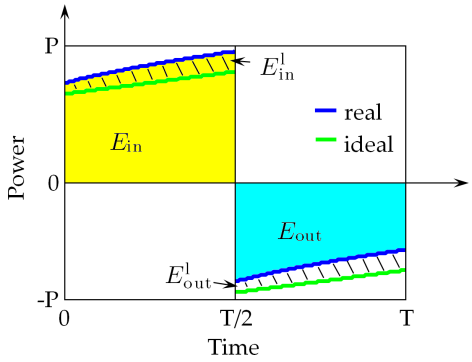

Fig. 3.13: Power input/output for a real and an ideal cell with regard to figure 3.12. The filled areas represent transferred energy, and lost energy is marked by hatched areas.

Figure 3.12 illustrates terminal values i, v for a single cycle period. As charged capacity equals discharged capacity ($T/2\,(i - i) = 0$), SoC of start and end point are the same ($SoC(0) = SoC(T)$[15]). For drawing a proportional correlation of OCV and SoC is assumed, that is why OCV follows a linear function of time. Cell impedance cause a difference between *real* terminal voltage v and (imaginary) *ideal* terminal voltage OCV. It follows that power input (charging) is higher and power output (discharging) is lower than for an ideal cell, as presented in figure 3.13. The area under the curve gives transferred energy, for an ideal cell energy input equals energy output:

$$E^\mathrm{i}_\mathrm{in} = \int_0^{T/2} OCV(t)\, i(t)\, \mathrm{d}t = -\int_{T/2}^{T} OCV(t)\, i(t)\, \mathrm{d}t = -E^\mathrm{i}_\mathrm{out} \tag{3.19}$$

[13] Otherwise it would be eliminated from the electric potential equation (3.14).
[14] $A = 2\,(24.9 + 55.6)\,129.3\,\mathrm{mm}^2$, $l = 12.2\,\mathrm{mm}$. (The center body is 0.5 mm thick.)
[15] This is a prerequisite for applying the method.

Then truly transferred energy can be expressed as sum of ideal energy transfer and energy losses:

$$E_{\text{in}} = E_{\text{in}}^{\text{i}} + E_{\text{in}}^{\text{l}} \qquad (E_{\text{in}}^{\text{i}} > 0,\ E_{\text{in}}^{\text{l}} > 0) \tag{3.20}$$

$$E_{\text{out}} = E_{\text{out}}^{\text{i}} + E_{\text{out}}^{\text{l}} \qquad (E_{\text{out}}^{\text{i}} < 0,\ E_{\text{out}}^{\text{l}} > 0) \tag{3.21}$$

Using equations (3.19, 3.20, 3.21), average power loss per cycle is given:

$$\bar{P}_T^{\text{l}} = \frac{E_{\text{in}}^{\text{l}} + E_{\text{out}}^{\text{l}}}{T} = \frac{E_{\text{in}} + E_{\text{out}}}{T} = \frac{1}{T}\int_0^T v(t)\, i(t)\, \mathrm{d}t \tag{3.22}$$

That means instead instantaneous power loss a time series of average power loss values is calculated. In doing so, a Matlab script is used to detect start and end of cycles from a given continuous measurement signal and evaluates equation (3.22). The obtained period of $T = 20\,\text{s}$ is very acceptable considering the time scale of the entire system. This can be seen from figure 3.14, where input variables for determination of electrical conductivity are plotted.

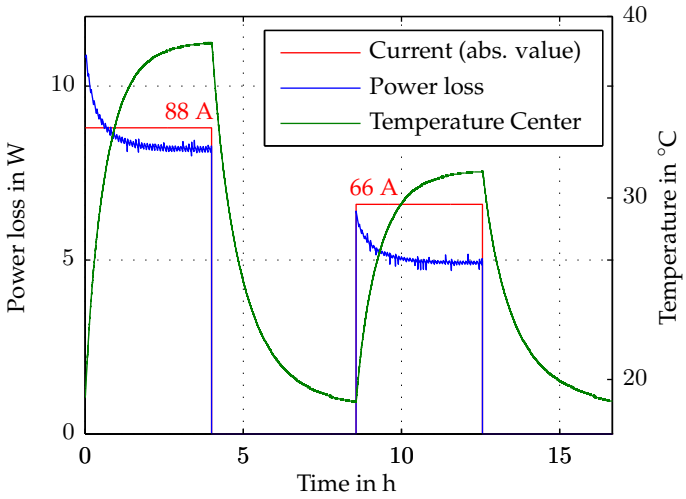

Fig. 3.14: Quantities for determination of electrical conductivity, obtained from experiment SoC50oc.

The calculation of electrical conductivity requires a load sequence matching the periods of power loss. For this reason a load profile is created manually which contains constant values according to table 2.1 instead measurement data. This idealized load also minimizes an introduction of noise. As the load is raised to the power of two, no distinction between charging and discharging must be drawn. In combination with temperature a parametric description of the temperature-dependent electrical conductivity is found by using time as free variable. It is obvious that a jelly-roll-averaged temperature should be used to realize the modeling idea correctly. As discussed later on, the resulting temperature field shows only small variations, and therefore temperature values of probe Center approximate the average temperature well. Star-CCM+ allows electrical conductivity

to be specified as a constant or a (field) function, therefrom a curve is generated using Matlab's *Curve Fitting Toolbox*. Applying a power series preserves predictive capability beyond parametrization bounds and results in a rather simple formula. While one fitting σ_{50} bases on the data of the SoC50oc experiment only, a further fitting σ_{all} is made including data from all experiments. Figure 3.15 compares electrical conductivity data and curve fittings. Fitting σ_{50} is used for simulations with the plain cell model as well as the air box model. Both curves are given as follows:

$$\sigma_{50} = (-1.210\,139\,855\,209\,077 \cdot 10^{14}\, T^{-4.612\,168\,491\,174\,701} + 936.6)\,\mathrm{S\,m^{-1}} \tag{3.23}$$

$$\sigma_{\text{all}} = (-3.252\,913\,493\,290\,552 \cdot 10^{13}\, T^{-4.383\,111\,127\,726\,723} + 940.5)\,\mathrm{S\,m^{-1}} \tag{3.24}$$

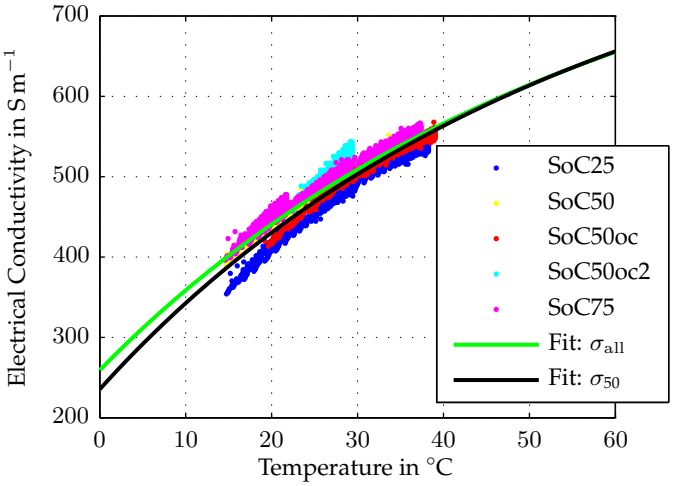

Fig. 3.15: Point clouds and curve fittings of electrical conductivity.

3.3.2.2 Boundary conditions

The above remarks imply that the electric model is only assigned to the jelly roll. For boundary conditions either the electric potential or the current flux can be applied. To be more precise, current flux means the normal electric current $J_{\text{n}} = \vec{J} \cdot \vec{n}$ on boundaries with face normal vector $\vec{n}$, also referred to as *specific electric current*. Referring to figure 3.11, the flux value is defined easily as:

$$J_{\text{n}} = \frac{i}{A} \tag{3.25}$$

The specific electric current boundary condition is applied with negative/positive sign to opposite surfaces of the jelly roll segments. These are denoted as inlet/outlet surfaces in the following. To ensure conservation of electric charge, flux values are determined

with discretized inlet/outlet surface areas. Figure 3.16 shows the location of inlet/outlet surfaces and illustrates the arrangement of jelly roll segments. The jelly roll is segmented to depict the orientation of electric current density as discussed in section 3.6.1. Just as thermal boundary conditions (energy equation), electric potential or current flux can not be specified within a domain, and that is why segments have to be electrically separated. Therefore a *Center body*[16] – excluded from the electric model – is introduced.

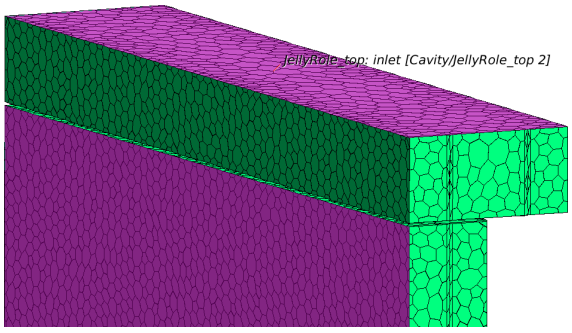

Fig. 3.16: Location of electrical boundary conditions shown for two of the four jelly roll segments. Inlet surfaces are colored purple. Outlet surfaces are positioned vis-a-vis to inlet surfaces (not visible).

As mentioned, the electric model primarily describes power loss and for this reason applying the effective (root mean square) load is sufficient. This fact allows computing the thermal steady state by running a steady state simulation. Furthermore, the load must not be temporally resolved in transient simulations. Since the square wave's (equation (2.4)) root mean square is equal to its amplitude, the current profile for transient simulation results in a step function as given in table 3.12. To exactly hit the time points of the jumps, the time steps before each discontinuity is accordingly shortened.

Type of simulation	Load i	Time
	A	s
Steady state	$4C$	
Steady state	$3C$	
Transient	$4C$	0–14 400
	0	14 401–30 826
	$3C$	30 827–45 227
	0	45 228–61 727

Tab. 3.12: Electrical boundary conditions. Specific electric current is defined by equation (3.25).

[16] Figure 3.3 shows the I-shaped Center body.

3.4 Results of Steady State Simulations

To summarize the above explanations, the experiment SoC50oc is simulated with CFD models by applying electric current as well as adequate thermal boundary conditions representing the power cables. Thus, steady state results should correspond to measurement values under thermally steady conditions. Table 3.13 summarizes the obtained results, in which experimental data is taken at the end of each cycling period ($t \approx 4\,\mathrm{h}$ and $t \approx 12.6\,\mathrm{h}$). Values are documented with a precision of two digits in order to identify differences in results, although such high accuracy does not have any engineering relevance.

Name	$i = 4C$				$i = 3C$			
	P	ΔP	θ_c	$\Delta\theta_c$	P	ΔP	θ_c	$\Delta\theta_c$
Experiment	8.22		38.56		4.93		31.50	
Air box model	8.11	−1.3 %	38.69	0.3 %	4.95	0.4 %	31.59	0.3 %
Plain cell model	8.12	−1.2 %	38.59	0.1 %	4.98	1.0 %	31.08	−1.3 %

Tab. 3.13: Comparison of experimental and numerical steady-state results of power loss P and temperature of probe Center θ_c. $[P] = \mathrm{W}$, $[\theta_c] = {}^\circ\mathrm{C}$.

As power loss error and temperature error are less than 1.3 %, a very good agreement between simulations and experiment is obtained. Evaluating the average jelly roll temperature of the air box models result in $\theta_{jr}^{4C} = 39.27\,^\circ\mathrm{C}$ and $\theta_{jr}^{3C} = 31.95\,^\circ\mathrm{C}$, which are higher than the values obtained with probe Center. From that it follows that parameterizing electrical conductivity with center-temperature shifts the fitted curve to lower temperatures (to the left in figure 3.15), and consequently power loss is underestimated. Since deviation of average and center-temperature lessens with lower currents, the underestimation of power loss decreases when reducing the load. On the other hand, the air box model overestimates power loss in case $i = 3C$. Because of the coupled, nonlinear nature of the problem, a simple reason for this behavior can not be identified. Evaluating the average heat transfer coefficient gives values $\alpha^{4C} = 3.8\,\mathrm{W\,m^{-2}\,K^{-1}}$ and $\alpha^{3C} = 3.4\,\mathrm{W\,m^{-2}\,K^{-1}}$. As the first value is used for the plain cell model, it is obvious that center-temperature is underpredicted in case $i = 3C$.

Figures 3.17 and 3.18 compare casing temperatures obtained with the air box model and the plain cell model. Therefore the color bars are set to an equal value range to have comparable illustrations. The temperature gradients coincide largely and a temperature spread of just 1 °C is noticeable. The approach of averaging heat transfer coefficient gives excellent results, only at the top face a slight deviation can be found. In this region convective heat transfer is overestimated, as proved by figure 3.19. There (convective) heat transfer coefficient, inherently computed by the air box model, is shown. At the side face values in the order of $\alpha \approx 5\,\mathrm{W\,m^{-2}\,K^{-1}}$ are found, verifying the estimation which is made in table 3.8.

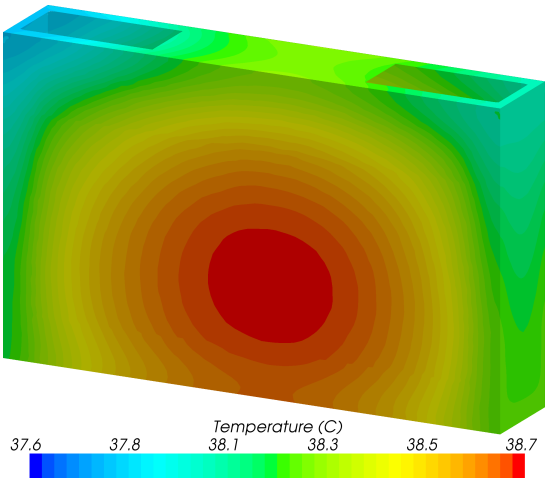

Fig. 3.17: Casing temperature, air box model, $i = 4C$.

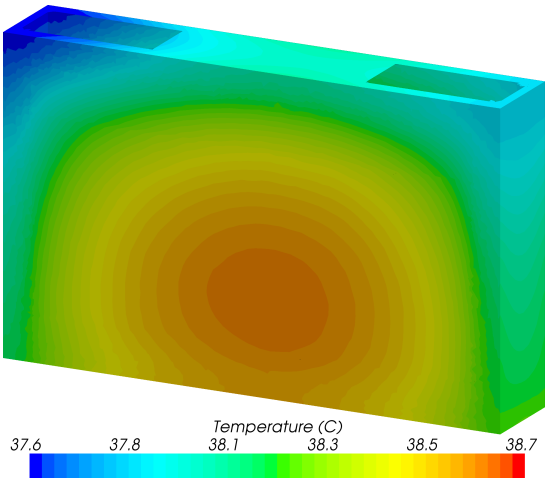

Fig. 3.18: Casing temperature, plain cell model, $i = 4C$.

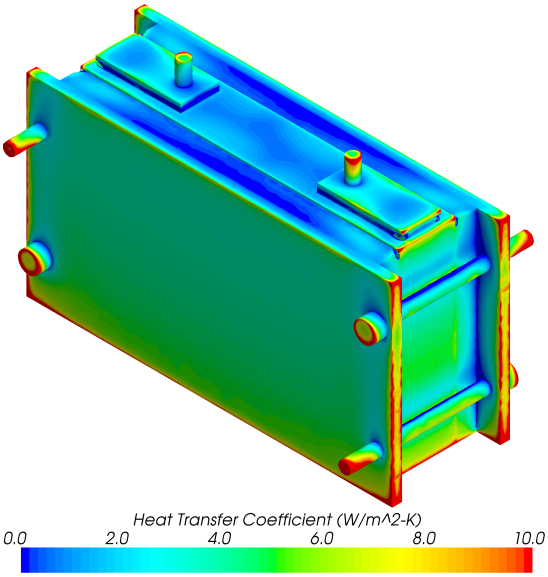

Fig. 3.19: Heat transfer coefficient ($\theta_\infty = 19\,^\circ\text{C}$), air box model, $i = 4C$.

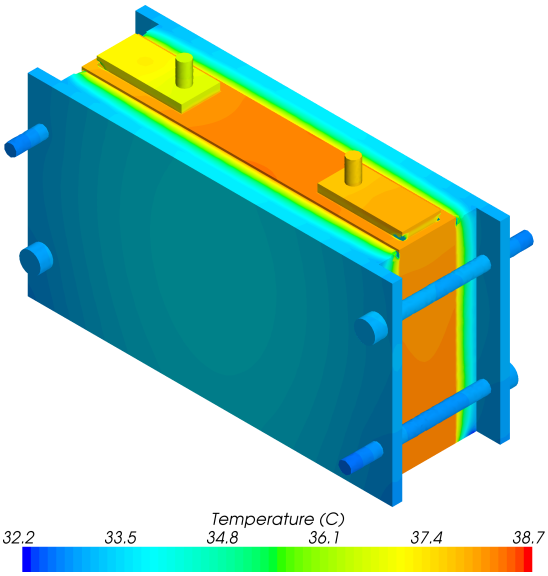

Fig. 3.20: Surface temperature, air box model, $i = 4C$.

Figure 3.20 illustrates surface temperature of the whole cell package. As the casing temperature is clearly higher than the temperature of the steel plate, the socket plates thermally isolate the cell. This fact can also be seen in figure 3.21, which shows temperature at a transverse section through the cell center. While temperature decreases only 1 °C between jelly roll center and casing (probe Center), a temperature drop throughout the socket plates of about 4.6 °C is found. Within the steel plates the temperature profile is rather smooth. The circular temperature profile in the bottom region is effected by the anisotropic formulation of thermal conductivity, whereas the effect is mitigated through adjacent air (cavity) in the top region. Another consequence of the anisotropy is a low temperature spread in longitudinal direction, as figure 3.22 points out. A temperature difference between the terminals can be seen there, as well.

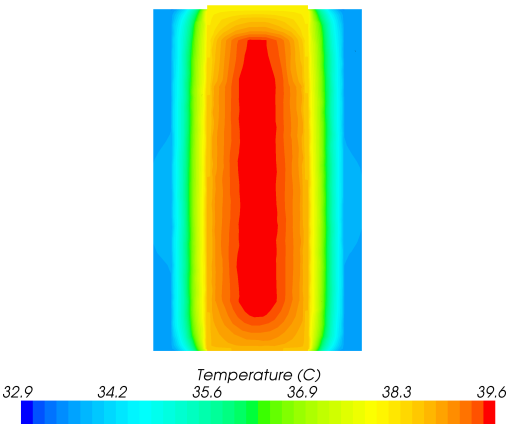

Fig. 3.21: Temperature, transverse section through cell center, plain cell model, $i = 4C$.

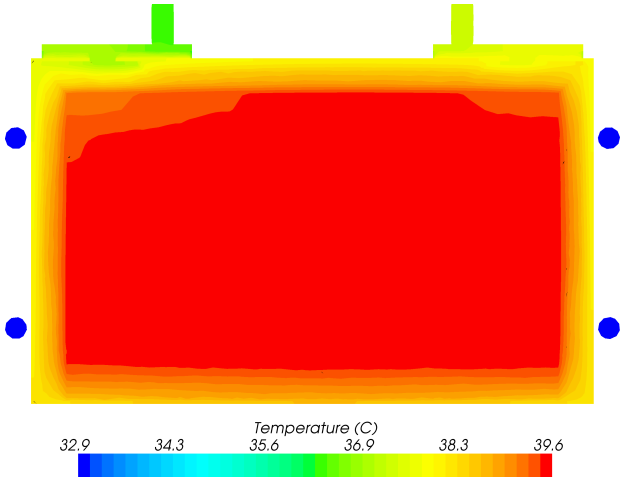

Fig. 3.22: Temperature, longitudinal section through cell center, plain cell model, $i = 4C$.

Figure 3.23 depicts the flow field in vicinity of the cell, represented by streamlines. Flow detaches at the top edge of the steel plates and a zone having almost zero velocity (quasi dead water) develops above the cell, which causes low convective heat transfer at the top face. As mentioned, a simulation using a turbulence model is performed for comparison. The y^+-value denotes a non-dimensional distance from wall to adjacent cell center and is used to describe flow quantities of the boundary layer. A value of $y^+ < 1$ is recommended [7] for resolving the viscous sublayer, which is a fulfilled requirement as presented by the figure. From this it follows that the mesh is also fine enough to accurately compute the boundary layer with a laminar flow model. Although the flow regime is laminar by nature and therefore a laminar description is sufficient, power loss and center-temperature obtained with use of the turbulence model are practically equal. Finally, figures 3.24 and 3.25 show the magnitude of air velocity within the cavity at transverse and longitudinal sections. As expected, resulting flow velocities are at very low level, indicating that convective heat transfer is of minor importance inside the cell.

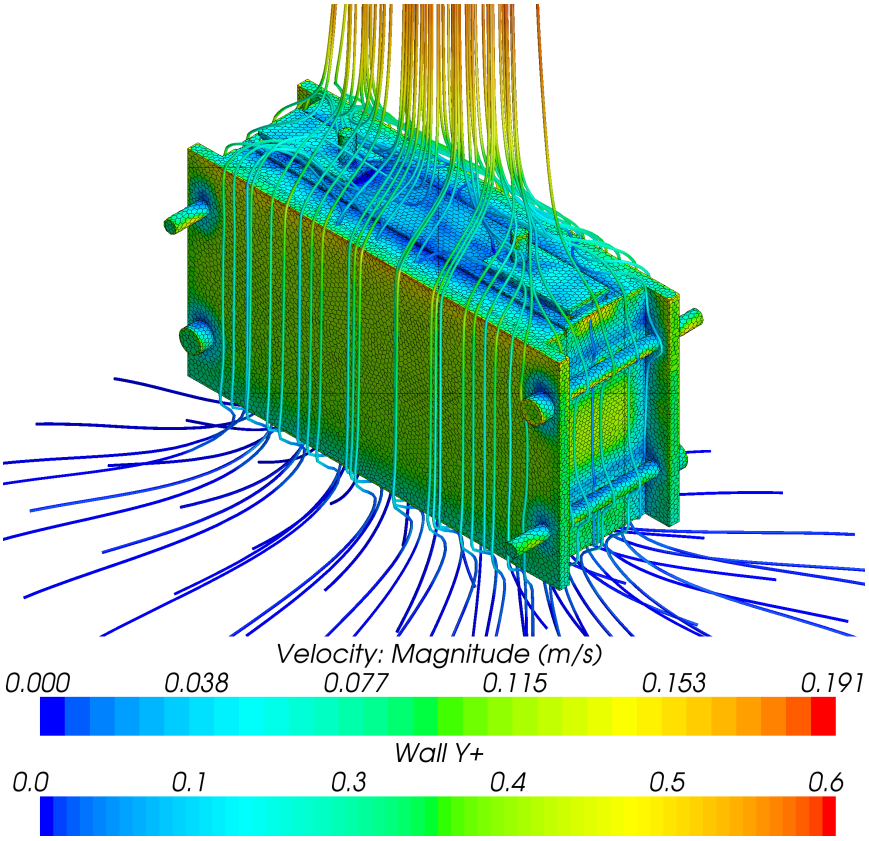

Fig. 3.23: Streamlines and dimensionless wall distance y^+, air box model (using k-ϵ turbulence), $i = 4C$.

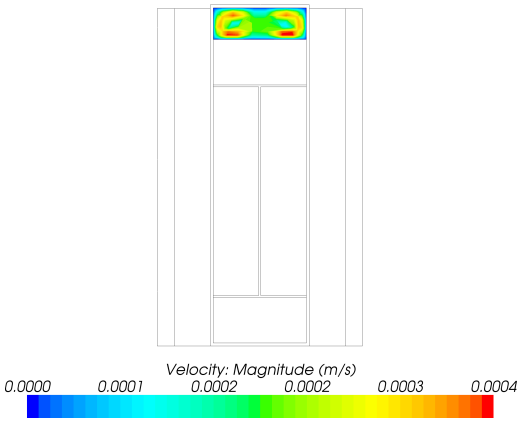

Fig. 3.24: Velocity magnitude within the cavity, transverse section through cell center, plain cell model, $i = 4C$.

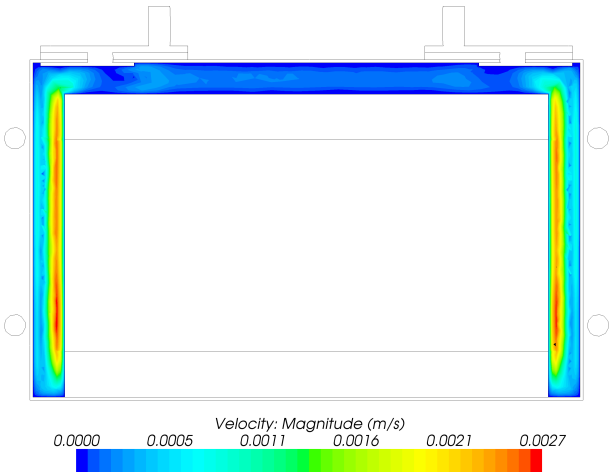

Fig. 3.25: Velocity magnitude within the cavity, longitudinal section through cell center, plain cell model, $i = 4C$.

3.5 Results of Transient Simulations

The good agreement of steady state results of both, the plain cell and the air box models, motivates to perform a transient analysis with the plain cell model. Figure 3.26 compares power loss and center-temperature of the experiment with simulation results. The plot

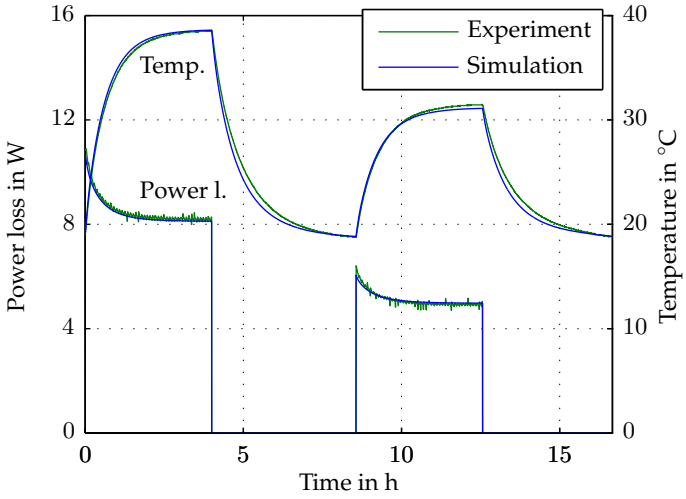

Fig. 3.26: Comparison of power loss and temperature of probe Center of experiment with simulation.

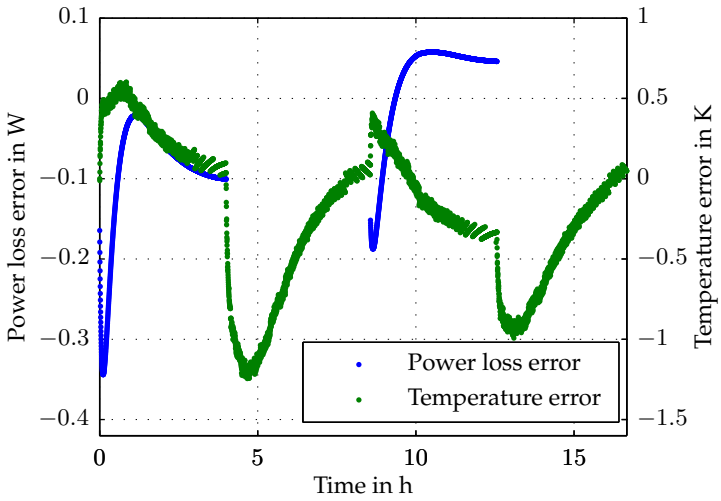

Fig. 3.27: Power loss error and temperature error of the transient simulation.

generally confirms findings of the previous section 3.4. Power loss has a negative deviation during the first cycling period as it is slightly underestimated. During the second cycling period this effect is overcompensated by an under-prediction temperature. Using a constant heat transfer coefficient represents a strongly simplified approach, because

heat transfer depends inherently on temperature. Since temperature is overpredicted during heating-up and undervalued during cooling-down, it is assumed that heat capacity of the cell is assessed too low. But power loss error and temperature error remain within very acceptable limits as illustrated in figure 3.27.

Finally, figure 3.28 opposes introduced waste heat (power loss) and dissipated heat, in which the contribution of the individual heat transfer mechanisms is presented separately. Because of the poor capability of natural convection to transfer heat, radiation plays a significant role. Its percentage of heat dissipation is about 45 % at steady state, even though temperature is rather low. Conduction within the power cables contributes about 6 %. An interesting aspect is that heat is fed into the cell during the first hour of cycling. This is presumably caused by a temperature dependence of the cables' internal resistance. The sudden absence of ohmic heat generated within the cables probably cause the humps at beginning of the cooling-down periods.

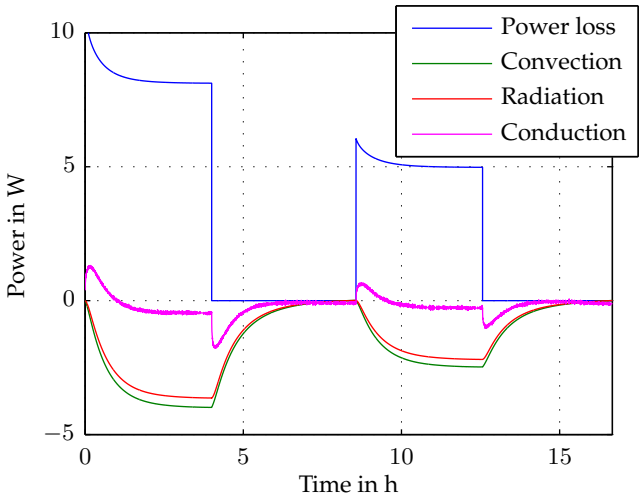

Fig. 3.28: Power loss and heat dissipation of individual heat transfer mechanisms.

All together, results show very good agreement with the experiment and confirm validity of the developed CFD model.

3.6 Discussion of Several Modeling Aspects

3.6.1 Segmentation of the Jelly Roll Substitute

A hot spot within the jelly roll increases current density and consequently locally introduced waste heat. For this reason a realistic simulation of current density is desired. As mentioned, charge flow perpendicular to layers is of particular interest. Considering the areal extent of the unwrapped jelly roll and the unwrapped jelly roll substitute,

the current density magnitude can obviously not be represented. To obtain suitable surfaces for application of electric boundary conditions, the jelly roll substitute has to be segmented. At first, splitting the domain into trapezoidal prisms as illustrated in figure 3.29 is chosen. In doing so, the red and blue lines represent inlet and outlet surfaces. This approach geometrically interprets the wound layer configuration very well, but gives unrealistic peaks of current density. Although disregarding temperature dependence of electrical conductivity, magnitudes covering a range of about 3800 $\mathrm{A\,m^{-2}}$ are found. Also, a modification of boundary conditions (shape functions or using a charge sink (center body) instead of a outlet condition) does not lead to satisfactory results. As the outlet surface is much smaller than the inlet surface, current density has to rise close to the outlet surface. This fact contradicts reality, where current density is homogeneous within certain bounds. A finer splitting of the jelly roll substitute would give an unwanted increase of model complexity. However, the already known segmentation into rectangular prisms is used. As depicted in figure 3.30, this approach

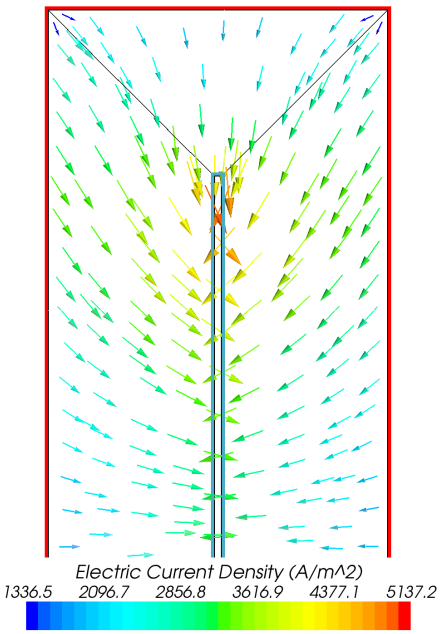

Fig. 3.29: Current density for trapezoidal segmentation, $\sigma = 550.6\,\mathrm{S\,m^{-1}}$, $i = 2C$.

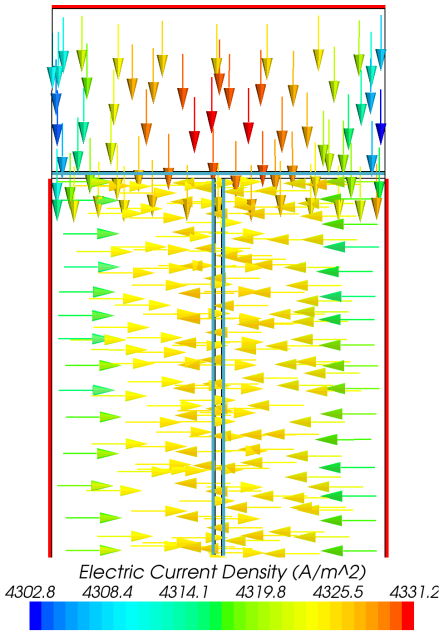

Fig. 3.30: Current density for rectangular segmentation, $\sigma(T) = (6.753\,T - 1485)\,\mathrm{S\,m^{-1}}$, $i = 2C$.[17]

gives a relatively homogeneous distribution of current density (value range of about 30 $\mathrm{A\,m^{-2}}$, already including a temperature dependence). Moreover, an even distribution is forced at inlet/outlet surfaces because of the applied boundary conditions. This cross-sectional shape also facilitates modeling of thermal conductivity considerably, as the formulation of anisotropy can be altered for each segment (*region-wise*). The approach simulates current flow within the jelly roll, other conducting parts as current collectors or terminals are only considered with respect to power loss.

[17] The linear electrical conductivity function was made in an early development stage of the model.

3.6.2 Absence of the Air Gap

The jelly roll is produced by winding up a planar electrode configuration and gets therefore its roundly shaped top and bottom end. As a consequence, space remains free between the round jelly roll ends and the casing. This air-filled gap is not modeled, instead the jelly roll substitute is contacting the casing wall physically. Hence, the real behavior in heat transfer is not correctly modeled. To investigate the influence of this inaccuracy, a series of simulations is computed where the gap is implemented by a thermal contact resistance. This means only conductive heat transfer is considered. Referring to figures 3.24 and 3.25, air is assumed to be quiescent for all practical purposes, allowing the disregard of convective transfer. Radiation is neglected as well. The contact resistance is applied to interfaces as shown in figure 3.33 and is determined for z and y-direction:

$$R_{\mathrm{z|y}} = \frac{z_{\mathrm{a}}|y_{\mathrm{a}}}{\lambda_{\mathrm{air}}} \tag{3.26}$$

Using the coordinates illustrated in figures 3.31 and 3.32, components of the gap width are expressed:

$$y_{\mathrm{a}}(z) = r - r\cos\Bigg(\underbrace{\frac{\pi}{2} - \arccos\left(\frac{|z|}{r}\right)}_{\phi}\Bigg) \tag{3.27}$$

$$z_{\mathrm{a}}(y) = r - r\sin\Bigg(\underbrace{\arccos\left(\frac{|y_0 - y|}{r}\right)}_{\psi}\Bigg) \tag{3.28}$$

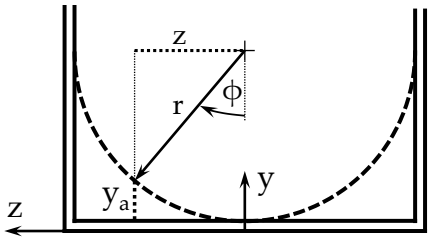

Fig. 3.31: Air gap width y_{a}.

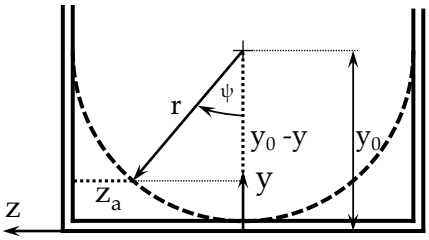

Fig. 3.32: Air gap width z_{a}.

Therein a coordinate system equivalent to that of the CFD model is used, thus equations (3.26) can be directly applied as *field function*[18]. As Star-CCM+ has numerical problems to evaluate R_{z} for $\psi \to 0$, term $\arccos(\ldots)$ of equation (3.28) is replaced with its Taylor series of order thirteen. This approximation results in $z_{\mathrm{a}}(\psi = 0) = 9.8\,\mathrm{mm} \neq 12.45\,\mathrm{mm}$, meaning that the jelly roll figuratively touches the casing at a width of 5.3 mm. For the sake of consistency, the thermal contact resistance R_{y} is also set to zero in the

[18] $r = 12.45\,\mathrm{mm}$, $y_0 = 13.25\,\mathrm{mm}$ or $y_0 = 69.35\,\mathrm{mm}$.

area of contact ($R_y(|z| < 2.65\,\mathrm{mm}) = 0$). As a result, resistance values up to $0.5\,\mathrm{m^2\,K\,W^{-1}}$ are obtained. For investigating the air gap influence, two models are used:

I Cell including socket plates and retainer

II Single cell

Model I is quite similar to the plain cell model but conductive and radiative heat transfer are disregarded. At the whole surface a convection boundary condition is applied using $\alpha = 10.9\,\mathrm{W\,m^{-2}\,K^{-1}}$ and $\theta_\infty = 24\,^\circ\mathrm{C}$. It is expected that the air gap has most impact in situations where heat has to be transmitted through the cell bottom, for example a cooling system via bottom plate. This situation is represented by model II. The casing's bottom surface is kept on a constant temperature of 24 °C, the casing's side walls are set adiabatic and the remaining surfaces are constrained by a convection boundary condition using $\alpha = 5\,\mathrm{W\,m^{-2}\,K^{-1}}$ and $\theta_\infty = 24\,^\circ\mathrm{C}$. The particular surfaces are highlighted in figure 3.34. Both model I and model II are loaded with a current of $i = 4C$ and use a linear[19] electrical conductivity curve defined as $\sigma(T) = (6.753\,T - 1485)\,\mathrm{S\,m^{-1}}$. The investigation is made by performing steady state simulations and varying the contact resistance. Then heat flow through the gap (interfaces side and bottom, compare figure 3.33) and the casing bottom (surface outside, compare figure 3.33) is analyzed. In other words, the heat flow from jelly roll into casing and from casing into environment is analyzed in specific areas. Furthermore, power loss and center-temperature are evaluated. Table 3.14 lists key parameters of the models and the obtained results.

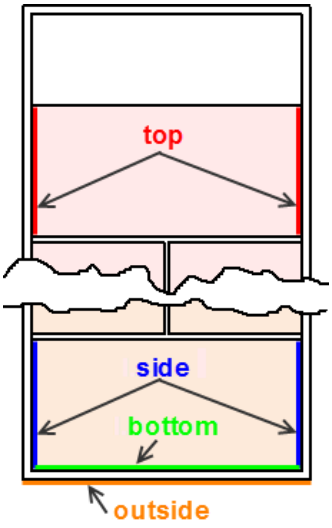

Fig. 3.33: Naming of interfaces (top, side, bottom) and of casing bottom surface (outside) as used in the air gap investigation.

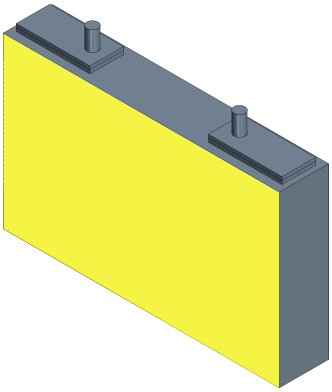

Fig. 3.34: Boundary conditions of model II: adiabatic (yellow), convection (gray) and temperature (non-visible bottom surface).

[19] See footnote 17 on page 43.

	Position	Model **I**		Model **II**			
		a	**b**	**a**	**b**	**c**	**d**
Th. c. res. $\mathrm{m^2\,K\,W^{-1}}$	top	0	R_z	0	R_z	0	0
	side	0	R_z	0	R_z	0	10
	bottom	0	R_y	0	R_y	10	10
H. flow W	side	0.62	0.16	1.24	0.36	2.32	$1.34 \cdot 10^{-3}$
	bottom	0.65	0.48	1.51	0.99	$7.19 \cdot 10^{-4}$	$1.89 \cdot 10^{-3}$
	outside	0.75	0.75	8.61	8.51	8.56	8.42
T: °C	Center	41.98	42.02	27.02	27.42	27.26	27.90
P: W	Jelly roll	7.34	7.32	8.72	8.64	8.68	8.57

Tab. 3.14: Interface conditions (thermal contact resistance) and results (heat flow, temperature, power loss) of the air gap investigation. $R_{z|y}$ by (3.26).

The results of model I demonstrate that introducing an air gap just marginally impacts power loss and center-temperature. Although heat flows through the interfaces side and bottom are significantly decreased ($-74\,\%$, $-26\,\%$) by introducing the air gap, heat dissipation remains constant at the casing bottom. A similar behavior is found in cases IIa and IIb, but small changes of center-temperature ($\Delta\theta_c = 1.5\,\%$) and power loss ($\Delta P = -0.9\,\%$) are recognized. Changes of interface heat flows are similar to those of model I ($-71\,\%$, $-34\,\%$), but almost the entire heat is dissipated at the bottom surface. The conclusion is that modeling the air gap between jelly role and casing is of minor importance and can be omitted. As the jelly roll has already very low thermal conductivity perpendicular to layers, an additional thermal resistance does not affect heat transfer essentially. Because of the excellent thermal conductivity of the casing material, most of the heat is transmitted within the thin casing. Case IIc and case IId are simulated to assess this fact, in which the jelly roll is thermally isolated by a thermal resistance of $10\,\mathrm{m^2\,K\,W^{-1}}$. These cases do not represent any real situation.

Finally, the temperature field inside the cell is discussed using results of model II. In figure 3.35a the air gap is neglected. The anisotropy of thermal conductivity effects the circular temperature profile in the bottom region. Since heat dissipation mainly occurs at the bottom surface, a temperature gradient develops from bottom to top region, and further a hot spot in the top region. In figure 3.35b, significant temperature jumps between casing and jelly roll indicate the presence of air gaps. The air gaps also cause the extension of the hot spot area over the entire jelly roll width. Furthermore, a declining temperature is found in vicinity of the contact area of jelly roll and casing ($|z| < 2.65\,\mathrm{mm}$, $y = 0.8\,\mathrm{mm}$). The temperature field for an isolated jelly roll bottom (figure 3.35c) matches, with exception of the sharp formed temperature jump, widely the results of case IIa (figure 3.35a). Isolation of side and bottom interface (figure 3.35d) leads to a hot area located at the bottom. This case demonstrates the excellent heat conduction within the casing.

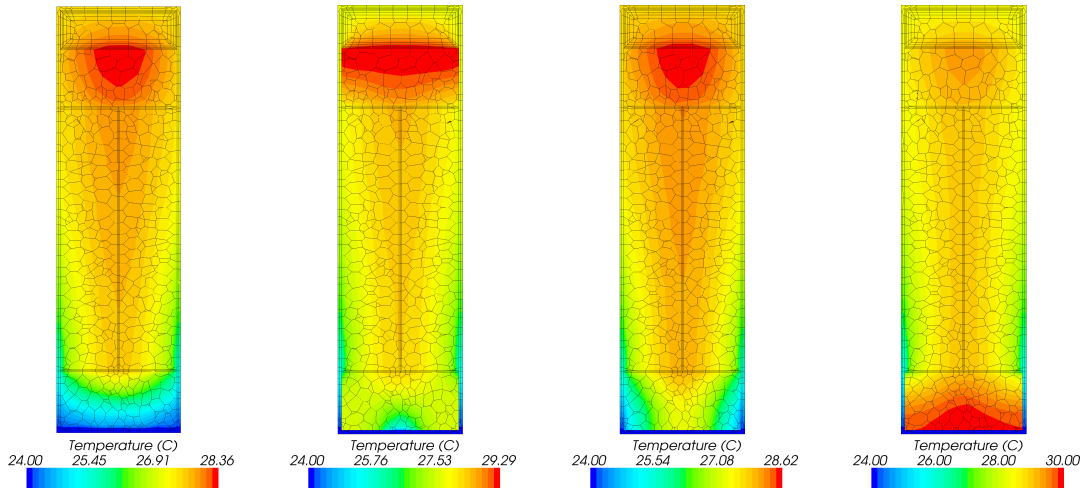

(a) Air gap neglected. **(b)** Air gap included. **(c)** Interface bottom isolated. **(d)** Interfaces bottom and side isolated.

Fig. 3.35: Temperature, transverse sections through cell center, air gap study, model **II**, cases **a**–**d**.

3.6.3 Mesh Refinement Study

The aim of the refinement study is to find out whether mesh size has an effect on the computed results. Therefore a series of steady state simulations is computed where the *base size*, which is the most important reference value of the polyhedral meshing model, is varied. Afterwards, power loss and center-temperature are evaluated. The refinement study is performed by utilizing the plain cell model.

Cell count	Base size	Power loss P	Temperature θ_c
	mm	W	°C
954 504	2	8.11	38.56
301 092	5	8.11	38.56
133 057	8	8.12	38.59
63 633	11	8.13	38.54

Tab. 3.15: Results of the mesh refinement study. Comparison of numerical steady-state results of power loss P and temperature of probe Center θ_c.

Table 3.15 provides the data of the evaluation, base size and obtained cell counts are listed additionally. It is found that mesh size does not affect results significantly. Since the temperature gradient is rather small, only a coarse mesh resolution is required to resolve the temperature profile. The study does not include any coarser base size, as a valid mesh owning less cells than approximately 60 000 is not achieved. In chapter 4

(pack models) slightly greater temperature gradients are expected. Therefore, a base size of 8 mm is also used for the pack models.

3.6.4 Disregard of Conduction within the Power Cables

As mentioned before, heat conduction within power cables is considered by a temperature boundary condition at the terminal bolts. In this section information about the error is given if conductive heat transfer is omitted. Therefore a transient simulation (plain cell model) is performed, in which the temperature boundary condition is replaced by a heat flux boundary condition corresponding to aluminum surfaces (compare table 3.10).

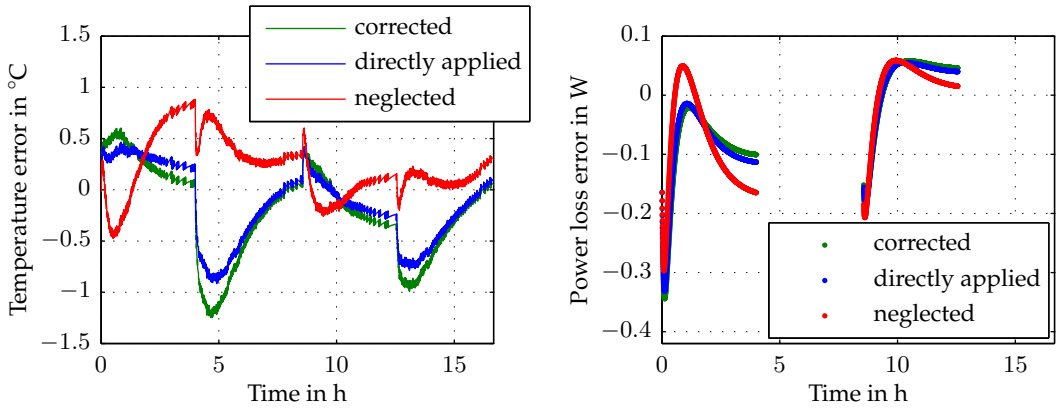

Fig. 3.36: Neglecting power cables, error of center-temperature and power loss.

Figure 3.36 compares errors obtained from three simulations. Curve *directly applied* relates to the very first simulation which is performed to determine a temperature correction (paragraph *Transient Simulation* on page 30). Curve *corrected* had already been covered in the results section and curve *neglected* is obtained from the aforementioned simulation. At first, the initial cycling and cooling-down period is discussed. The missing contribution in heat transfer is clearly shown. The temperature error is negative where usually heat is fed in and positive elsewhere. Therefore the power loss error overswings to a greater extent, but is still limited to $\Delta P = -1.9\,\%$ at steady state ($t \approx 4\,\mathrm{h}$). During the second cycling and cooling-down period, the overestimation of convective heat dissipation is compensated, which actually improves power loss error. As conclusion, the error introduced by neglecting the power cables remains limited, as temperature and power loss are inversely correlated.

4 Pack Models

The term *battery* means an energy storage system containing one or more appropriately connected cells. In vehicular applications a lot of cells are used in order to increase the total electric energy of the battery, a high power output is obtained by connecting part of them in parallel. In this particular case the battery comprises a series of 86 cell sets, in which each cell set consists of three cells in parallel connection.[1] Four of these sets are organized into a module, which is referred to as *pack* in the following. The connection scheme of the pack is shown in figure 4.1. As mentioned in the introduction, only a single pack (12 cells) is simulated within the framework of the project.

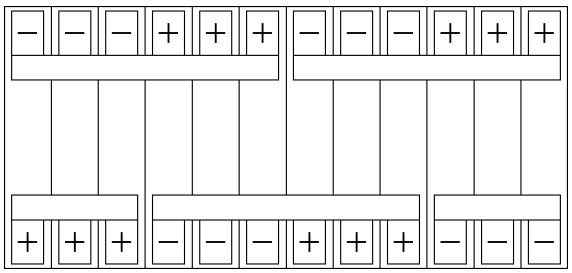

Fig. 4.1: Connection scheme of the cell pack.

This chapter describes the model development for a single pack. To build the pack model, the derived cell model is arranged in the above scheme and the terminals are connected via busbars. The assembly is enclosed by a pack casing. For the purpose of cooling the pack, three different concepts are considered:

- Liquid cooling by a cooling plate
- Gaseous cooling by a cooling duct
- Gaseous cooling by an air gap

These concepts are investigated in the following sections. The boundary conditions and objectives of the individual concept differ slightly for each alternative. The key objective of the simulations is to determine the spatial temperature distribution across the pack. In doing so two concerns are of particular interest:

- Homogeneity of the spatial temperature field across the jelly rolls
- General cooling capability of the individual concept

[1] Nominal specification of the battery: $V_{\text{batt}} = 316\,\text{V}$, $C_{\text{batt}} = 67.5\,\text{A h}$. Power output ($i = 1C$): $P_{\text{el}} \approx 21\,\text{kW}$.

Because of the higher model complexity, the geometry can not be created with use of 3D-CAD in a satisfying manner. Therefore, the geometry is developed by utilizing Pro/ENGINEER Wildfire and imported into Star-CCM+ using the *Parasolid Transmit* file format.[2]

4.1 Cooling Plate Model

To realize this concept, a metal plate is affixed at the bottom surfaces of the cells and coolant is conducted through a circular hole in the center of this plate. A *thermal pad*, installed at the contact area of cooling plate and cells, eliminates manufacturing inaccuracies and ensures heat transfer. For safety reasons, all parts have to be electrically separated. Therefore an insulation paper made of aramid is inserted between the cells and between cells and pack casing. The pack casing consists of sheet metal and a terminal cover. The specific aim of the model is to determine the amount of heat dissipating by the coolant depending on coolant flow rate and thermal pad characteristics.

4.1.1 Modeling Assumptions, Geometry and Mesh

The thermal pad is sufficiently characterized by pad height and thermal conductivity of the pad material as only steady state simulations are performed. Since the height is small compared to the planar dimensions of the pad, geometric modeling of the pad is omitted. Instead, the pad is considered by a thermal contact resistance R_{pad} introduced at the interfaces connecting cells and cooling plate. In other words, one combined parameter replaces two former parameters, the consequence being that the total number of necessary simulation runs is reduced. Further advantages are a smaller number of mesh cells and – as only parameters have to be adapted to set up another case – the reusability of the mesh. Hence, this approach lessens simulation cost. The same conclusions are drawn concerning the aramid paper. The paper is also replaced with a thermal contact resistance R_{ap}.

The design of the cooling plate and the pack casing is provided by the project partner. For reasons of simplifications, irrelevant geometric details of the design are not included in the model. The following simplifications are made:

- Pack casing represented through rectangular plates
- Simplified terminal cover, avoidance of small gaps
- Geometric modeling of the aramid paper omitted
- Geometric modeling of the thermal pad omitted

[2]Geometry data can be imported as region, part, or body, but it is highly recommended to import the geometry as body. In doing so, work load is reduced tremendously as running the Imprint-operation within 3D-CAD automatically generates part contact data. (Compare remark on page 18.)

Figure 4.2 presents the final pack geometry. The pack casing is assembled by two parts which are referred to as cover plate (14 mm thick) and side plate (1 mm thick), respectively. The terminal cover (1.5 mm thick) is created in such a manner that the terminals are precisely enclosed, disregarding small gaps between terminals and cover. With other words, a very fine mesh is avoided in vicinity of the gaps. Based on experience of the cell model simulations, the air inside the cover is assumed to be (almost) quiescent and heat conduction in missing gaps is considered by a thermal contact resistance R_{gap}. The open volume inside the cover is referred to as terminal cavity. As in reality the battery is incorporated in the car structure, choice of thermal boundary conditions is a quite difficult task. To appropriately represent the installation situation in the car, the whole pack is placed inside an air volume. The outer surface of the air volume is modeled as wall (no-slip condition) and the temperature of this wall is set to a constant value. The distance between pack and outer surface is chosen to be 1 cm. This approach represents the metal housing of the entire battery and is confirmed by the project partner. The air volume is referred to as environment.

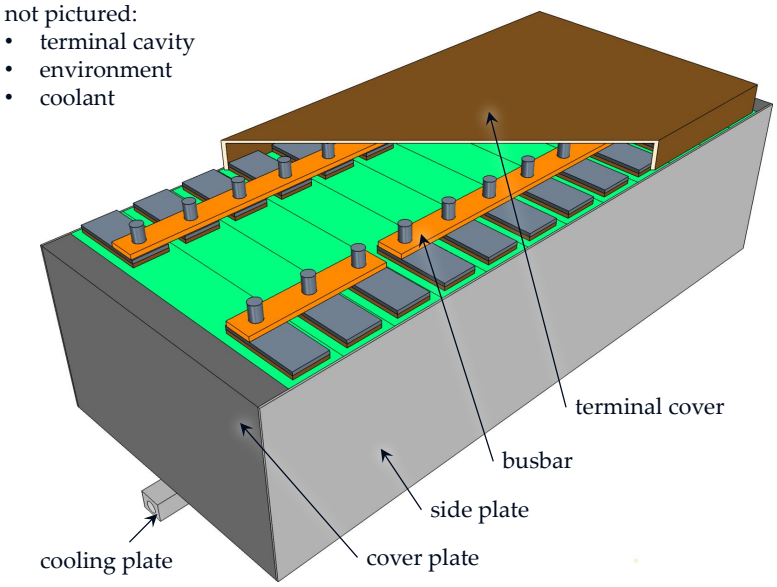

Fig. 4.2: Geometry of the cooling plate model.

The main dimensions of the cooling plate are 100 mm by 318 mm, meaning that the plate covers all cells in longitudinal direction (compare figure 4.5). As the aramid paper in between the cells is represented by a contact resistance, the thermal pad length – and thus pad area – is reduced by paper thickness times eleven. This is a negligible error, especially as the contact zone of the vertical paper and the horizontal cooling plate is rather small. Furthermore, the paper has very low thermal conductivity and therefrom the heat conduction inside the paper (parallel to surface) is of minor importance. The coolant passage has a diameter of 6 mm. Because of modeling requirements, the coolant passage is designed up to the enclosing surface of the environment. To prevent a thermal bridge being established, a thermal contact resistance R_{cp} is introduced between cover

plate and cooling plate. The locations of the particular contact resistances are provided in figures 4.3 and 4.4. The figures also show the cross-sectional shape of the cooling plate.

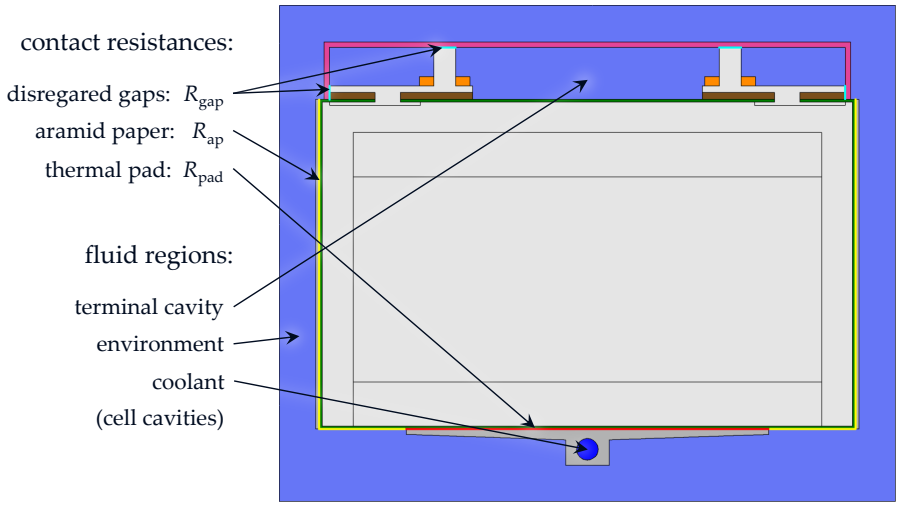

Fig. 4.3: Geometry. Transverse section through the first cell.

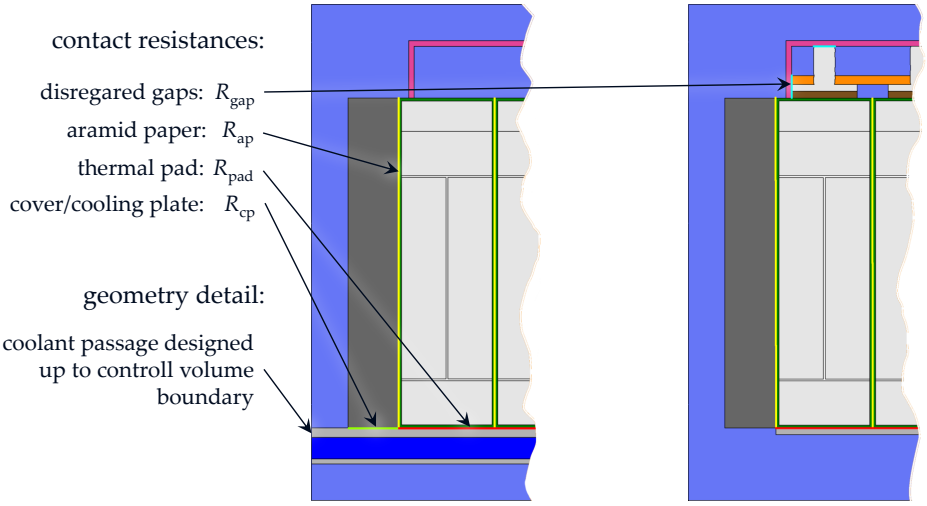

Fig. 4.4: Geometry. Longitudinal sections through the pack center (left side) and the terminals (right side).

The mesh is built by employing the polyhedral meshing model. Prism layer meshes are generated at all faces contacting a fluid region. The coolant domain is meshed using the *Generalized Cylinder Mesher*. This sub method of the polyhedral mesher generates an extruded mesh along the length of the coolant passage, reducing the overall cell count. Furthermore, the rate of convergence is improved. Around the busbars, refinement areas are defined to locally increase mesh density. Within the environment, the mesh resolution is also improved by increasing the *Poly density*-factor from the default value

1 to 1.2. Figure 4.5 represents the generated mesh. The detail shows the generalized cylinder mesh of the coolant, where some of the internal cells have been exposed. In summary, the model consists of 147 regions which are connected via 660 interfaces. The overall cell count is approximately 3 500 000.

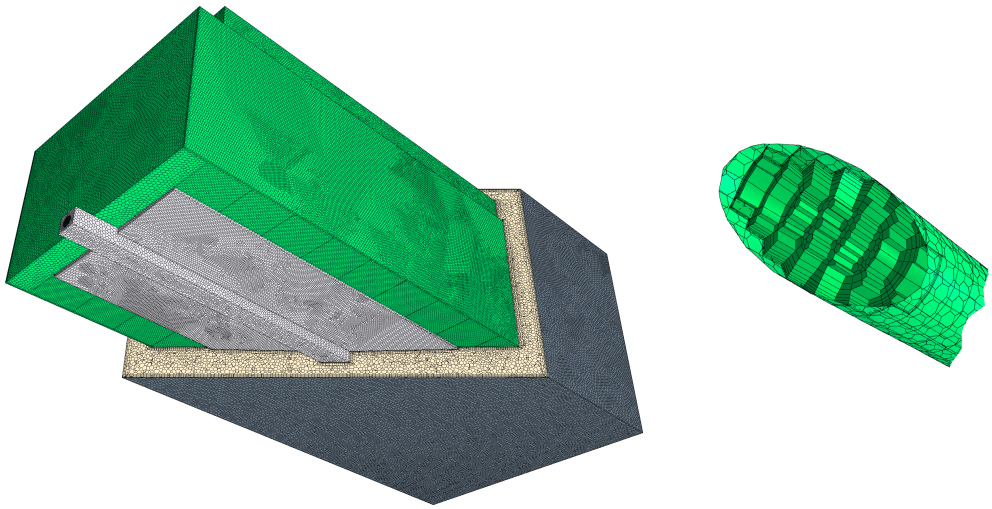

Fig. 4.5: Mesh of the cooling plate model (left side). The cooling plate is highlighted in light gray and the surrounding air volume is cut. The extruded mesh of the coolant region (right side) is generated by employing the generalized cylinder mesher.

4.1.2 Parameters and Boundary Conditions

As stated, the previously derived cell model forms the basis for simulating the pack. Hence, all material parameters regarding the cell can be looked up in chapter 3. With reference to the electric model, the electrical conductivity curve σ_{all} (equation (3.24)) is applied to all cells. This setting implies that the cells are equally conditioned in their electrical behavior. The coolant is a solution of 50 % by volume ethylene glycol and 50 % by volume water. Coolant parameters are determined for a temperature of 30 °C and presented in table 4.1. As material parameters of the coolant only vary marginally over the observed temperature range, they can be assumed to be constant. The materials of the additional regions are listened in table 4.2. All material properties are provided by references to earlier chapters.

Name	Material	Specific heat	Thermal conductivity	Dynamic viscosity	Density	Reference
		$\mathrm{J\,kg^{-1}\,K^{-1}}$	$\mathrm{W\,m^{-1}\,K^{-1}}$	$\mathrm{mPa\,s}$	$\mathrm{kg\,m^{-3}}$	
Coolant	Solution	3319	0.383	2.94	1068.8	[1]

Tab. 4.1: Material properties of coolant.

Name	Material	Table
Busbar	Copper	
Cooling plate	Aluminum	
Cover plate	Aluminum	3.6
Side plate	Aluminum	
Terminal cover	Polycarbonate	
Terminal cavity	Air	3.7
Environment	Air	

Tab. 4.2: Materials of cooling plate model (exclusive cells/coolant).

To obtain meaningful pad resistance values, literature has been searched for appropriate parameters for thermally conductive films. As the project partner rejects any silver-containing thermal pastes and limits the maximum thickness of the pad, the following bounds for specification of the pad parameter are given:

- Pad thickness: 0 to 3 mm
- Thermal conductivity [8]: 0.8 to 3 $\mathrm{W\,m^{-1}\,K^{-1}}$

Using these bounds, the range of thermal contact resistance is determined to $R_{\mathrm{pad}} = 0$ to $0.003\,75\,\mathrm{m^2\,K\,W^{-1}}$. The aramid paper has a thermal conductivity of $\lambda_{\mathrm{ap}} = 0.139\,\mathrm{W\,m^{-1}\,K}$ [19] and a thickness of $s_{\mathrm{ap}} = 0.25\,\mathrm{mm}$. Hence, the contact resistance replacing the aramid paper results in $R_{\mathrm{ap}} = 0.0018\,\mathrm{m^2\,K\,W^{-1}}$. The width of the disregarded gaps is assumed to be $s_{\mathrm{air}} = 1\,\mathrm{mm}$, giving an air gap resistance of $R_{\mathrm{gap}} = 0.0385\,\mathrm{m^2\,K\,W^{-1}}$. Contact resistances applied to the interfaces of cooling plate and cover plates are arbitrarily chosen to be $R_{\mathrm{cp}} = 10\,\mathrm{m^2\,K\,W^{-1}}$ in order to restrict heat transfer to thermal pad area.

As mentioned in the geometry section, the installation situation in the car is represented by a constant temperature boundary condition. In doing so, the wall temperature of the environment-region is set to $\theta_{\mathrm{e}} = 30\,^{\circ}\mathrm{C}$. Front face and end face of the cooling passage[3] are set adiabatic. Heat transfer across the control volume boundary is also caused by inflowing and escaping coolant. The boundary conditions of the coolant are chosen as follows:

- Velocity inlet: $\vec{v}_{\mathrm{in}}$, $\theta_{in} = 10\,^{\circ}\mathrm{C}$
- Pressure outlet: $p_{\mathrm{out}} = 0\,\mathrm{Pa}$, reference pressure $p_{\mathrm{ref}} = 1013.25\,\mathrm{mPa}$

To obtain a suitable flow velocity, the very first simulation is performed using a manually estimated volumetric coolant flow rate $\dot{V}$. This first value serves as a starting point for finding coolant flow rates for further simulations. As the obtained *Reynolds numbers*[4]

[3] These very small surfaces of the cooling plate are coplanar to the environment surface.

[4] The Reynolds number Re gives a measure of the ratio of inertial forces to viscous forces and is used to characterize flow regime. In conventional applications, laminar pipe flow is obtained below a critical threshold of $Re_{\mathrm{c}} \approx 2300$ [3].

are far below the critical threshold, the coolant flow occurs in the laminar flow regime. As a consequence of this, the velocity profile within the circular coolant passage can be described by a parabolic function (*Hagen-Poiseuille* flow [9]). Being r_0 the radius of the passage and r the radial distance from the passage's longitudinal axis (with unit vector $\vec{e}_x$), the inlet velocity profile is specified to:

$$\vec{v}_{in}(r) = \frac{8\,\dot{V}}{r_0^2\,\pi}(r_0^2 - r^2) \cdot \vec{e}_x \tag{4.1}$$

The coolant flow rate is varied within the range of $\dot{V} = 1 \cdot 10^{-7}$ to $5 \cdot 10^{-6}\,\mathrm{m^3\,s^{-1}}$. At last electric boundary conditions are addressed. Each cell is loaded with a current of $i = 46.7\,\mathrm{A}$.

Flows inside the air regions (environment, terminal cavity, cell cavities) are driven by buoyancy only, therefrom they are computed using a laminar flow model. As implied in the previous paragraph, a laminar flow model is used for the coolant region as well. Results are obtained by performing steady state simulations. To improve the rate of convergence, under-relaxation factors are increased in a similar manner as for the cell model. For investigating the cooling concept, a parameter study has to be carried out. In this respect, an automation of setup and simulation of each case – enabled by Star-CCM+'s capability of executing *Macros* as well as sequencing simulation runs using *bash scripts* – is very desired. To optimize turnaround time, two stopping criteria are specified which make use of the power balance equation. The residual $\mathcal{R}_P$ of the power balance equation is given as:

$$\mathcal{R}_P = P_{ohmic} + \dot{Q}_{in} - \dot{Q}_{out} \tag{4.2}$$

The residual includes waste heat (power loss P_{ohmic}) generated inside the model and heat flows ($\dot{Q}_{in|out}$) crossing the control volume boundary. Being $\mathcal{R}_P \approx 0$ indicates a fully converged steady state solution. The stopping criteria are defined as follows:

- Minimum criterion:

$$|\mathcal{R}_P| \leq 0.25\,\mathrm{W} \tag{4.3}$$

- Asymptotic criterion:

$$|\max(\mathcal{R}_P) - \min(\mathcal{R}_P)| \leq 0.25\,\mathrm{W} \text{ within 150 iterations} \tag{4.4}$$

The first criterion is satisfied if the residual falls below the limit. The second criterion limits the range over which the residual can fluctuate in the given number of iterations, in which the number is counted backwards from actual iteration number. It is introduced as the residual order shows a oscillating behavior. Both criteria have to be fulfilled to stop the analysis. As a result, permanent supervision of the progressing solution is superfluous.

To recap, the investigation of the cooling plate concept is made by performing steady state simulations in which thermal contact resistance of the pad and coolant flow rate are varied. The following parameters are covered in the study:

- $R_{\text{pad}} = \{0, 1.25, 2.50, 3.75\} \cdot 10^{-3}\,\text{m}^2\,\text{K}\,\text{W}^{-1}$
- $\dot{V} = \{0.1, 0.3, 0.5, 1, 3, 5\} \cdot 10^{-6}\,\text{m}^3\,\text{s}^{-1}$

4.1.3 Results

First of all, table 4.3 gives an overview on coolant flow rates using more common and more descriptive units. The obtained numerical values are rather low, but they seem to be reasonable as a battery has a high efficiency. Furthermore, the single pack represents only a small part of the battery and cooling flow rate for the entire battery is significantly higher.

Volume flow rate[5] $\dot{V}$	$\text{m}^3\,\text{s}^{-1}$	1e-7	3e-7	5e-7	1e-6	3e-6	5e-6
Mean velocity	$\text{m}\,\text{s}^{-1}$	0.004	0.011	0.018	0.035	0.106	0.177
Volume flow rate	$\text{L}\,\text{h}^{-1}$	0.36	1.08	1.80	3.60	10.80	18.00
Mass flow rate	$\text{kg}\,\text{h}^{-1}$	0.4	1.2	1.9	3.9	11.5	19.2
Reynolds number	1	8	23	39	77	231	386

Tab. 4.3: Overview of coolant flow rate.

Table 4.4 provides outlet temperatures of the coolant, which are obtained by mass flow averaging over outlet surface. The outlet temperature is mainly affected by the coolant flow rate. The table indicates that only a pad resistance $R_{\text{pad}} = 0$ is simulated for flow rates $\dot{V} = \{1\text{e-}7, 5\text{e-}6\}\,\text{m}^3\,\text{s}^{-1}$. In case of the lower flow rate, the jelly roll temperatures

R_{pad}	$\dot{V}$					
	1e-7	3e-7	5e-7	1e-6	3e-6	5e-6
0	52.2	33.2	25.7	18.8	13.4	12.1
1.25e-3		32.6	25.3	18.6	13.3	
2.50e-3		32.3	25.0	18.4	13.2	
3.75e-3		32.0	24.8	18.3	13.1	

Tab. 4.4: Coolant outlet temperature in °C.[6]

are obtained lying beyond the temperature limit of operation (45 °C). In case of the higher flow rate, the jelly roll temperatures are found far below wall temperature of the environment-region, meaning that the car structure is cooled down by the coolant. Consequently, no further simulations are performed regarding these flow rates and pad parameters $R_{\text{pad}} \neq 0$. That fact is also confirmed by figure 4.6. The figure provides extreme and average jelly roll temperatures for case $R_{\text{pad}} = 0$, in which the full range of

[5] For the sake of compactness, *scientific e notation* is used to specify $\dot{V}$ and R_{pad} throughout this section.
[6] $[R_{\text{pad}}] = \text{m}^2\,\text{K}\,\text{W}^{-1}$, $[\dot{V}] = \text{m}^3\,\text{s}^{-1}$.

flow rate is simulated. These temperature are found by evaluating the volume of all jelly rolls.The maximum temperature decreases by approximately 14 °C within the interesting range of flow rates ($\dot{V} = \{3e\text{-}7 \ldots 3e\text{-}6\}\,m^3\,s^{-1}$) and gives a reasonable approximation of the average temperature. The behavior of the average temperatures being just slightly below the maximum temperatures does not change for alternating pad resistances.

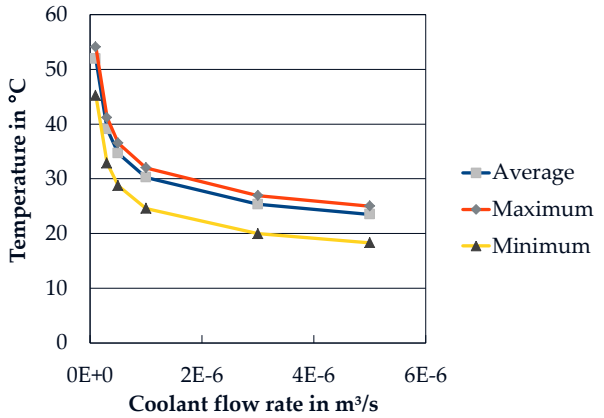

Fig. 4.6: Temperatures within jelly rolls for $R_{pad} = 0$.

As illustrated in figure 4.7, the temperature minimum is located near the inlet boundary (front end of the pack). The hottest zone is found close to the upper rear pack end. This hot zone is moving towards pack center (to the left in figure 4.7) with increasing temperature level, which is a consequence of the temperature boundary condition. While a pronounced temperature gradient develops in longitudinal direction of the pack, the temperature gradient transversally to the pack is negligibly small.

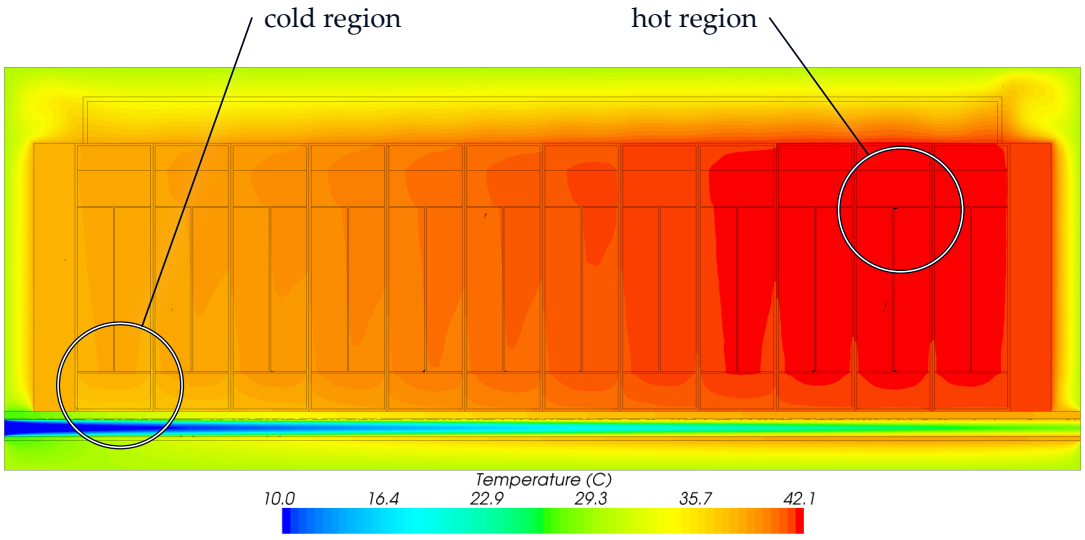

Fig. 4.7: Temperature, longitudinal section through pack center, $R_{pad} = 3.75e\text{-}3\,m^2\,K\,W^{-1}$, $\dot{V} = 3e\text{-}7 m^3\,s^{-1}$.

The temperature field in transverse direction is shown in figure 4.8, in which *first cell* and *last cell* refers to coolant flow direction. The pad resistance introduces a temperature drop across the interfaces of cells and cooling plate. The temperature drop, as well as the heat flux into the coolant, reduces along the cooling plate as coolant heats up while flowing through the passage. This fact causes the hot zone to be located at the rear pack end. Figure 4.9 provides the temperature drop as a function of coolant flow rate, in which the drop is determined for each individual cell-cooling plate interface. In doing so, temperatures are surface-averaged on both sides of the interface and subtracted eventually. The curve *cell 1* corresponds to the interface of the *first cell*, the consecutive numbering refers to coolant flow direction. The obtained temperature drop seems to be realistic, confirming the suitable choice of pad resistance values.

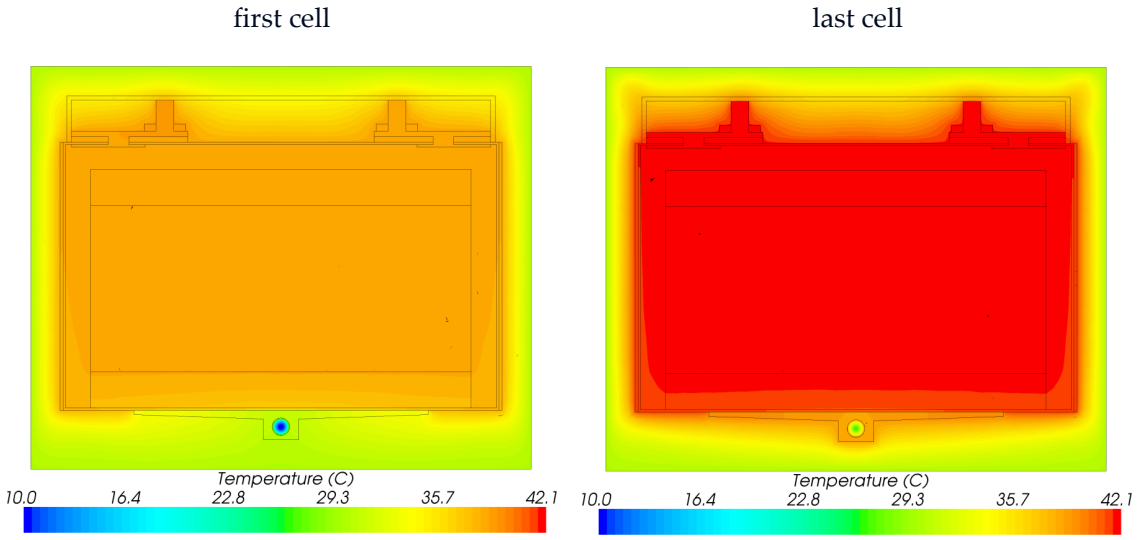

Fig. 4.8: Temperature, transverse sections through pack, $R_{\text{pad}} = 3.75\text{e-}3\,\text{m}^2\,\text{K}\,\text{W}^{-1}$, $\dot{V} = 3\text{e-}7\text{m}^3\,\text{s}^{-1}$.

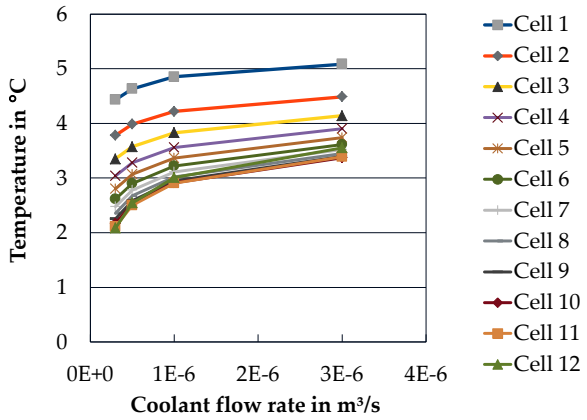

Fig. 4.9: Temperature drop across the thermal pad for $R_{\text{pad}} = 3.75\text{e-}3\,\text{m}^2\,\text{K}\,\text{W}^{-1}$.

For evaluation of the cooling concept, two critical parameters are defined:

- Maximum temperature: describes the general cooling capability
- Maximum temperature difference: describes the homogeneity of the temperature field

The second parameter is calculated from the difference of maximum temperature and minimum temperature. As mentioned before, these extreme values are found in evaluating the volume of all jelly rolls. Figure 4.10 shows these critical parameters as function of coolant flow rate and pad resistance.

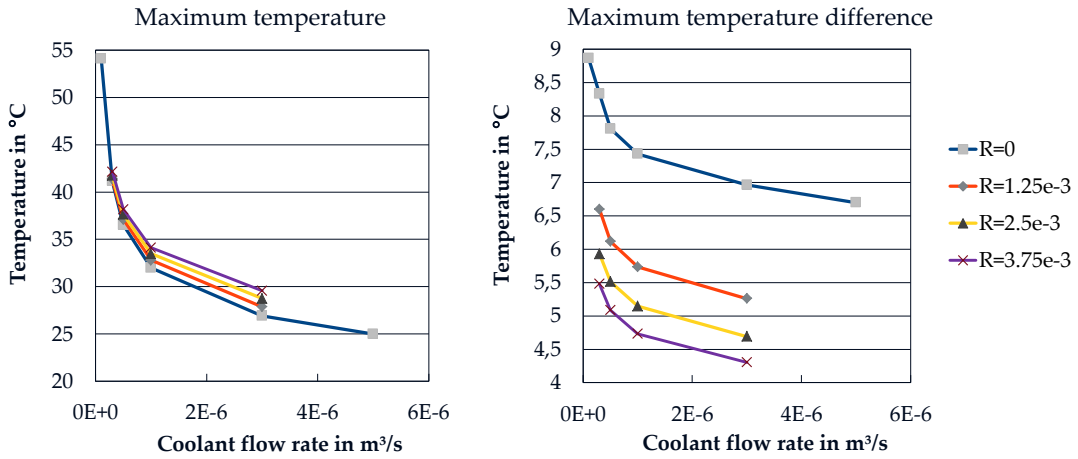

Fig. 4.10: Temperatures within jelly rolls dependent on R_{pad} and $\dot{V}$.

The jelly roll temperature is mainly influenced by the coolant flow rate, as already suggested in the discussion of coolant outlet temperature (table 4.4). While the pad resistance has minor influence on the maximum temperature, the temperature spread is considerably reduced when pad resistance increases. To provide an example, results of case $R_{\text{pad}} = 3.75\text{e-}3\,\text{m}^2\,\text{K}\,\text{W}^{-1}$ and case $R_{\text{pad}} = 0$ are compared with regard to coolant flow rate $\dot{V} = 1\text{e-}6\,\text{m}^3\,\text{s}^{-1}$. Introducing the pad resistance increases the maximum temperature by approximately 5 % (1.6 °C), whereas the maximum temperature difference is decreased by approximately 35 % (−2.7 °C). In other words, a thermal pad homogenizes the temperature field but raises the general temperature level. It should be mentioned that this effect may benefit from the model's boundary condition. As the thermal pad isolates the cells against the cooling plate, a larger percentage of waste heat has to be dissipated at the surface of the environment-region to achieve a steady state solution (10 % versus 6 % in above cases). As at this surface a constant temperature is applied, the spatial temperature distribution develops more uniformly across the pack.

Finally, table 4.5 provides the findings respective power loss. An average power loss per cell of $P_{\text{cell}} \approx 2.5\,\text{W}$ is given on the basis of all results.[7] Comparing coolant flow rates $\dot{V} = 3\text{e-}7\,\text{m}^3\,\text{s}^{-1}$ and $\dot{V} = 3\text{e-}6\,\text{m}^3\,\text{s}^{-1}$, the power loss increases 16 % in average.

[7] A efficiency of ≈1.5 % is obtained assuming nominal cell voltage.

Figure 4.11 presents the net heat transfer of the coolant. The coolant heat transfer exceeds power loss in cases of high flow rates, corresponding to the earlier mentioned fact that the car structure is cooled down. Having said this, the heat is flowing into the model across the control volume boundaries (surface of environment-region). A clear presentation of these results is also given in table A.1 in the appendix. There heat flow across the thermal pad (table A.2) is discussed as well.

R_{pad}	$\dot{V}$					
	1e-7	3e-7	5e-7	1e-6	3e-6	5e-6
0	25.6	28.4	29.7	31.2	33.3	34.2
1.25e-3		28.3	29.5	30.9	32.8	
2.50e-3		28.2	29.3	30.6	32.4	
3.75e-3		28.0	29.1	30.3	32.0	

Tab. 4.5: Total power loss of the pack in W.[8]

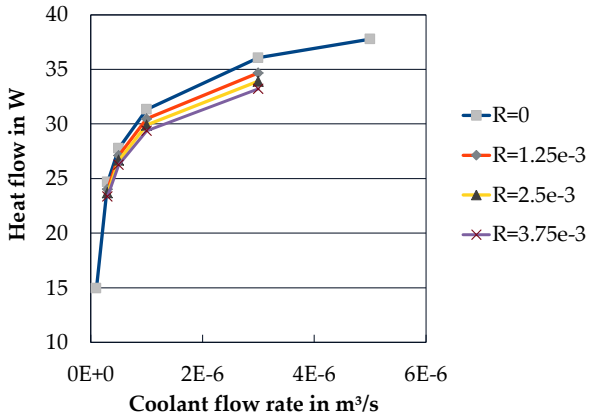

Fig. 4.11: Net heat transfer of the coolant.

4.2 Cooling Duct Model

The cooling concept presented in this section is almost identical with above concept of the cooling plate. However, the cooling plate is replaced by a cooling duct. Instead coolant, air is conducted through the duct. The specific aim of this model is to evaluate the heat transfer capability of the system with respect to the cooling air condition at the inlet. The boundary condition for cooling air is specified by temperature and volume flow rate.

[8] $[R_{\text{pad}}] = \text{m}^2\,\text{K}\,\text{W}^{-1}$, $[\dot{V}] = \text{m}^3\,\text{s}^{-1}$.

4.2.1 Modeling Assumptions, Geometry and Mesh

As density and specific heat of air are much lower than those of the coolant, the volume flow rate of the cooling air has to be larger to obtain appropriate heat dissipation. As a consequence, a larger cross-sectional size of the duct is required as well. The duct has a rectangular cross-sectional shape measuring a width of 100 mm and a height of 15 mm. The wall of the duct is 0.5 mm thick. An enclosing box (environment) is generated using a clearance of 1 cm between pack and box boundary. The rest of the pack geometry is identical to the above geometry, as well as modeling assumptions. In particular, the contact resistances R_{pad}, R_{ap}, R_{gap}, and R_{cp} are introduced again. Figure 4.12 provides a transversal section through the pack. The cross-sectional shape of the duct as well as locations of the contact resistances are shown in this figure.

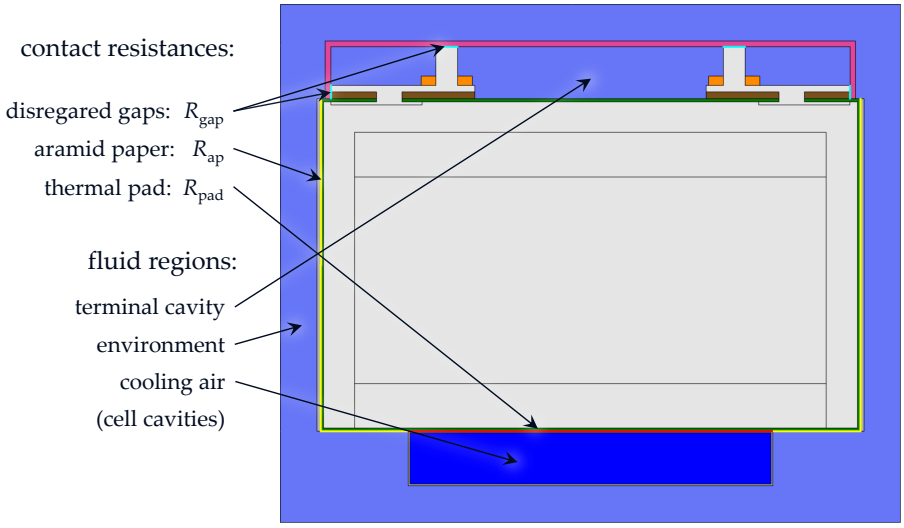

Fig. 4.12: Geometry. Transverse section through the first cell.

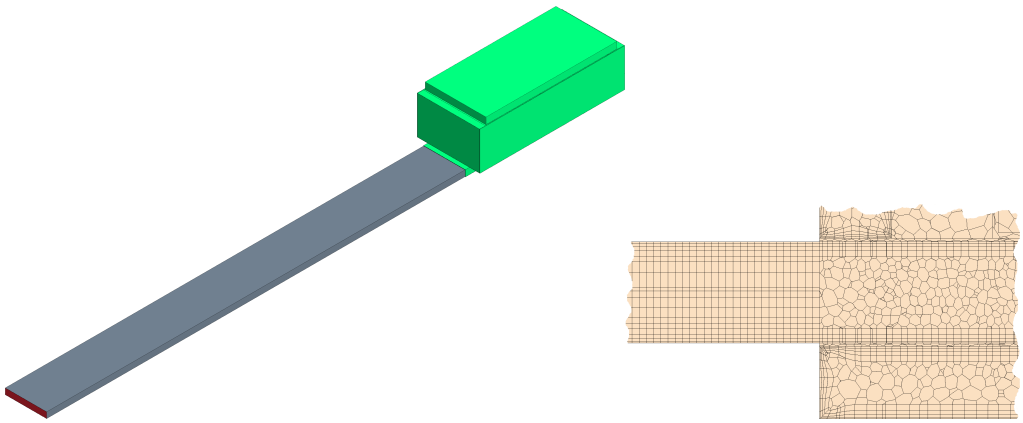

Fig. 4.13: Pack geometry and extrusion of the inlet boundary (exclusive environment). The detail shows the area around the inlet boundary (longitudinal section, inclusive environment).

The mesh is generated using the polyhedral meshing model, prism layer meshes are attached to boundaries with fluid contact. Unlike as for circular pipes, a description of the laminar velocity profile by a closed formula is not feasible. Moreover, volume flow rates enforcing a turbulent flow regime are also considered. The flow profile at the inlet boundary may further be influenced by the duct design upstream of the pack. As further information on the installation situation is not available, the flow profile at inlet boundary is assumed to be a fully developed pipe flow. In order to obtain a fully developed flow, an additional upstream extension of the flow domain is attached to the inlet boundary. In doing so, the *Extruder Meshing Model* is employed, which extends the volume mesh by extruding the core mesh of a specified boundary. Figure 4.13 illustrates the result of that extrusion.[9] The advantages are that the extruder mesher does not require any underlying geometry, and the length of the extension can easily be defined by changing mesher parameters. For the study, the length is set to 1 m. The final mesh includes the volumes of pack, environment, and inlet extrusion. It contains approximately 5 250 000 cells.

4.2.2 Parameters and Boundary Conditions

As thermal conductivity and viscosity of air cover a significant value range over the considered temperatures, a temperature-dependent relation is chosen to describe these parameters. The relation is also known as *Sutherland's law*, for dynamic viscosity it is given as [7]:

$$\frac{\mu}{\mu_0} = \left(\frac{T}{T_0}\right)^{3/2} \left(\frac{T_0 + S}{T + S}\right) \tag{4.5}$$

Therein T_0 and μ_0 are the reference temperature and the reference viscosity, respectively. The variable S denotes the Sutherland constant. The relation describing thermal conductivity has an identical structure but different reference values. An overview on the reference values is provided by table 4.6, while table 4.7 summarizes the cooling air material parameters. Cooling air is assumed to be dry, hence heat dissipation is estimated conservatively.

Name	Reference value	Reference temperature	Sutherland constant
Thermal conductivity	$0.024\,14\,\mathrm{W\,m^{-1}\,K^{-1}}$	273.15 K	194 K
Dynamic viscosity	$1.716 \cdot 10^{-5}\,\mathrm{Pa\,s}$	273.15 K	111 K

Tab. 4.6: Sutherland parameters of air.

The cooling duct is made of aluminum, so material parameters of the remaining regions are identical to table 4.2. The duct is assumed to be hydraulically smooth. With exception of the pad resistance, all thermal contact resistances are set as described in the previous

[9] See previous page 61.

Name	Material	Specific heat	Thermal conductivity	Dynamic viscosity	Molecular weight	Reference
		$\mathrm{J\,kg^{-1}\,K^{-1}}$	$\mathrm{W\,m^{-1}\,K^{-1}}$	$\mathrm{Pa\,s}$	$\mathrm{g\,mol^{-1}}$	
Cooling air	Air	1003.6	eq. 4.5, tab. 4.6	eq. 4.5, tab. 4.6	28.97	[6]

Tab. 4.7: Material properties of the cooling air.

section 4.1. The pad resistance is chosen to be $R_{\mathrm{pad}} = 1.875 \cdot 10^{-3}\,\mathrm{m^2\,K\,W^{-1}}$, expressing the mean value of the former investigated interval.

Just as for the cooling plate model, an electric current of $i = 46.7\,\mathrm{A}$ is applied to each cell and the temperature boundary condition of the enclosing box is set to $\theta_{\mathrm{e}} = 30\,^{\circ}\mathrm{C}$. Extruding the inlet boundary generates some new model surfaces. The front surface is equally shaped as the flow section and embodies the *new* inlet boundary with face normal $\vec{e}_{\mathrm{x}}$. The lateral surface of the extrusion is set as adiabatic wall. Cooling air boundary conditions are chosen as follows:

- Velocity inlet: $\vec{v}_{\mathrm{in}}(x, y)$, θ_{in}
- Pressure outlet: $p_{\mathrm{out}} = 0\,\mathrm{Pa}$, reference pressure $p_{\mathrm{ref}} = 1013.25\,\mathrm{mPa}$

Being a, b the dimensions of the flow section, inlet velocity is specified as:

$$\vec{v}_{\mathrm{in}}(x, y) = \frac{\dot{V}_{\mathrm{in}}\,\pi^2}{4\,a\,b}\,\sin(\frac{\pi\,x}{a})\,\sin(\frac{\pi\,y}{b}) \cdot \vec{e}_{\mathrm{x}} \tag{4.6}$$

This equation describes a simple sinusoidal velocity profile generating a volume flow rate $\dot{V}_{\mathrm{in}}$. Using an appropriate coordinate system, zero velocity is obtained at the wetted perimeter of the duct and the velocity profile already exhibits the fundamental shape of pipe flow. Both, laminar and turbulent flow regimes are covered. Based on experience gained from the air box model, the Realizable Two-Layer k-ϵ turbulence model is used to simulate cooling air flow in every case. This approach facilitates setting up the parameter study. The mesh size is checked to fulfill the aforementioned condition of wall distance ($y^+ < 1$) in particular cases. The results are obtained in performing steady state simulations. Stopping criteria as defined by equations (4.3) and (4.4) allow an automated sequencing of simulation runs.

Again, the cooling air flow rates are found by varying a starting value which is deduced in a manual estimation. They are bounded below by the temperature limit of cell operation, while an upper bound is given from the temperature boundary condition applied at the environment-region and the mean velocity. The range of investigation for inlet temperatures is defined by the project partner. The following list summarizes the parameters considered in the study:

- $\dot{V}_{\mathrm{in}} = \{0.5, 1.25, 2, 2.5, 2.75, 4.5, 6.5, 8.5, 10\} \cdot 10^{-3}\,\mathrm{m^3\,s^{-1}}$
- $\theta_{\mathrm{in}} = \{10, 20, 30\}\,^{\circ}\mathrm{C}$

4.2.3 Results

Table 4.8 presents an overview on the cooling air flow rate using descriptive units. As mentioned at the beginning of this section, the air flow rate has to be larger than the coolant flow rate in order to effect a required cooling capacity. Correlating the specific heat capacity of these fluids results in a factor $c_{\text{coolant}}/c_{\text{air}} \approx 3$. This factor is reflected if mass flow rates of tables 4.3 and 4.8 are compared.[10] In most cases a turbulent flow regime establishes as the obtained Reynolds numbers are above the critical threshold. The table also illustrates that mean velocities up to $7.2\,\text{m}\,\text{s}^{-1}$ are predicted. Because of the velocity profile, the maximum velocity is even higher. It is expected that such high velocities introduce acoustic noise in a real application. As a consequence, simulations with cooling air volume rates $\dot{V}_{\text{in}} > 0.01\,\text{m}^3\,\text{s}^{-1}$ are not performed.

Volume flow rate $\dot{V}_{\text{in}}$	Mean velocity	Volume flow rate	Mass flow rate[11]	Reynolds
$\text{m}^3\,\text{s}^{-1}$	$\text{m}\,\text{s}^{-1}$	$\text{L}\,\text{h}^{-1}$	$\text{kg}\,\text{h}^{-1}$	number[11,12]
5.00e-4	0.4	1 800	2.1	578
1.25e-3	0.9	4 500	5.4	1 444
2.00e-3	1.4	7 200	8.6	2 311
2.50e-3	1.8	9 000	10.7	2 888
2.75e-3	2.0	9 900	11.8	3 177
4.50e-3	3.3	16 200	19.3	5 199
6.50e-3	4.7	23 400	27.9	7 509
8.50e-3	6.1	30 600	36.5	9 820
1.00e-2	7.2	36 000	42.9	11 553

Tab. 4.8: Overview of cooling air flow rates.

Table 4.9 provides the outlet temperatures of the cooling air. The values are obtained by mass flow averaging over the outlet boundary. The temperature difference between inlet and outlet decreases with rising inlet temperatures and increasing volume flow rates. The blank cells in the table identify some pairs of parameters which are not considered in the study.

According to the cooling plate model, the critical parameters *Maximum temperature* and *Maximum temperature difference* are evaluated. The results are illustrated in figure 4.14. Using an inlet temperature $\theta_{\text{in}} = 30\,^{\circ}\text{C}$ does not allow safe operation of the pack as either the cell's temperature limit ($45\,^{\circ}\text{C}$) is exceeded or temperature safety margin is insufficiently small. Inlet temperatures $\theta_{\text{in}} = 10\,^{\circ}\text{C}$ and $\theta_{\text{in}} = 20\,^{\circ}\text{C}$ provide a wide parameter range of operational conditions. As expected, the curves of the maximum

[10] The temperature difference of the fluids between inlet and outlet boundary has also to be considered in this comparison. A similar argumentation can be made with the product of density and specific heat. Then a factor of ≈ 3000 is obtained, which is reflected in the ratio of volume flow rates.

[11] Calculated for $\theta_{\text{in}} = 20\,^{\circ}\text{C}$.

[12] To calculate Reynolds number correctly, the equivalent hydraulic diameter is used.

$\dot{V}_{in}$ in $m^3\,s^{-1}$	$\theta_{in} = 10\,°C$	$\theta_{in} = 20\,°C$	$\theta_{in} = 30\,°C$
5.00e-4	35.1	41.3	
1.25e-3	23.8	31.7	39.5
2.00e-3	19.9	28.4	36.8
2.50e-3			35.8
2.75e-3	17.9	26.7	
4.50e-3	15.4	24.6	33.7
6.50e-3	14.1	23.4	32.8
8.50e-3	13.3	22.7	32.2
1.00e-2	12.9	22.4	32.0

Tab. 4.9: Cooling air outlet temperature in °C. The blank cells identify pairs of parameters which are not considered in the study.

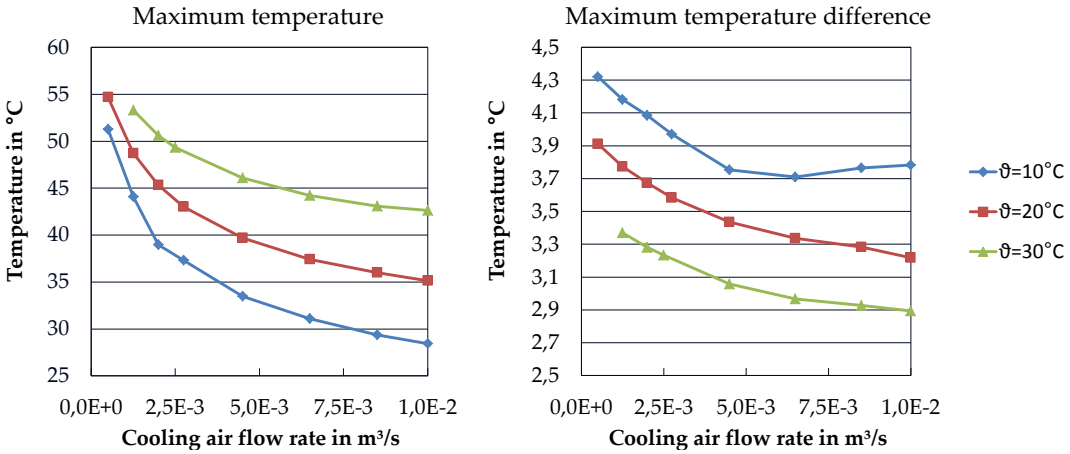

Fig. 4.14: Temperatures within jelly rolls dependent on θ_{in} and $\dot{V}_{in}$.

temperature difference have a similar characteristic when comparing the cooling duct model and the cooling plate model. On a closer examination, a more homogeneous temperature field is obtained from the cooling duct model. In doing so, two specific maximum temperature conditions are compared on the basis of:

- Identical inlet temperatures: Curves $\theta_{in} = 10\,°C$ of figure 4.14
- Identical pad resistances: a linear interpolation between curves $R_{pad} = 1.25e\text{-}3$ and $R_{pad} = 2.5e\text{-}3$ of figure 4.10

Table 4.10 gives the results of this comparison – less spread of the temperature field is obtained with the cooling duct model. It is assumed that this concept benefits from a large solid-fluid contact zone on the one hand. Although the duct walls are rather thin, the temperature field develops almost homogeneously along the wall. Thus, the entire inner surface contributes to heat transfer. This can be seen in figure 4.15, which provides temperature on transversal sections through the pack. On the other hand, a turbulent flow regime increases heat dissipation considerably.

Maximum temperature	Maximum temperature difference	
	Cooling duct model	Cooling plate model
30 °C	3.7 °C	5.1 °C
40 °C	4.1 °C	6.1 °C

Tab. 4.10: Maximum temperature difference compared for two values of the evaluation parameter maximum temperature.

Another interesting fact is that the curve of the maximum temperature difference (figure 4.14) is slightly increasing for high volume flow rates and inlet temperature $\theta_{in} = 10\,°C$. As the maximum temperature falls below the value of the temperature boundary condition (environment-region, $\theta_e = 30\,°C$) in these cases, the effect is presumably caused by instreaming heat flows. Finally, information on the net heat transfer of the cooling air is given in figure 4.16. As the temperature level of the cooling duct model is generally higher, the obtained power loss – and thus the net heat transfer – is lower compared to the cooling plate model. Additional information on the power loss is given in table A.3 in the appendix.

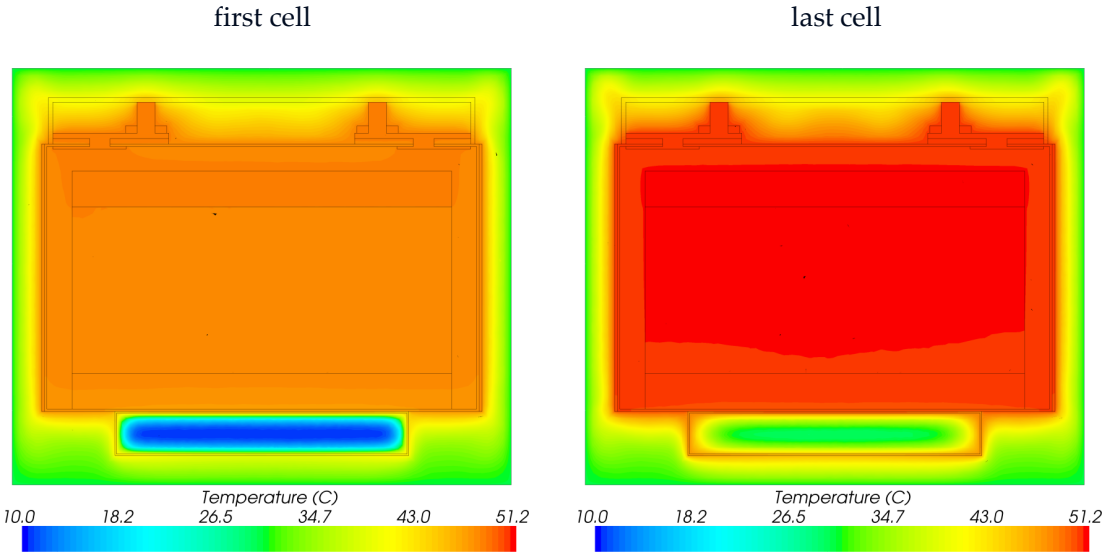

Fig. 4.15: Temperatures, transverse sections through the pack, $\theta_{\text{in}} = 10\,^{\circ}\text{C}$, $\dot{V}_{\text{in}} = 5 \cdot 10^{-4}\,\text{m}^3\,\text{s}^{-1}$.

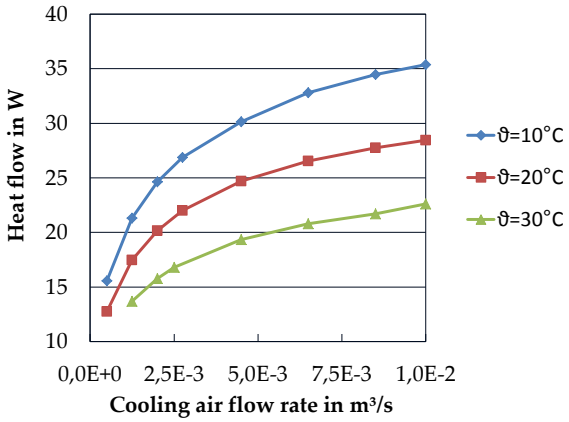

Fig. 4.16: Net heat transfer of the cooling air.

4.3 Air Gap Model

The cooling concept presented in this section is realized by conducting air through gaps lying in between the cells. The shape of the gaps is determined by spacers which also ensure structural stability of the pack. The specific aim of the model is to identify heat transfer capability of the concept with respect to gap width.

4.3.1 Modeling Assumptions, Geometry and Mesh

The spacers are positioned in between the cells and they are shaped in a meandering pattern as illustrated in figure 4.17. So air gaps formed by one spacer contact alternately cells being kept apart by this spacer. The figure also provides information on spacer dimensions, where d denotes the gap width. This parameter is varied in the investigation. Total height and total length of spacers and cell casings are equal, consequently they are arranged to one another in a flush manner.

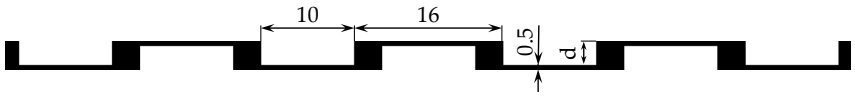

Fig. 4.17: Contour of spacer with dimensions and gap width d.

The pack is completed with busbars, a terminal cover, and a shell. The shell is composed of a side plate and two cover plates, illustrated as yellow and green parts in figure 4.18. Furthermore, cooling air volume is represented by the light blue part. As the figure indicates, cells are aligned upright in this concept and the flow direction of cooling air is from top to bottom. Additional spacers are positioned in between cover plates and outer cells. The orientation of the air flow is characterized by two basic domains. Firstly, a rectangular prism represents an air intake. The height of the prism measures 50 mm, the lateral and the longitudinal extent of the prism is defined in a way that all air gaps are covered completely. Secondly, cooling air is passed through the gaps. The entire cooling air domain is modeled as contiguous volume. For the sake of simplicity, an enclosing air volume as modeled in the above pack models is not included in this scenario. Instead, heat flow to the surroundings is established by applying a temperature boundary at the top surface of the terminal cover.

In contrast to above pack models, all CFD air gap models must be completely set up from scratch to perform the gap width study. From this it follows that a new geometry has to be created for each simulation case. To speed up this task, the CAD-model developed in Pro/ENGINEER contains a parameterized gap width. That means, the entire geometry[13] is modified by simply entering the gap width.

[13] In detail: Dimensions of spacer, busbars, terminal cavity, terminal cover, side plate, and cooling air volume are modified.

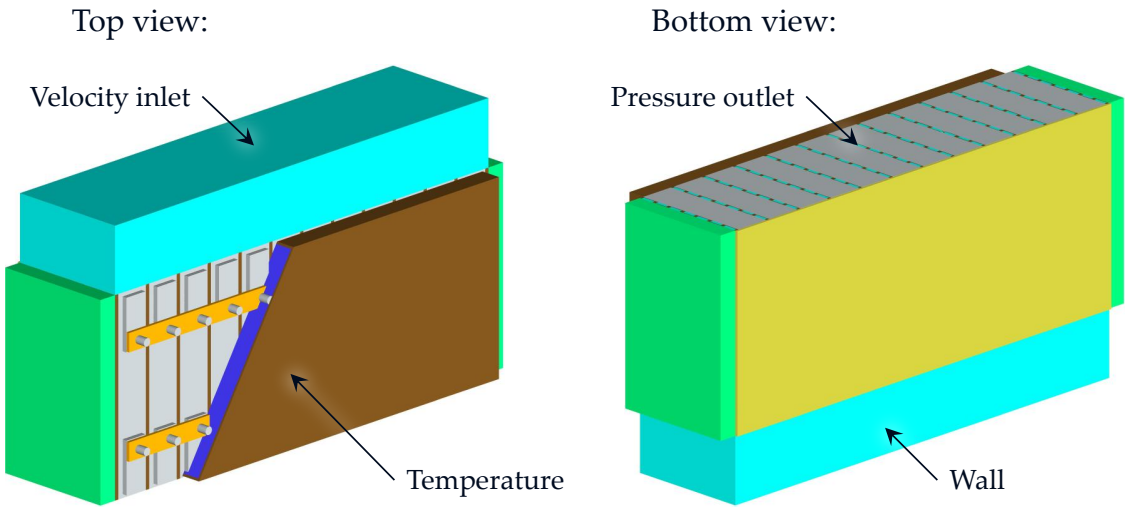

Fig. 4.18: Geometry and boundary conditions of the air gap model, terminal cover cut. The light blue volume represents the cooling air region. Surfaces not tagged by an arrow are set adiabatic.

The mesh is generated by employing the polyhedral meshing model, including prism layer meshes residing next to wall boundaries. Special care is taken to ensure a suitable transition of mesh density from a coarse mesh at inlet boundary to a very fine mesh at the entrances of the gaps. Especially, attention is paid to a sufficiently fine mesh resolution within the gaps. As the entire simulation process including meshing, model setup, and post-processing is automated, it is desired to come up with suitable prism mesh parameters in advance. Therefore, the flow field within a single gap is computed using a small test model.[14] The test model is used to optimize the near wall cell thickness in order to fulfill the aforementioned requirement for wall distance $y^+ < 1$. By computing a separate test model for each gap width, ideal values for local mesh size and prism mesh settings can be received eventually. Using this data, an adequate density of the pack mesh is obtained at the first attempt, and no further re-meshing process has to be executed. Furthermore, the mesh resolution is locally increased around the busbars. The cell count ranges from approximately 3 600 000 to 8 250 000. The pack models include 156 regions which are connected via 699 interfaces.

4.3.2 Parameters and Boundary Conditions

Since a significant increase of temperature is expected, the cooling air is described using temperature-dependent material properties. In doing so, Sutherland's law is employed. As the estimated Reynolds numbers are very low, the cooling air flow is simulated using a laminar flow model. Detailed information on the spacers' material is not available, so they are assumed to be made of polycarbonate[15]. In a real application of this cooling

[14] The flow rate through a single gap is estimated by the total flow rate divided by the number of gaps.
[15] Anyway, material properties of relevant plastics are within a certain value range.

concept, a second pack would be arranged symmetrically to the side plate. For that reason, the side plate is also assumed to be made of polycarbonate. Table 4.11 gives an overview on materials used in this model. As corresponding material parameters have already been presented above, only a reference to the related passage is given. Similar to the above models, the terminal cover fits terminals and busbars closely. Again, any disregarded gaps are considered by a thermal contact resistance $R_{\text{gap}} = 0.0385\,\text{m}^2\,\text{K}\,\text{W}^{-1}$. Information on the location of these gaps is given in figures 4.3 and 4.4.

Name	Material	Table
Busbar	Copper	
Cover plate	Aluminum	
Spacer	Polycarbonate	3.6
Side plate	Polycarbonate	
Terminal cover	Polycarbonate	
Terminal cavity	Air	3.7
Cooling air	Air	4.7

Tab. 4.11: Materials of the air gap model (exclusive cells).

As discussed in the geometry section, the cooling air region consists of two characterizing domains – the air intake and the gaps. The intake volume is laterally surrounded by smooth walls as indicated in figure 4.18. These walls are not included in any heat transfer processes, so they are set adiabatic. The top surface of the intake represents the inlet boundary. The boundary condition for air inflow at the inlet is specified specified by volumetric flow rate and temperature from the project partner. The cooling air region ends with the exit openings of the gaps. Thus, outlet conditions have to be applied at these faces. A summary of cooling air boundary conditions is given in the following list. Therein A_{in} denotes the area of the inlet boundary and $\vec{e}_{\text{x}}$ the face normal of the inlet boundary:

- Velocity inlet: $\vec{v}_{\text{in}} = \dot{V} \,/\, A_{\text{in}} \cdot \vec{e}_{\text{x}}$ using $\dot{V} = 8800\,\text{L}\,\text{h}^{-1}$, $\theta_{in} = 22\,^{\circ}\text{C}$
- Pressure outlet: $p_{\text{out}} = 0\,\text{Pa}$, reference pressure $p_{\text{ref}} = 1013.25\,\text{mPa}$

As mentioned, modeling an enclosing air volume is omitted and a temperature boundary condition is applied directly at the top surface of the terminal cover instead. This surface is tagged by an arrow in figure 4.18. The temperature is chosen to be $\theta_t = 22\,^{\circ}\text{C}$. The model represents only one half of a fully symmetrical problem, in which the resulting temperature field would also be symmetrical. As a consequence, zero heat transfer would develop across the symmetry plane. To account for this fact, the surface of the side plate is set adiabatic. For simplification, all remaining surfaces are set adiabatic as well. Referring to the electric model, an electrical conductivity curve σ_{all} (equation (3.24)) is used, and a current of $i = 54\,\text{A}$ is applied to each cell.

The air gap models are computed as steady state simulations. The under-relaxation factors are increased to improve the rate of convergence. For an automated sequencing of simulation runs, stopping criteria as defined by equations (4.3) and (4.4) are used. The following list gives a summary of air gap widths considered in the study:

- $d = \{2, 2.5, 3, 3.5, 4, 4.5, 5\}\,\mathrm{mm}$

4.3.3 Results

At the inlet boundary very low cooling air velocities of $|\vec{v}_{\mathrm{in}}| \approx 0.045\,\mathrm{m\,s^{-1}}$ on average are obtained. The flow velocity increases considerably while entering gaps because of the large decrease of the cross-sectional area.[16] Table 4.12 lists resulting mean velocities – the ratio of maximum gap velocity to mean velocity is approximately 1.7. However, resulting Reynold's numbers are far below the critical threshold and a laminar flow regime is developed throughout the cooling air volume. The obtained outlet temperatures are decreasing with ascending gap width. That means, the net heat transfer of cooling air is reduced and less heat is transferred from solid structure to cooling air, respectively. Equivalent information is given in the last column of table 4.12. There the net heat transfer of the cooling air is related to total power loss of the pack. Comparing gap widths $d = 2\,\mathrm{mm}$ and $d = 5\,\mathrm{mm}$, the ratio decreases approximately $-1\,\%$. The disadvantageous influence of gap width on heat transfer is probably mitigated by increased cell temperatures. Furthermore, higher temperatures cause a decrease in power loss of approximately $-1.2\,\%$.

Nominal gap parameters			Results of the air gap model		
Gap width d	Mean velocity	Reynolds number[17]	Outlet temperature	Total power loss	Ratio of heat flows[18]
mm	$\mathrm{m\,s^{-1}}$	1	°C	W	1
2	1.3	289	34.2	38.2	0.935
2,5	1.1	277	34.1	38.1	0.933
3	0.9	266	34.1	38.0	0.932
3,5	0.8	257	34.0	38.0	0.930
4	0.7	247	34.0	37.9	0.928
4,5	0.6	239	33.9	37.8	0.926
5	0.5	231	33.9	37.7	0.924

Tab. 4.12: Results of the air gap model.

The obtained temperatures can be seen in figure 4.19, illustrating critical parameters *Maximum temperature* and *Maximum temperature difference*. In contrast to the above

[16] The total cross-sectional area of the gaps is on average 0.9 % of the area of the inlet boundary.
[17] Calculated for $\theta_{\mathrm{in}} = 22\,°\mathrm{C}$.
[18] Ratio of net heat transfer of the cooling air to total power loss of the pack.

models, the parameters are evaluated for each single cell as well. The cells are numbered consecutively from pack front end to pack rear end. To provide an example, *Cell 1* and *Cell 12* denote the outermost cells of the pack. Curve *All* denotes an evaluation based on the entire volume of all jelly rolls. Comparing gap widths $d = 2\,\text{mm}$ and $d = 5\,\text{mm}$, the

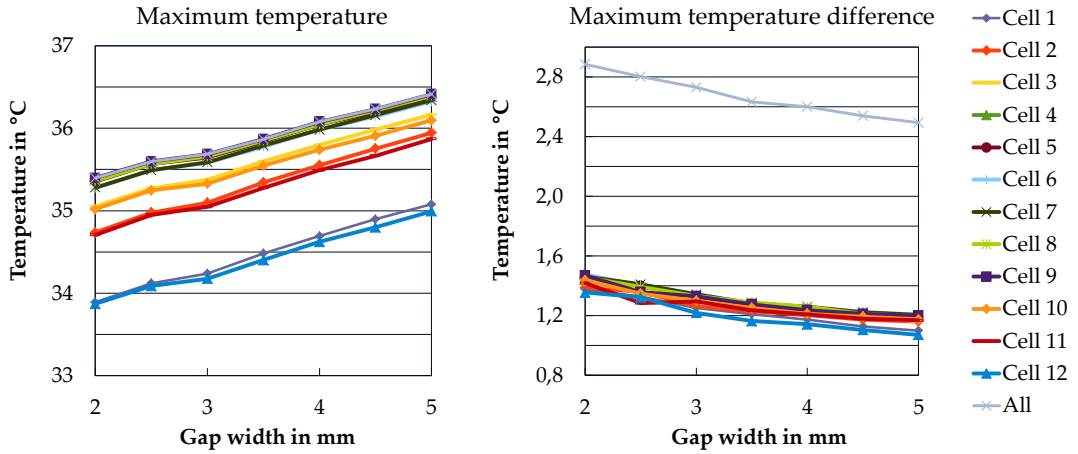

Fig. 4.19: Temperatures within jelly rolls dependent on gap width.

maximum temperature increases on average 1.1 °C or 3.3 %. The plot clearly shows that cell temperatures increase uniformly since the curves are almost parallel. Furthermore, a symmetry is found as curve pairs *Cell 1/12*, *Cell 2/11*, and *Cell 3/10* take an identical course. A maximum temperature difference of 1.3 °C on average is obtained considering each cell separately. Temperature homogeneity achieved with this cooling concept is very satisfactory, even curve *All* results in an average value of just 2.7 °C. Actually, further improvement of temperature homogeneity will be achieved by adapting the design of the outermost spacers. As the outermost air gaps – in contrast to all other gaps – are fed by single cells only, the cooling effect acting upon these cells is increased. Thus, a temperature gradient develops in longitudinal direction of the pack, causing the differences between maximum temperatures. This fact is clearly presented in figure 4.20, which gives temperature at a vertical section through the pack. Further, the figure shows that the hottest zones are located near the outlet boundary and inside cells positioned centrally in the pack. Excessive cooling of the outermost cells can be circumvented by simply reducing the total flow section of the outermost spacers by half. Further sections through the temperature field are shown in figures A.1 and A.2 in the appendix.

It should be noted that the obtained variations of heat flows and temperatures are very low. The thermal effect of a modified gap width will not have any practical relevance in a real application. On the other hand, the gap width considerably affects the pressure drop of the cooling system. As presented in figure 4.21, the pressure drop decreases approximately by 90 % over the entire range of investigated gap width.[19] The pressure

[19] Additionally, figure 4.21 illustrates heat flows which have already been considered in the discussion of table 4.12. The figure shows that net heat transfer of the cooling air is more decreasing than ohmic heat generation. The small value range of the secondary axis should be considered.

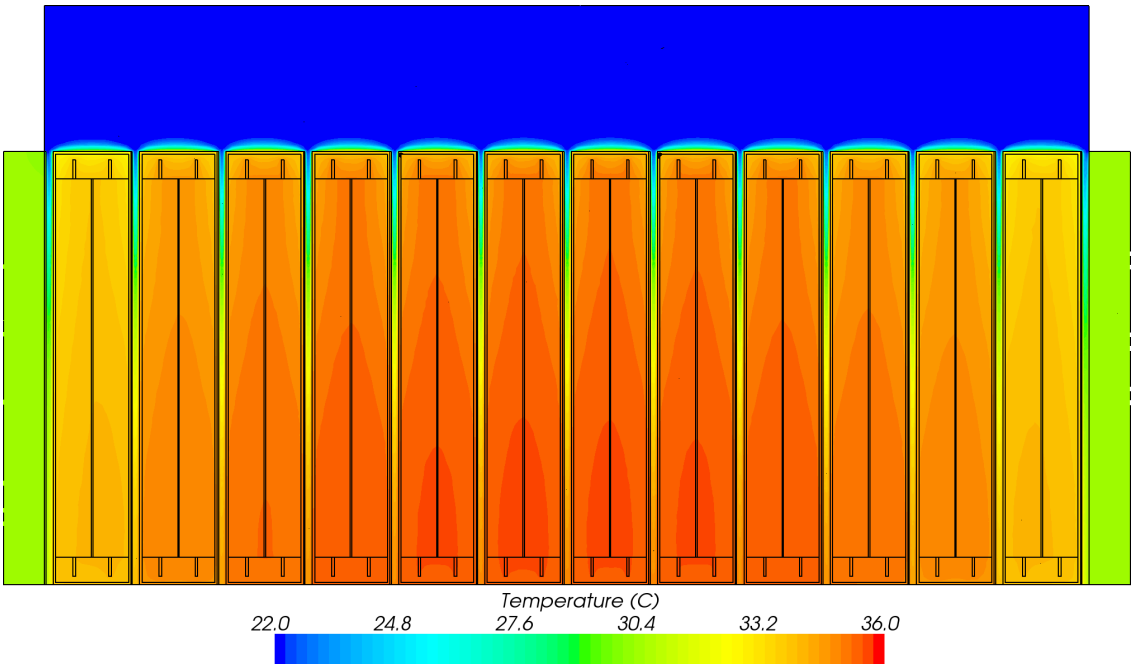

Fig. 4.20: Temperatures, vertical section through jelly roll centers, $d = 2.5\,\text{mm}$.

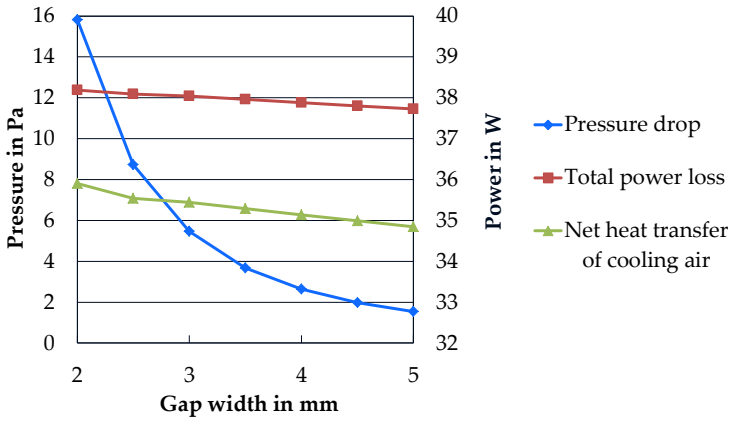

Fig. 4.21: Pressure drop between inlet and outlet and heat flows.

drop is evaluated between inlet and outlet boundary,[20] but most of the pressure drop is generated inside the air gaps. As representative example, a closer look is taken at case $d = 2.5\,\text{mm}$. While the total pressure drop of 8.7 Pa is obtained between inlet and outlet boundary, the pressure drop between the gap entry section and the outlet is 7.7 Pa. As a consequence, the gap width is a fundamental design parameter regarding efficiency of the cooling system. On the other hand, the pressure drop within the gaps should even be significantly higher than that of the air supply. Under this condition cooling air will be distributed uniformly to all gaps.

[20] In doing so, pressure is averaged over the relevant area.

5 Summary and Conclusion

CFD simulations are modern engineering tools used frequently to enhance development processes in a wide range of industries, including the automotive sector. For a successful implementation of electromobility, the problem of battery aging has to be brought under control. Therefore, having knowledge of the spatial temperature distribution across the battery is essential.

The Cell Model

The CFD model developed in the present thesis provides the desired temperature distribution. For computing the thermal state of a lithium-ion cell, the layered structure of the jelly roll and the temperature-dependent production of waste heat caused by an electric load are considered in a coupled approach.

The results of the CFD simulations are verified with experimental data. The experiments are performed using specially defined load profiles, and care is taken to obtain a natural convection situation. Furthermore, the experimental data is used to parameterize the cell's internal resistance. A model including the environment (*air box model*) and a model only representing heat dissipation to the environment by boundary conditions (*plain cell model*) are used to compute steady state simulations. Both models provide very good agreement with measurements from experiments. The results of the air box model show that each heat transfer mechanism – convection, radiation, and conduction – contributes to heat dissipation significantly. In particular, the influence of radiation is significant in the present case of natural convection. The layered structure inside the cell causes the temperature profile to be almost uniform parallel to the layers, while a pronounced temperature gradient is developed perpendicular to the layers. The obtained surface temperature is rather smooth. This fact motivates to average the heat transfer coefficient over the dissipation surface. The heat transfer coefficient is in turn an input variable of the plain cell model. The plain cell model represents a simplified modeling approach and provides low-cost simulations because of a small number of finite volumes. Hence, the plain cell model is employed to virtually rerun the entire experiment in a transient analysis. These results also show very good agreement with the experiment, confirming the validity of the CFD model.

Naturally, the correctness of the spatial temperature distribution cannot be checked directly as temperature measurement inside the cell is absolutely impossible. Heat conduction, however, is a well described phenomena and therefore validity of the obtained temperature field is inferred from correctly obtained surface temperature.
Furthermore, it should be noted that real power loss – derived from measured terminal

voltage and terminal current – is generated in all conducting components of the cell, but the electric model is restricted to the jelly roll volume only. This fact represents a compromise, which has to be made to meet modeling requirements. The experiment results indicate a significant generation of ohmic heat inside the power cables, so heat generation is expected to be noticeable within cell components besides the jelly roll as well. In other words, the CFD model describes power loss truly in the sense of totally generated heat, but the spatial distribution of heat source density is slightly different compared to the real condition. Consequently, the model's temperature distribution should be slightly distorted, especially in the area of aforementioned components. On the other hand, the experiment results point out that only highest loads cause a significant heat generation inside the cables. Thus, the effect should be negligible concerning moderate or small electric loads.
Considering very small electric loads, the parameterization of the internal resistance may be used inappropriately. Since the internal resistance also depends on electric load, a load different to those loads as covered by the parametrization would probably induce inaccurate results. Anyhow, the heat introduced into the cell – and therefore the changes in surface temperature – will be relatively low. This fact has to be considered if further experiments should be carried out.

Finally, a brief outlook on development potentialities of the CFD model is given. One option would be to create an even more abstract model of the jelly roll by omitting the segmentation of the jelly roll substitute at all. The jelly roll substitute would consist of one contiguous volume and two opposite surfaces, for example those ones bordering the current collectors, can be used to apply electric boundary conditions. As a consequence, computed electric current density will miss orientation and magnitude of the real current density vectors. Presumably, this fact does not matter as only the (scalar) source density of ohmic heat is of interest. Having said this, an investigation is recommended if that new current density field influences the spatial distribution of ohmic heat generation negatively, especially in cases of high temperature gradients. This approach would be advantageous as current collectors and terminals can be included in the electric model. Moreover, the general modeling effort will be reduced.
Another option would be to create a more detailed model of the jelly roll by geometrically resolving the layers. At least three distinct layers – two metal-based conductors and one intermediate substitute layer – have to be modeled to obtain a properly functioning, electric model. The substitute layer represents the active zone of the cell (anode, cathode, and separator), and its thermal and electrical properties can be determined using the methods presented in the thesis. This approach would also enable all conducting parts to be included in the electric model. As a consequence, more accurate results regarding the electric current density field and the temperature field are obtained. The improved geometric resolution could also form a basis for more sophisticated simulations. For example, progressive temperature rise and final malfunction caused by thermal runaway could be investigated. The suggested enhancements are accompanied by an immense increase of computational cost.

The Pack Models

The derived cell model is used to investigate cooling concepts of a battery for vehicular applications. In doing so, only a part of the battery – a pack comprising twelve cells – is implemented and three different cooling concepts are investigated by parameter studies. In the first concept, the cells are consecutively arranged in a row and the cooling effect is realized by conducting coolant through a cooling plate affixed to the bottom surfaces of the cells. In the second concept, the cooling plate is replaced by a cooling duct and air is used as cooling fluid. The third concept is realized in conducting air through gaps which are formed by spacers inserted between the cells.

Regarding the spatial temperature distribution, the concepts of cooling plate and cooling duct show an almost identical behavior. Generally, a pronounced temperature gradient develops in longitudinal direction of the pack, while the temperature profile is rather smooth in transversal sections. The simulation results show that inserting a thermal pad between the cooling plate and the cells homogenizes the temperature field, but raises the general temperature level. Besides, it is crucial to see this advantageous effect on temperature spread in conjunction with the temperature boundary condition of the model. Furthermore the results show that – under the condition of equal maximum temperature and pad resistance – the cooling duct concept provides less temperature spread than the cooling plate concept. On the other hand, the flow rates of cooling air have to be much higher than those of the coolant to achieve an appropriate cooling effect. Thus, considerable flow velocities are obtained inside the duct. The third concept represents the most preferable alternative from a thermal point of view as it provides the least temperature spread. Moreover, the results show that the gap width impacts heat transfer capability of the system marginally, but affects pressure drop significantly.

Although the maximum temperature and the homogeneity of the temperature field represent key parameters regarding the battery performance and the aging behavior, some other issues might affect the application of a certain cooling concept. Especially for an electric vehicle, a further key parameter is the efficiency of the entire cooling system. For that reason a liquid cooling fluid, characterized by a high mass density and a high heat capacity, is advantageous. Then the prerequisite of high flow rates and thus high pumping power is circumvented. Besides this, a solution with minimum space requirements is implemented. The disadvantageous temperature spread of the cooling plate concept can be improved by simply reducing pack length. On the other hand, extra effort has to be expended to ensure the liquid tightness of the system. Tightness is a stringent necessity as lithium reacts vigorously with aqueous solutions. This potential danger is avoided by using air as cooling fluid. Further, using air reduces the structural complexity of the entire car as the cooling circuit can be included into the air conditioning system. On the other hand, applicability of an air-based system may be restricted by allowable maximum velocity as the introduction of acoustic noise must be prevented. All together, thermal adjustment of the battery is a nontrivial task which should be accomplished in view of the complete car concept. Based on the promising results of the simulations, the air gap concept is recommended for realization.

Appendix

A Additional Results of the Cooling Plate Model

Table A.1 provides the net heat transfer of the coolant in relation to total power loss of the model. This method of illustration provides the same information content such as figure 4.11. Values greater than one mean that heat flows from the environment into the pack. A consideration combined with table 4.5 allows the expression of absolute values. Table A.2 presents the total heat flow across interfaces between cells and cooling plate, in other words the total heat flow through the thermal pad. The values are expressed in relation to net heat transfer of the coolant. A value greater than one indicates that part of heat flowing through the pad is conducted through the cooling plate and dissipated to the environment.

R_{pad}	$\dot{V}$					
	1e-7	3e-7	5e-7	1e-6	3e-6	5e-6
0	0.585	0.870	0.936	1.004	1.084	1.105
1.25e-3		0.849	0.920	0.987	1.058	
2.50e-3		0.841	0.912	0.978	1.048	
3.75e-3		0.834	0.904	0.969	1.039	

Tab. A.1: Ratio of net heat transfer of the coolant to total power loss of the pack.[1]

R_{pad}	$\dot{V}$					
	1e-7	3e-7	5e-7	1e-6	3e-6	5e-6
0	1.125	1.023	1.008	0.996	0.984	0.978
1.25e-3		1.019	1.004	0.992	0.979	
2.50e-3		1.016	1.000	0.989	0.975	
3.75e-3		1.012	0.997	0.985	0.971	

Tab. A.2: Ratio of total heat flow through the thermal pad to net heat transfer of the coolant.[1]

[1] $[R_{\text{pad}}] = \text{m}^2\,\text{K}\,\text{W}^{-1}$, $[\dot{V}] = \text{m}^3\,\text{s}^{-1}$.

B Additional Results of the Cooling Duct Model

Table A.3 lists the total ohmic heat generated within the cooling duct model. The average power loss per cell is calculated to $P_{\text{cell}} \approx 2.3\,\text{W}$. Table A.4 provides the net heat transfer of the cooling air, expressed in ratios of net heat transfer to total power loss. A value greater than one means that heat flows from the environment into the pack. It should be noted that these values are lower than those of the cooling plate concept. This fact confirms that the cooling duct concept has a higher heat transfer capability than the cooling plate concept. For the comparison of cooling plate and cooling duct results, an equivalent basis should be used. To provide an equal pad resistance, values in table A.1 should be interpolated between second and third row. To obtain similar maximum temperatures, only values associated with $\dot{V}_{\text{in}} = 1.25\text{e-}3 \ldots 8.5\text{e-}3$ of the first column of table A.4 should be used. Then conditions corresponding to a maximum temperature range of $\approx$28 °C to $\approx$44 °C and a pad resistance of $R_{\text{pad}} = 1.875\text{e-}3\,\text{m}^2\,\text{K}\,\text{W}^{-1}$ will be compared.

$\dot{V}_{\text{in}}$ in $\text{m}^3\,\text{s}^{-1}$	$\theta_{\text{in}} = 10\,°\text{C}$	$\theta_{\text{in}} = 20\,°\text{C}$	$\theta_{\text{in}} = 30\,°\text{C}$
5.00e-4	25.9	25.3	
1.25e-3	27.4	26.4	25.5
2.00e-3	28.3	27.1	26.0
2.50e-3			26.2
2.75e-3	29.2	27.6	
4.50e-3	30.4	28.4	26.9
6.50e-3	31.2	29.1	27.3
8.50e-3	31.9	29.5	27.5
1.00e-2	32.3	29.8	27.7

Tab. A.3: Total power loss of the pack in W.

$\dot{V}_{\text{in}}$ in $\text{m}^3\,\text{s}^{-1}$	$\theta_{\text{in}} = 10\,°\text{C}$	$\theta_{\text{in}} = 20\,°\text{C}$	$\theta_{\text{in}} = 30\,°\text{C}$
5.00e-4	0.60	0.50	
1.25e-3	0.78	0.66	0.54
2.00e-3	0.87	0.74	0.61
2.50e-3			0.64
2.75e-3	0.92	0.80	
4.50e-3	0.99	0.87	0.72
6.50e-3	1.05	0.91	0.76
8.50e-3	1.08	0.94	0.79
1.00e-2	1.10	0.96	0.82

Tab. A.4: Ratio of net heat transfer of the cooling air to power loss.

C Additional Results of the Air Gap Model

Figure A.1 provides temperature in perpendicularly cross sections. On the left, a section through the central spacer – and thus route of cooling air – is shown. The picture illustrates that air temperature remains constant inside the air intake, and how cooling air heats up while passing through the gaps. On the right, a section trough the cell next to the central spacer is shown. Temperature rises slightly towards the outlet boundary, but the temperature profile is almost uniform. Air inside the terminal cover is nearly quiescent, therefrom heat transfer is dominated by conduction and a sharp temperature gradient is obtained. For the sake of completeness, a horizontal section trough the jelly roll centers is given in figure A.2.

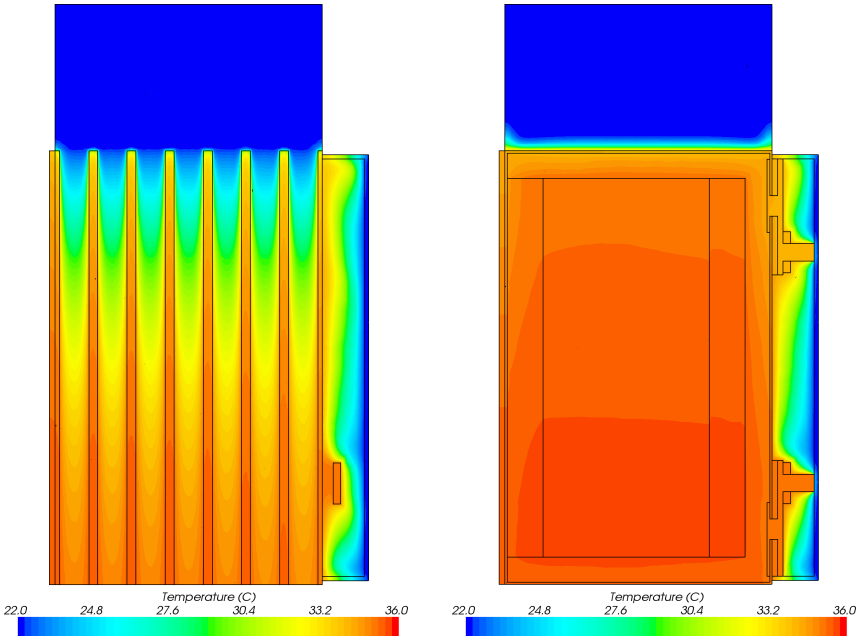

Fig. A.1: Temperatures, transverse section through central spacer (left side) and a cell next to this spacer (right side), $d = 2.5\,\mathrm{mm}$.

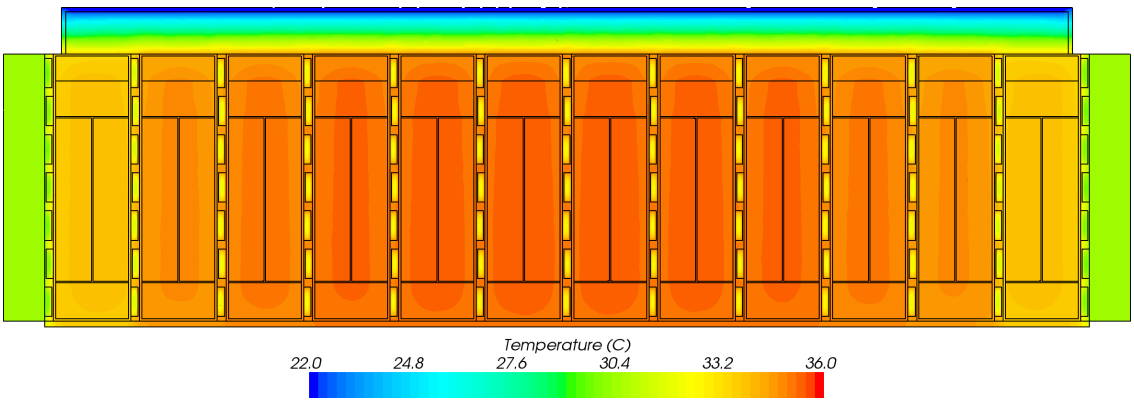

Fig. A.2: Temperatures, horizontal section through jelly roll centers, $d = 2.5\,\mathrm{mm}$.

List of Figures

List of Tables

Bibliography

[1] American Society of Heating, Refrigerating and Air-Conditioning Engineers, Inc. ASHRAE Handbook Fundamentals, 2009.

[2] Auer Kunststofftechnik GmbH & Co KG, December 2010. http://www.auer-kunststofftechnik.de/daten.htm.

[3] H. D. Baehr and K. Stephan. *Wärme- und Stoffübertragung*. Springer, Berlin, 7. edition, 2010.

[4] E. Becker. EEI_101110_Geometrie_Zelle_AIT_Ebe.ppt. Presentation of cell disassembling.

[5] J. K. Carson, S. J. Lovatt, D. J. Tanner, and A. C. Cleland. Thermal conductivity bounds for isotropic, porous materials. *International Journal of Heat and Mass Transfer*, 48:2150–2158, 2005.

[6] CD-adapco. *Star-CCM+ Material Database*, 6.02.007 edition.

[7] CD-adapco. *Star-CCM+ User Guide*, 6.02.007 edition.

[8] Dr. D. Müller GmbH. Wärmeleitfolien ab 0.5 mm, March 2011. http://www.mueller-ahlhorn.com/produkte-materialien/material/waermeleitprodukte/waermeleitprodukte/waermeleitfolien-ab-05-mm/.

[9] K. Grote and J. Feldhusen, editors. *DUBBEL – Taschenbuch für den Maschinenbau*. Springer, Berlin, 22. edition, 2007.

[10] G. Guo, B. Long, B. Cheng, S. Zhou, P. Xu, and B. Cao. Three-dimensional thermal finite element modeling of lithium-ion battery in thermal abuse application. *Journal of Power Sources*, 195:2393–2398, 2010.

[11] Japanese manufacturer. Specifications 22.5 Ah cell.

[12] A. Jossen and W. Weydanz. *Moderne Akkumulatoren richtig einsetzen*. Ubooks, 1. edition, 2006.

[13] U. S. Kim, C. B. Shin, and C.-S. Kim. Effect of electrode configuration on the thermal behavior of a lithium-polymer battery. *Journal of Power Sources*, 180(2):909–916, 2008.

[14] B. J. Landi. Nanomaterial approaches to enhance lithium ion batteries, June 2011. http://www.oecd.org/dataoecd/22/63/44028153.pdf.

[15] D. Linden and T. B. Reddy, editors. *Handbook of batteries*. McGraw-Hill Handbooks, New York, 3. edition, 2002.

[16] Pike Research, Cleantech Market Intelligence. Asian manufacturers will lead the $8 billion market for electric vehicle batteries, June 2011. http://www.pikeresearch.com/newsroom/asian-manufacturers-will-lead-the-8-billion-market-for-electric-vehicle-batteries.

[17] H. Schlichting and K. Gersten. *Grenzschicht-Theorie*. Springer, Berlin, 10. edition, 2006.

[18] V. Srinivasan. Batteries for vehicular applications. In *PHYSICS OF SUSTAINABLE ENERGY: Using Energy Efficiently and Producing It Renewably*, volume 1044 of *Conference Proceedings*, pages 283–296. AIP, 2008.

[19] Synflex Elektro GmbH. Nomex 410 Aramidpapier, March 2011. http://www.synflex.de/de/produkte_pdf/?id=25&areaid=flaechenisolierstoffe.

[20] viZaar AG (Bereich Thermografie). Emissionsgradtabelle, February 2011. http://www.thermografie-xtra.de/de/waermebildkamera-tipps-tricks-know-how/emissionsgrad-tabelle.html.

[21] M. Winter and R. J. Brodd. What Are Batteries, Fuel Cells, and Supercapacitors? *Chemical Reviews*, 104(10):4245–4270, 2004.